

CORRECTION OF THE POST – NECKING TRUE STRESS – STRAIN
DATA USING INSTRUMENTED NANOINDENTATION

by

Iván Darío Romero Fonseca

A dissertation submitted to the faculty of
The University of North Carolina at Charlotte
in partial fulfillment of the requirements
for the degree of Doctor of Philosophy in
Mechanical Engineering

Charlotte

2014

Approved by:

Dr. Qiuming Wei

Dr. Harish Cherukuri

Dr. Alireza Tabarraei

Dr. Carlos Orozco

Dr. Jing Zhou

©2014
Iván Darío Romero Fonseca
ALL RIGHTS RESERVED

ABSTRACT

IVÁN DARÍO ROMERO FONSECA. Correction of the post-necking True Stress-Strain data using instrumented nanoindentation.
(Under the direction of DR. QIUMING WEI)

The study of large plastic deformations has been the focus of numerous studies particularly in the metal forming processes and fracture mechanics fields. A good understanding of the plastic flow properties of metallic alloys and the true stresses and true strains induced during plastic deformation is crucial to optimize the aforementioned processes, and to predict ductile failure in fracture mechanics analyzes. Knowledge of stresses and strains is extracted from the true stress-strain curve of the material from the uniaxial tensile test. In addition, stress triaxiality is manifested by the neck developed during the last stage of a tensile test performed on a ductile material. This necking phenomenon is the factor responsible for deviating from uniaxial state into a triaxial one, then, providing an inaccurate description of the material's behavior after the onset of necking

The research of this dissertation is aimed at the development of a correction method for the nonuniform plastic deformation (post-necking) portion of the true stress-strain curve. The correction proposed is based on the well-known relationship between hardness and flow (yield) stress, except that instrumented nanoindentation hardness is utilized rather than conventional macro or micro hardness. Three metals with different combinations of strain hardening behavior and crystal structure were subjected to quasi-static tensile tests: power-law strain hardening low carbon G10180 steel (BCC) and electrolytic tough pitch copper C11000 (FCC), and linear strain hardening austenitic

stainless steel S30400 (FCC). Nanoindentation hardness values, measured on the broken tensile specimen, were converted into flow stress values by means of the constraint factor C from Tabor's, the representative plastic strain ϵ_r and the post-test true plastic strains measured. Micro Vickers hardness testing was carried out on the sample as well. The constraint factors were 5.5, 4.5 and 4.5 and the representative plastic strains were 0.028, 0.062 and 0.061 for G101800, C11000 and S30400 respectively. The established corrected curves relating post-necking flow stress to true plastic strain turned out to be well represented by a power-law function.

Experimental results dictated that a unique single value for C and for ϵ_r is not appropriate to describe materials with different plastic behaviors. Therefore, Tabor's equation, along with the representative plastic strain concept, has been misused in the past. The studied materials exhibited different nanohardness and plastic strain distributions due to their inherently distinct elasto-plastic response. The proposed post-necking correction separates out the effect of triaxiality on the uniaxial true stress-strain curve provided that the nanohardness-flow stress relationship is based on uniaxial values of stress. Some type of size effect, due to the microvoids at the tip of the neck, influenced nanohardness measurements. The instrumented nanoindentation technique proved to be a very suitable method to probe elasto-plastic properties of materials such as nanohardness, elastic modulus, and quasi-static strain rate sensitivity among others. Care should be taken when converting nanohardness to Vickers and vice versa due to their different area definition used. Nanohardness to Vickers ratio oscillated between 1.01 and 1.17

DEDICATION

This dissertation is dedicated to: my parents, Jorge Enrique and Elvira, who have given me always unconditional and invaluable support; to my grandmother Sara who departed this world during my studies; to my brothers, Javier Enrique and Jorge Andrés (R.I.P), and my beloved sister Maria Jimena; finally, to my 3-year-old little girl Gabriela who has been “an engine” that drives me in pursuing this goal until the end and never give up.

ACKNOWLEDGMENTS

I would like to thank my advisor Dr. Qiuming Wei for the opportunity he gave me to be part of his research group and for his guidance and support during my research. I want to thank Dr. Harish Cherukuri who was always willing to help me from the very beginning of my graduate studies. Also, thanks to Dr. Alireza Tabarraei, Dr. Carlos Orozco and Dr. Jing Zhou who very kindly accepted to be part of this committee.

I would like to express my gratitude to Dr. M. Garry Hodgins for his guidance, great support, and his boundless human quality. Thanks to Dr. Robin Coger who gave a lot of advice and encouragement to me, both, in the academic and personal life. Special thanks to Mr. Franklin Green, Dr. Thomas Koch and Dr. HaiTao Zhang for their abundant collaboration and cooperation with the use of the labs and equipment necessary for this research. I received generous support from Matthew Bellasai, Hernando Pacheco Gómez, Michael Tompkins and Marc Marcos in the machine shop. I am particularly grateful for the assistance, feedback and suggestions given by Maria Nikopoulos regarding academic writing. Thanks to the other members of Dr. Wei's research group, past and present ones, for their fellowship and their accompaniment during these years.

Special thanks to the Graduate school of the University of North Carolina at Charlotte for supporting me through the GASP and the Teaching Assistantship programs; also, to the Center for Graduate Life.

Above all my deepest thankfulness to the Creator whose will only made possible this accomplishment.

TABLE OF CONTENTS

LIST OF TABLES	x
LIST OF FIGURES	xi
CHAPTER 1: INTRODUCTION	1
1.1 Metals Under Uniaxial Quasi-static Tensile Loading.	1
1.2 Tensile Test Theory – Stress – Strain Curves.	3
1.2.1 Engineering Stress – Strain curves.	6
1.2.2 True Stress – Strain Curves.	12
1.3 Necking Behavior.	17
1.4 The Bridgman Correction of the Post Necking Stress – Strain Data.	21
1.5 Hardness of Metals.	24
1.5.1 Indentation Hardness Tests.	25
1.6 Relationship between Hardness and the Flow Curve of a Metal.	26
1.7 Instrumented Nanoindentation Testing – Indentation Hardness.	32
1.7.1 Pile – up and sink – in Behavior.	37
1.7.2 Indentation Size Effect (ISE).	40
1.8 Motivation of this Research.	41
1.9 Research Objectives.	42
1.10 Organization of this Dissertation.	43
CHAPTER 2: PROPOSED METHODOLOGY	45
2.1 Forward and Reverse Analysis	45
2.2 Applicability of Tabor’s Relationship	46
2.3 Representative Plastic Strain	48

2.4 Approaches of this Work	51
CHAPTER 3: MATERIALS AND EXPERIMENTAL PROCEDURES	55
3.1 Materials.	55
3.2 Mechanical Testing.	56
3.2.1 Tensile Test.	56
3.2.2 Instrumented Nanoindentation and Microhardness.	57
3.2.3 Compression Test.	59
3.2.4 Nanoindentation Strain Rate Sensitivity.	60
3.3 Preparation of the Surface of Samples.	60
3.4 Optical and Scanning Electron Microscopy.	61
CHAPTER 4: RESULTS AND DISCUSSION	63
4.1 Stress-Strain Curves.	63
4.2 Indentation Hardness Profile.	68
4.3 Indentation Hardness Map.	69
4.4 Mapping Indentation Hardness Into Flow Stress.	71
4.5 Reverse Analysis.	75
4.6 Corrected True Stress-Strain Data.	79
4.7 Validity of the Method.	81
4.8 Comparison Between Experimental Results to Other Models.	82
4.9 Strain Rate Sensitivity at the Neck Region.	85
4.10 Limiting Factors in the Research of this Dissertation.	87
4.11 Optical Microscope and SEM Images for G10180.	88
CHAPTER 5: EVALUATION OF MECHANICAL PROPERTIES OF ECAE COPPER VIA INSTRUMENTED INDENTATION	91

	ix
5.1 Introduction	91
5.2 Experimental Procedure	95
5.3 Results and Discussion	98
5.4 Summary and Concluding Remarks.	106
CHAPTER 6: CONCLUSIONS AND FUTURE WORK	108
REFERENCES	112
VITA	122

LIST OF TABLES

TABLE 1.1:	Important parameters determined from the True Stress-strain curve.	17
TABLE 1.2:	Static Indentation Hardness testing methods and the formulas involved.	26
TABLE 2.1:	Possible scenarios where Tabor's relationship may be applied. The relationship between hardness and flow stress still holds.	47
TABLE 2.2:	Summary of representative plastic strain values obtained by different groups.	50
TABLE 3.1:	Materials utilized in the research, designation, crystal structure and conditions followed to fully anneal them.	55
TABLE 3.2:	Reagents, their components and procedure followed during the etching process of the samples. Etchant number* according to ASTM Standard.	61
TABLE 4.1:	Elasto-plastic properties from engineering stress-strain curves of G10180, C11000 and S30400.	64
TABLE 4.2:	Strain hardening and nanohardness expressions as functions of the true plastic strain interval specified.	73
TABLE 4.3:	Constraint Factor C, obtained from nanoindentation hardness.	77
TABLE 4.4:	Representative stress and Representative plastic strain values for G10180, C11000 and S30400.	79
TABLE 5.1:	Product yield in percentage for ECAE processing routes as a function of number of passes.	95

LIST OF FIGURES

- FIGURE 1.1: A prismatic circular bar under (a) tensile and (b) compressive loading. The dashed blue lines represent the original geometry. The solid lines represent the deformed geometry. F : applied load; A_0 : initial cross section area; l : deformed length or final length; l_0 : original length of the specimen. 2
- FIGURE 1.2: Schematic of the major frame of a tensile test device. The specimen is placed in the grips and pulled until fracture. The extensometer measures the change in length within the gage section from which the specimen strain is derived. 4
- FIGURE 1.3: (a) Tensile-test specimen before and after testing; l_f is the gage length after fracture. (b) Schematic sequence depicting the deformation phases in the specimen and their corresponding points in the stress-strain curve. 6
- FIGURE 1.4: Determination of the yield strength in (a) ductile metals using 0.002 permanent offset strain and (b) typical curve for steel showing the yield point phenomenon. In this case usually the lower yield point is taken as the yield strength of the steel. 8
- FIGURE 1.5: Schematic engineering stress-strain curves for different materials. (a) Ductile behavior with necking after the tensile strength (UTS) is reached. (b) Relatively brittle behavior and (c) completely brittle behavior. In (b) and (c) necking is not present, and the tensile strength is the fracture strength. In all cases the UTS is the maximum stress value. 9
- FIGURE 1.6: Schematic illustration of how the yield strength is affected by the amount of plastic deformation as if the metal would have been unloaded and reloaded again. Dashed lines parallel to the elastic portion are to obtain the yield strength, points C and D, for initial and re-loaded case respectively. 14
- FIGURE 1.7: (a) Comparison of engineering and true stress strain curves. (b) Tension True curve (flow) compared to that from compression test. 16
- FIGURE 1.8: Considère criterion to illustrate the onset of necking. True and nominal stress-strain curves are plotted along with the strain hardening rate (dashed line in the upper right corner). 19
- FIGURE 1.9: Triaxial stress state in a tensile specimen at the neck region showing longitudinal, circumferential and radial stresses. 20

FIGURE 1.10: The Bridgman correction factor, B , as a function of the geometry of the neck (primarily the a/R ratio).	22
FIGURE 1.11: Bridgman correction factor as a function of necking strain ϵ_n .	23
FIGURE 1.12: Mean contact pressure vs. indentation strain of annealed copper for various indenter diameters.	30
FIGURE 1.13: Comparison of flow curves obtained from hardness measurements (points) with flow curve obtained from compression test (solid curves) for a mild steel and an annealed copper.	31
FIGURE 1.14: (a) A typical load-displacement curve (schematic) from a Berkovich indentation experiment. (b) Cross-section profile of the specimen surface during the indentation process. h_f : depth of the residual impression. h_e : elastic displacement recovery during unloading. h_c : depth of the contact of the indenter with the specimen at P_{max} . h_s : sink-in of the surface at P_{max} . h_{max} : Maximum indentation depth at P_{max} . a : radius of the contact circle. P : Normal load on sample. S : Contact stiffness (slope of the unloading part). ϕ : half included angle of the indenter.	34
FIGURE 1.15: Berkovich indenter geometry. The shaded area shows the projected contact area that depends on the contact depth at a given time during the indentation.	36
FIGURE 1.16: Sink-in and pile-up during indentation. The actual contact area differs from that one predicted by the calculation of the contact depth.	38
FIGURE 1.17: Indentation profile for a non-strain hardening material. In this figure, z represents the indenter axis direction and r represents the radial direction for cone indentation.	39
FIGURE 2.1: Volume-averaged plastic strain induced by conical indenter of half-angle of 70.3° showing dependency on the strain hardening exponent n , but not on yield strength or elastic modulus.	49
FIGURE 2.2: Strain gradient field under the indenter tip. Simulations of the indentation process on same material. (a) Berkovich. (b) Vickers.	51
FIGURE 2.3: Schematic of the approach. For each of the cross sections, the amount of plastic deformation can be mapped into values of plastic strain in the true stress-strain diagram, which in turn will have a unique value of the flow stress.	52

- FIGURE 2.4: Tabor's relationship illustrated for the three different cases mentioned above: (a) perfectly plastic metal, with $C \approx 3$. (b) Indented annealed metal where the representative stress is a function of the representative strain. (c) Metal with initial plastic deformation before indentation; the representative stress is now a function of the initial plastic deformation ϵ_0 , plus the indentation representative plastic strain ϵ_r . 54
- FIGURE 3.1: Cylindrical geometry Tensile Test Specimen: $D=8.9$ mm, $G=36$ mm, $A=41.7$ mm (min), $R=6.35$ mm. 56
- FIGURE 3.2: Schematic illustration showing how the sample for Instrumented Nanoindentation was obtained. (a) Post-tensile test specimen half. (b) Cutting along axial plane to extract a 5 mm slice. (c). Sample for Instrumented Nanoindentation, where L_s is the length of the sample along nanohardness measurements were taken. 58
- FIGURE 3.3: Map of the nanoindentation sites for the G10180. Transverse or diametral direction, and axial distance from gage length mark, L_s . 59
- FIGURE 4.1: Nominal stress-strain curves from uniaxial tensile tests carried out on (a) G10180, (b) C11000 and (c) S30400. Results from two specimens are displayed. 63
- FIGURE 4.2: Before (bottom) and after (top) G10180 tensile specimens showing the necking feature and the decrease in diameter along the whole reduced section. 65
- FIGURE 4.3: True stress-strain curves from tensile and compression tests, and fracture points for (a) G10180 steel, (b) C11000 and (c) S30400. The plot on the right of each curve shows the strain hardening behavior of each. 66
- FIGURE 4.4: Variation of hardness with distance from gage length mark, L_s . Berkovich (blue) and Vickers (red) measurements. 68
- FIGURE 4.5: Hardness maps of: (a) G10180 steel. (b) C11000 copper. (c) S30400 stainless steel. 70
- FIGURE 4.6: Log-Log plot of nano Hardness vs. True plastic strain. The power law equation links nanohardness with true plastic strain. (a) G10180 steel, (b) C11000 copper and (c) S30400 stainless steel. The red line is the linear fit at the given scale. 72
- FIGURE 4.7: Plastic strain contours obtained from nanohardness measurements for (a) G10180 steel, (b) C11000 copper and (c) S30400 stainless steel. 74

- FIGURE 4.8: Schematic of the reverse analysis performed. Plastic strain ranges for measured nanohardness (left) and flow curve (right). 75
- FIGURE 4.9: Representative stress for G10180 steel, $\sigma_r = 265.38$ MPa, used as input to find out the representative plastic strain. The total strain for this stress level is $\epsilon_{\text{Total}} = 0.031$. Similar method to find those for C11000 and S30400. 78
- FIGURE 4.10: Corrected True Stress-Strain curves for (a) G10180 steel, (b) C11000 Copper and (c) S30400 Stainless steel. 80
- FIGURE 4.11: Pre-necking nanohardness vs. true plastic strain for S304000 showing linear trend likewise flow stress for the same plastic strains range. 82
- FIGURE 4.12: Comparison of the corrected curve to all true stress-strain data (a) G10180 Steel, (b) C11000 copper and (c) S30400 stainless steel. 84
- FIGURE 4.13: Strain Rate Sensitivity (SRS) of G10180, C11000 and S30400 at the neck. (a), (c) and (d). Nanohardness vs. strain rate, and (b), (d) and (f) strain rate sensitivity exponent m vs plastic strain for the three materials respectively. 86
- FIGURE 4.14: Grain size of G10180. Top left: micrograph taken at X100 showing grain features at the grip section. Top right: micrograph taken at X100 showing elongated grains at the neck region. Bottom: Gradient of grain size and orientation along L_s . 89
- FIGURE 4.15: SEM images of G10180 steel. Top left: microvoids at the center of the failure. Top right: microvoids in the range of 0.5-1 μm . Bottom left: array of four Berkovich indentations at the neck region. Bottom right: Berkovich indentation of comparable size to microvoids at the neck. 90
- FIGURE 5.1: (a) Schematic of an ECAE die showing its geometry. (b) Schematic illustrating the ECAE process and coordinates. 93
- FIGURE 5.2: Hybrid route E following $180^\circ - 90^\circ - 180^\circ$ rotation pattern. 96
- FIGURE 5.3: Load - displacement curves for ECAE copper for (a) $N=0$, (b) $N=4$, (c) $N=24$ and (d) $N=32$ passes showing the influence of the indentation strain rate on the maximum load. 100
- FIGURE 5.4: Variation of Nanohardness with number of passes for ECAE copper. Tests performed at various constant indentation strain rates. 101

The nanohardness peak is reached at N=4 passes.

FIGURE 5.5: Nanohardness as function of indentation strain rate for ECAE copper from N=0 (annealed state) to N=32 passes under route E. Log H vs. Log ϵ . 104

FIGURE 5.6: Strain Rate sensitivity exponent obtained by nanoindentation on ECAE copper (Route E) as function of number of passes. For N=8, data for two different rods is provided. 105

CHAPTER 1: INTRODUCTION

1.1 Metals Under Uniaxial Quasi-Static Tensile Loading.

Quasi-static tensile loading is one of the types of quasi-static loading (the mechanical load changes slowly with time) from which the mechanical strength of the material can be determined at relatively low strain rates. Other types of quasi-static loading include uniaxial (loading in a single direction) compression, bending, shearing, torsional and biaxial loading conditions. When a metal specimen is under tensile loading, it is elongated in the loading (or longitudinal) direction of the specimen under the action of the tensile force. As a result of externally imposed mechanical force, the metal specimen extends or elongates in a temporary (reversible) or permanent (irreversible) manner depending on the capacity of the metal to bear the magnitude of force imposed. At the same time its cross section will usually decrease while the length increases. If the loading forces are of compressive type, the specimen will shrink in length and its cross section will increase. After unloading the specimen to zero force, if the specimen goes back to its original dimensions completely, then the deformation of the specimen is said to be elastic. On the other hand, if the specimen has experienced permanent change in the geometry or dimensions, it is said that plastic deformation or permanent deformation has occurred in the specimen. FIGURE 1.1 depicts the case of a circular cross section specimen under tensile and compressive uniaxial loading. The dashed blue lines represent

the original geometry of the specimen and the solid red lines stand for the geometry after deformation.

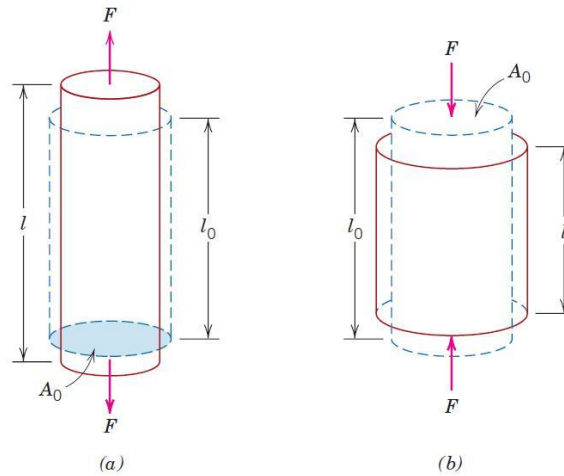


FIGURE 1.1: A prismatic circular bar under (a) tensile and (b) compressive loading. The dashed blue lines represent the original geometry. The solid lines represent the deformed geometry. F : applied load; A_0 : initial cross section area; l : deformed length or final length; l_0 : original length [1] of the specimen.

What must be kept in mind is that elastic deformations may be negligible compared to plastic deformations when the latter ones are well beyond the onset of plasticity. Metals can exhibit either ductile or brittle behavior when subjected to the types of loads mentioned above; on one hand, brittle metals are characterized by failing in a brittle manner without appreciable plastic deformation prior to failure and the deformation experienced by the specimen is nearly exclusively elastic deformation. Such brittle behavior can be found in some refractory metals with body-centered cubic lattice (bcc) structures including polycrystalline tungsten, molybdenum and chromium [2-6], or some steels at low temperatures [7]. On the other hand, ductile metals can exhibit significant amount of permanent or plastic deformation before failing by fracture. Most

face-centered cubic (FCC) metals are ductile, and most BCC metals are also ductile at relatively high homologous temperatures (homologous temperature is the temperature of interest divided by the melting point of the material).

1.2 Tensile Test Theory – Stress – Strain Curves.

Among all the various quasi-static mechanical tests, tensile test is the most common and widely used for the importance and number of properties that can be derived from it. Such mechanical properties are key factors in component design and also are valuable inputs in research and development when comparing new materials or certain types of processes and in the quality control area to assure that the material meets the final needs. The tensile test must be performed in a consistent way, or in such a manner that whoever does it, the outcomes shall be in agreement with any other test of the same material performed on any other machine and in any other laboratory. It is the role of organizations for the standardization of these procedures to develop standard testing methods that anyone in the world can follow. Such standards usually involve guidelines for the geometries of the specimen, loading speed, testing temperature, machine calibration, and any other factors and parameters that affect the outcome properties of the test. In the United States the aforementioned organization is the ASTM (American Society for Testing and Materials) and the ISO (International Organization for Standardization) on a worldwide basis.

In a typical tensile test, the specimen is held with two opposite grips, one of them fixed and one movable. One end of the specimen is slowly pulled at a constant rate by an increasing axial (uniaxial) force, and simultaneously, the elongation of the segment between two marks –known as gage section whose length is the gage length (GL) – is

recorded along with the instantaneous value of the force applied at every increment of time. Normally the force measurements are made automatically by the machine load cell and the elongation measurements by an extensometer or non-contact extensometer that provides more accuracy and consistent elongation readings until the specimen fails. FIGURE 1.2 shows a schematic of a tensile test device and the way the specimen is mounted between the grips.

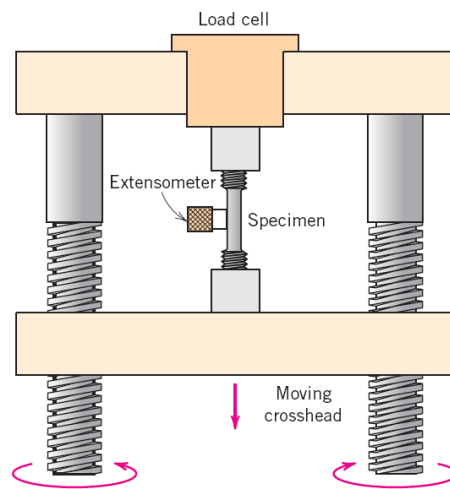


FIGURE 1.2: Schematic of the major frame of a tensile test device. The specimen is placed in the grips and pulled until fracture. The extensometer measures the change in length within the gage section from which the specimen strain is derived [1].

When the test finishes with the breaking of the specimen, a set of elongation-force data for each time increment will be the raw data output. This output is dependent on the particular geometry of the specimen that can have either a circular or rectangular cross section; the ends where the grips hold the specimen have relative large cross-section with respect to the GL in order to secure that the specimen breaks within the gage section. To eliminate the dependence of the experimental results such as the strength and ductility of

the specimen on specimen geometry, both elongation and the force are normalized to engineering stress and engineering strain respectively as follows:

$$\sigma = \frac{F}{A_0} \quad (1.1)$$

$$\epsilon = \frac{l_i - l_0}{l_0} = \frac{\Delta l}{l_0} \quad (1.2)$$

where F is the instantaneous applied force, A_0 is the initial cross-sectional area, l_0 is the initial gage length, l_i the instantaneous length and Δl the change in length or elongation. It is customary to refer to engineering stress, σ , and engineering strain, ϵ , as average longitudinal stress and average linear strain correspondingly [8]. It has been recognized that specimen dimension and geometry can strongly affect the accuracy of the stress-strain plot of a tensile experiment. This is particularly true if only cross-head displacement values are used to derive the strain [9, 10]. This is the fundamental reason for the standardization of mechanical testing.

The tensile test possesses some advantages respect to the other types of quasi-static mechanical testing [11]:

- The average longitudinal stress is nearly homogeneous within the gage section until just right before the onset of necking.
- Several very important mechanical properties can be derived from it (see below), and particularly the strength and the ductility are of primary concern.
- The deformation process – elastic and plastic – can be observed in a qualitative and quantitative manner.
- The performing of the test is relatively easy.

present in the material at low stress levels during the initial stage of the test. The first segment of the curve shows a proportional or linear relationship between stress and strain that is known as the Hooke's law, and the constant of proportionality (the slope of the line) is called the Modulus of Elasticity or Young's modulus, E ,

$$\sigma = E\epsilon \quad (1.3)$$

This linear relationship ceases to exist at some theoretical point known as the limit of proportionality, which is the stress value where the stress-strain curve first departs from linearity. Also another point would indicate the stress at which plastic deformation begins and this stress point is designated as the elastic limit. However, none of these two points can be very precisely ascertained since both depend on how accurately the strain can be measured during the test [13]. As such, the proportionality limit and elastic limit have no practical significance. To overcome this issue, in most engineering practices an offset stress is measured by constructing a straight line parallel to the elastic section of the stress-strain curve at a specific value of strain, 0.002 in most cases [14]. The offset stress obtained in this way is defined as the yield strength of the material, σ_y , or $\sigma_{0.2}$ where 0.2 corresponds to 0.2% permanent (or plastic) strain. In the case of a metal or material, particularly plastics with nonlinear elastic region some other method has to be applied. In some materials like annealed low carbon steels, the transition between the elastic to plastic behavior is demarcated by what is known as the yield point phenomenon. FIGURE 1.4 shows how the yield strength values in steels and other ductile metals are determined in practice. Here it should be pointed out that upon yielding, the total strain of the specimen has two components: the elastic strain and the plastic strain. Upon complete unloading, only the elastic strain is recovered.

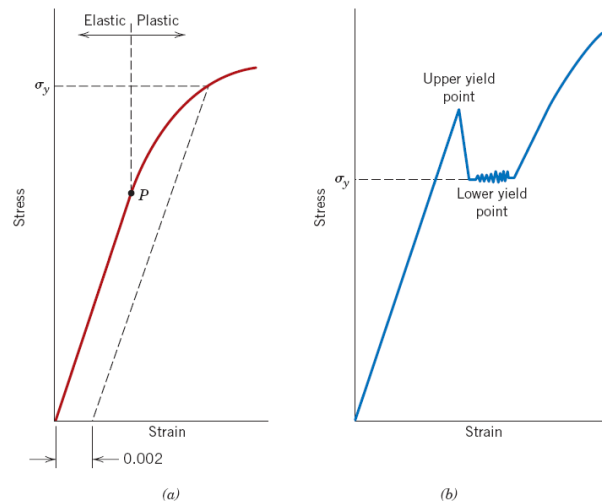


FIGURE 1.4: Determination of the yield strength in (a) ductile metals using 0.002 permanent offset strain and (b) typical curve for steel showing the yield point phenomenon [1]. In this case usually the lower yield point is taken as the yield strength of the steel.

Usually for an annealed metal, be it of FCC or BCC structure, after the set-in of plasticity, the stress value increases with plastic deformation in the specimen (the material strain hardens) until a maximum stress is reached. During this stage of uniform plastic deformation a constancy of volume is usually assumed, i.e.,

$$A_i l_i = A_0 l_0 \quad (1.4)$$

The original cross section of the tensile specimen A_0 , reduces along the gage length to A_i (an instantaneous value), while the specimen elongates from l_0 to l_i . The strain hardening compensates the reduce in the cross sectional area until, at some point in the specimen cross section, the effect of the decrease in the area is greater than the hardening effect of the specimen while straining, being this the weak point on which further plastic deformation will concentrate. This point is represented in the stress-strain curve as the maximum point known as the maximum tensile strength or the Ultimate

Tensile strength, UTS, which is the maximum value of stress that the metal can withstand under tensile loading. After this point, the plastic deformation is not uniform anymore; instead, it will be concentrated in a smaller region or neck and tensile instability begins. Now the cross sectional area is decreasing in a localized region more rapidly than the strain hardening effect can compensate and the value of the stress falls off until fracture occurs in the neck region. This phenomenon is known as *necking* and the final fracture will occur at the neck section at a stress value less than the UTS in the engineering stress-strain curve. It is worth to clarify at this point that the tensile strength or UTS is the maximum stress value in the engineering stress-strain curve, and at the same time, is the point until the plastic deformation is assumed to be uniform. In the case of ductile metals the value of UTS is reached right before the localized or non-uniform deformation (necking) begins, and in the case of brittle materials, the tensile strength will coincide with the fracture strength due to the little, or in some cases, vanishing plastic deformation that takes place in the specimen; this situation is illustrated in FIGURE 1.5 for ductile metals (a), less ductile (b), and completely brittle materials (c), from the left to the right.

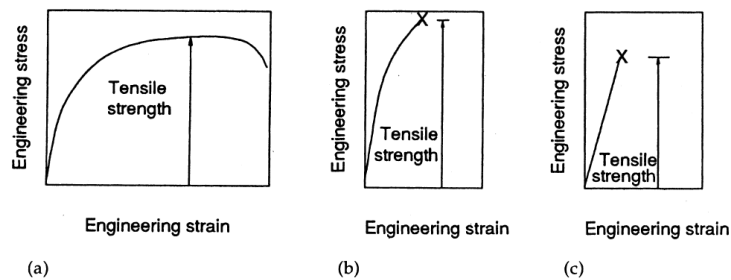


FIGURE 1.5: Schematic engineering stress-strain curves for different materials. (a) Ductile behavior with necking after the tensile strength (UTS) is reached. (b) Relatively brittle behavior and (c) completely brittle behavior. In (b) and (c) necking is not present, and the tensile strength is the fracture strength. In all cases the UTS is the maximum stress value [13].

Another very important parameter of mechanical property derived from the tensile test is the material's capability to withstand plastic deformation until fracture, known as *ductility*. There are two ways to measure ductility from the tensile test results. The first one involves measuring the engineering fracture strain represented by a parameter called the percentage of elongation to failure, % *EL*, that depends on the final length or length at fracture, l_f , of the GL whose original value is l_0 , i.e.,

$$\%EL = \left(\frac{l_f - l_0}{l_0} \right) \times 100 \quad (1.5)$$

The term within the parentheses is the plastic component, ϵ_{pf} , of the engineering fracture strain, ϵ_f , since the elastic strain is recuperated when the stress goes back to zero right after the fracture. It is a good practice to obtain these values from the data recorded in the tensile test, especially if the amount of plastic deformation is not significantly large, e.g., metals of low ductility or brittle metals, by using the following equation,

$$\epsilon_{pf} = \epsilon_f - \frac{\sigma_f}{E} \quad (1.6)$$

where σ_f is the average engineering fracture strength; equation (1.5) gives a closer calculation to the measurements made on the broken specimen after the tensile test and can be understood as a %plastic elongation = $100\epsilon_{pf}$.

The second parameter used to measure ductility is the percentage of reduction of area, %*RA*, which is the result of comparing the cross sectional area after fracture, A_f , with the original one, A_0 . It can also be expressed in terms of the diameter of the cross section, d , as follows:

$$\%RA = q100\% = \left(\frac{A_0 - A_f}{A_0} \right) \times 100 \quad (1.7)$$

$$or \%RA = \left(\frac{d_0^2 - d_f^2}{d_0^2} \right) \times 100 \quad (1.8)$$

These two parameters to measure the ductility of the specimen, % *EL* and %*RA*, can be related to each other only if there is no necking present in the specimen, i.e., as long as only uniform deformation takes place within the specimen. Otherwise the two parameters will not be directly related to each other anymore. There are examples where %*EL* is small but the %*RA* is still considerably large. This is particularly the case for a number of FCC metals with nanocrystalline (grain size $d < 100$ nm) or ultrafine grain (grain size $d > 100$ but < 1000 nm) microstructures [15-21]. The importance of ductility lies on how much plastic deformation a component will have before fracture and to what degree of deformation a work-piece can be taken before it fractures or cracks during a manufacturing process. However, usually, strength and ductility are two inter-exclusive properties. That is to say, high strength structural materials usually exhibit not so desirable ductility [22]. Examples are again to be found in ultrafine grain and nanocrystalline metals and alloys where the small grain sizes translate into very high strength, but often at the cost of much reduced ductility [23-27]. Hope is looming, though, to produce structural materials with concurrently high strength and decent ductility [28-30]. Lessons can also be learned from natural materials such as nacre which has a hierarchical structure and shows extremely improved toughness compared with its constituents [22, 31-33].

The stress-strain curves vary in shape for different materials and are affected by variables such as composition, history of thermo-mechanical processing, and the speed of

testing (strain rate), just to mention a few. The magnitudes of the mechanical properties mentioned above will also influence the stress-strain curve's shape.

1.2.2 True Stress – Strain Curves.

A real or true description of the deformation characteristics of a metal is not given in the nominal or engineering stress-strain curve, because the stress and the strain are based on the original or initial dimensions of the specimen and do not account for their continuous change throughout the test [34]. From FIGURE 1.3 (the engineering stress-strain plot) it may be incorrectly concluded that after reaching the maximum point (tensile strength), the metal becomes weaker because of the downturn of the stress until fracture. In reality, what happens after UTS is that the ductile metal specimen enters into the non-uniform plastic deformation zone and experiences plastic instability. Within a local region (the necking region), the cross-sectional area decreases quickly at the necking section; this decrease makes the load required to keep on elongating the specimen to lower down. Since the engineering average linear stress is based on unchangeable original dimensions, the ratio of load to original area (nominal stress) decreases consequently. However, what really happens during this stage is that the material continues to strain harden until the final fracture, making an actual or true stress value to increase until the final fracture as well. As such, the concepts of true stress and true strain should be based on actual dimensions, i.e., the actual cross sectional area of the specimen, ever decreasing after yielding, and actual gage length at every moment. Such actual parameters are the instantaneous quantities of the specimen during mechanical straining. This being said, the usefulness of the nominal or engineering curve is in applications with little total deformation, mainly elastic ones; on the contrary, the

true curve is more meaningful when dealing with large deformations, particularly when large plastic deformation is involved.

The plastic flow characteristics of a ductile metal are captured in the true stress-strain curve, where each point is considered the yield strength for that metal pulled in tension to that degree of strain corresponding to the stress value in question. For this reason, the true stress-strain curve is also known as the Flow Curve. In FIGURE 1.6 the initial flow stress, labeled as σ_{y0} , is the yield strength of the metal with no prior strain, and the curve will follow the trajectory OCDE. If the tensile test is stopped at some point after the initial yielding, the line DB (parallel to the elastic portion) will be followed and the specimen experiences some elastic recovery predicted by equation (1.6). After re-loading the specimen a new flow stress, σ_{yi} , will be reached at point D. The location of point D depends on how much plastic strain prior to re-loading the metal had, and the trajectory would be the same of that metal that was never unloaded, and therefore, will be following the path of DE. An equivalent situation to stopping the test after yielding is when a tensile test is performed in a metal with prior permanent deformation, for instance, in the amount of OB.

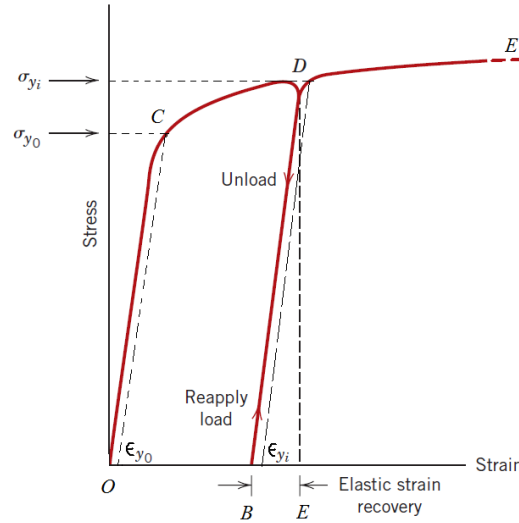


FIGURE 1.6: Schematic illustration of how the yield strength is affected by the amount of plastic deformation as if the metal would have been unloaded and reloaded again. Dashed lines parallel to the elastic portion are to obtain the yield strength, points C and D, for initial and re-loaded case respectively. Adapted from [1]

True stress, σ_T , is defined as the applied axial force divided by the current or instantaneous cross sectional area,

$$\sigma_T = \frac{F}{A_i} \quad (1.9)$$

To determine the true strain, ϵ_T , an integral of the incremental instantaneous strain, $d\epsilon_T$, over the current length has to be carried out as follows:

$$\epsilon_T = \int_{l_0}^{l_i} d\epsilon_T = \int_{l_0}^{l_i} \frac{dl}{l} = \ln\left(\frac{l_i}{l_0}\right) \quad (1.10)$$

The constancy of the volume in plastic deformation was expressed in equation (1.4), which can be rearranged and combined with equation (1.1) and (1.2) to relate the nominal stress to the true stress as follows:

$$\frac{l_i}{l_0} = \frac{A_0}{A_i},$$

$$\epsilon = \frac{l_i - l_0}{l_0} = \frac{l_i}{l_0} - 1 = \frac{A_0}{A_i} - 1 \therefore \epsilon + 1 = \frac{A_0}{A_i};$$

$$\frac{\sigma_T}{\sigma} = \frac{F}{A_i} \times \frac{A_0}{F} = \frac{A_0}{A_i} = \epsilon + 1,$$

$$\sigma_T = \sigma(\epsilon + 1) = \sigma \left(\frac{A_0}{A_i} \right) \quad (1.11)$$

Likewise, a relationship between the nominal strain and true strain can be established:

$$\epsilon_T = \ln \left(\frac{l_i}{l_0} \right) = \ln(\epsilon + 1) \quad (1.12)$$

Equations (1.11) and (1.12) relate the nominal values to the true ones of the stress and strain data which are valid for the uniform deformation case. In other words, they are valid up to the tensile strength in the engineering stress-strain curve. Only if the true strain is expressed in terms of the areas or diameters, then it will be valid until the fracture point as well;

$$\epsilon_T = \ln \left(\frac{A_0}{A_i} \right) = 2 \ln \left(\frac{d_0}{d_i} \right) \quad (1.13)$$

A representation of the relationship between a true and nominal (engineering) curve is shown in FIGURE 1.7(a) where the true curve departs from the nominal one as total strain increases. In FIGURE 1.7(b) the fact that the true curve may be obtained either from compression or tension test is depicted; if the material is the same, the two true curves should overlap or be very close to each other.

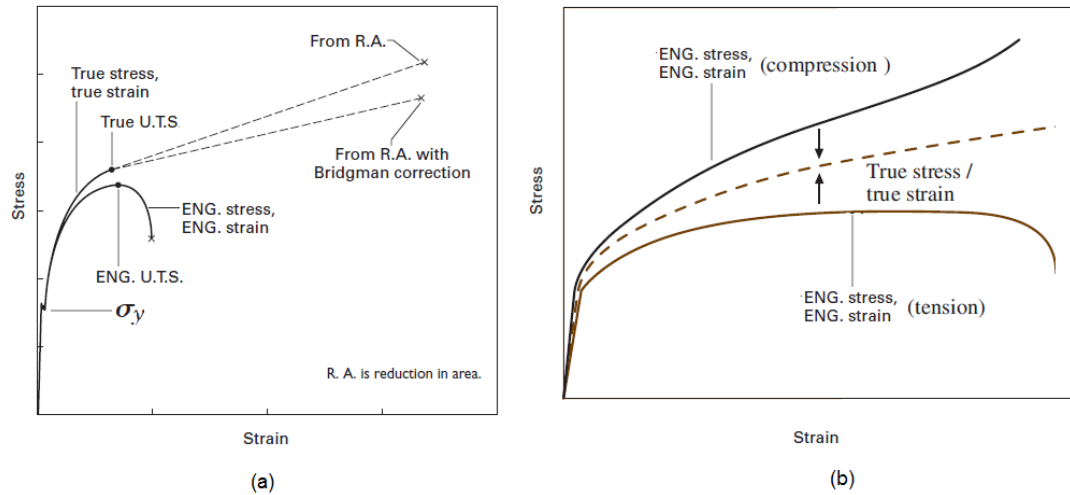


FIGURE 1.7: (a) Comparison of engineering and true stress strain curves. Adapted from [35]. (b) Tension True curve (flow) compared to that from compression test. Adapted from [35, 36].

It is worth to note that in the case of uniaxial tension the true curve is to the left of the nominal one until the UTS is reached, from which the curve is more or less linear up to the maximum load at the fracture point in some cases; its slope may continuously decrease until fracture in some others.

Some of the parameters that are determined from the true curve are presented in TABLE 1.1.

TABLE 1.1: Important parameters determined from the True Stress-strain curve.

Parameter	Description	Formula	
True stress at maximum load	Point for the onset of necking for most materials. A_u : cross sectional area of the specimen at maximum force.	$\sigma_{T_u} = \frac{F_{max}}{A_u}$	(1.14)
		$\sigma_{T_u} = \sigma_u \frac{A_0}{A_u}$	(1.15)
True fracture stress	Force at fracture divided by area at fracture. Must be corrected for triaxial state of stress.	$\sigma_{T_f} = \frac{F_f}{A_f}$	(1.16)
True fracture strain	Strain based on the original area and the area after fracture. A_f : cross sectional area at fracture.	$\epsilon_{T_f} = \ln \frac{A_0}{A_f}$	(1.17)
		$\epsilon_{T_f} = \ln \frac{1}{1-q}$	(1.18)
		q : Reduction in area (cylindrical specimens)	
True uniform strain	Based on strain up to the maximum load.	$\epsilon_{T_u} = \ln \frac{A_0}{A_u}$	(1.19)
True local necking strain	Strain required to deform the specimen from maximum load to fracture.	$\epsilon_{T_n} = \ln \frac{A_u}{A_f}$	(1.20)
Strain-hardening exponent, n	True curve representation between yield strength and the UTS is given by the Hollomon's equation (uniform plastic deformation region).	$\sigma_T = K \epsilon_T^n$	(1.21)
		K : the strength coefficient (material constant)	

1.3 Necking Behavior.

The equations mentioned so far apply when the metal exhibits uniform deformation, i.e., up to the maximum force during the tensile test. After reaching this point the specimen geometry changes, so does the stress state within the necking region. The non-uniform deformation, or necking area, is a localized region where most of the strains accumulate while the rest of the specimen undergoes negligible change in dimension. According to what is known as the Considère criterion [37, 38], at the onset

of necking, the specimen is in an unstable equilibrium when the total force reaches a maximum and decreases afterwards. In the engineering stress-strain curve, the onset of necking is signaled by reaching the UTS, that is, when the load bearing ability due to strain hardening is exceeded by the increase in stress due to the decrease in cross sectional area. The Considère criterion is then presented as

$$\frac{d\sigma}{d\epsilon} = 0 \quad (1.22)$$

Alternatively, the plastic instability condition can be expressed in the following manner:

$$dF = \sigma_T dA + Ad\sigma_T \quad (1.23)$$

where F is the applied force. Equation (1.23) can be rewritten as follows:

$$\sigma_T = \frac{d\sigma_T}{d\epsilon_T} \quad (1.24)$$

and assuming the constancy of the volume, then combining with equation (1.21), one has

$$\epsilon_{Tu} = n \quad (1.25)$$

This indicates that at the onset of necking the true strain (at maximum force) is numerically equal to the strain hardening exponent in the context of Hollomon equation. This exponent can then be taken to denote the onset of necking. FIGURE 1.8 illustrates the criterion on a true stress-strain curve as well as a nominal (engineering) stress-strain curve, both curves are plotted along with the strain hardening rate (right hand side in equation (1.24)). Also, one can notice that strain hardening continues even in local deformation after the onset of necking.

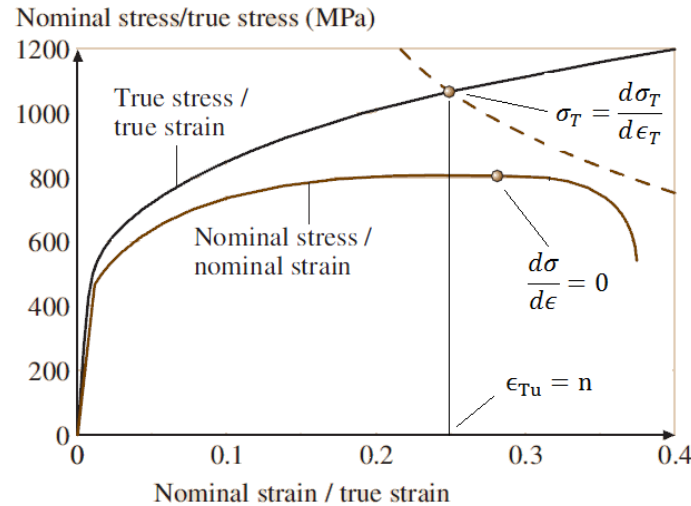


FIGURE 1.8: Considère criterion to illustrate the onset of necking. True and nominal stress-strain curves are plotted along with the strain hardening rate (dashed line in the upper right corner). Adapted from [36].

FIGURE 1.7 and FIGURE 1.8 depict the continuous increase of the true stress-strain curve after necking starts, and that the true strain at fracture can be much higher than the nominal total strain for a ductile specimen. The localized and rapidly decreasing cross sectional area requires its continuous measurement even after necking, and can be roughly approximated by obtaining a single point corresponding to the fracture point and joining it to the point of maximum force, as it is done by the upper dash line in FIGURE 1.7(a).

Because of the necking phenomenon, the stress condition in the tensile specimen within the necking region is no longer uniaxial due to the geometrical irregularity. Instead, the stress state in that region turns out to be a complicated triaxial stress condition, and the components of the stress tensor can be represented by a radial stress, σ_r , a circumferential stress, σ_θ , in addition to the longitudinal stress, σ_z . As it is

shown in FIGURE 1.9, the three stress components reach their maximum values at the center of the tensile specimen, with the circumferential and radial components, σ_θ and σ_r , approximately equal except close to the surface. The lateral contraction of the material at the center of the neck, when it is being stretched in the longitudinal direction, is impeded by neighboring disks of larger cross sections above and below it which are not deforming. In other words, the effect of this situation in the necking region is the replacement of uniaxial stress state by the existence of stress components in all three directions. The presence of the two additional components of stress raises the longitudinal component necessary to cause further plastic flow within the necking region. Therefore, the true stress at the neck (tensile force divided by minimum cross sectional area at the neck) is increased above what it would be if uniaxial stress state prevailed. That is to say, only a fraction of the axial stress, that exceeds the transverse stress, is effective in causing plastic flow.

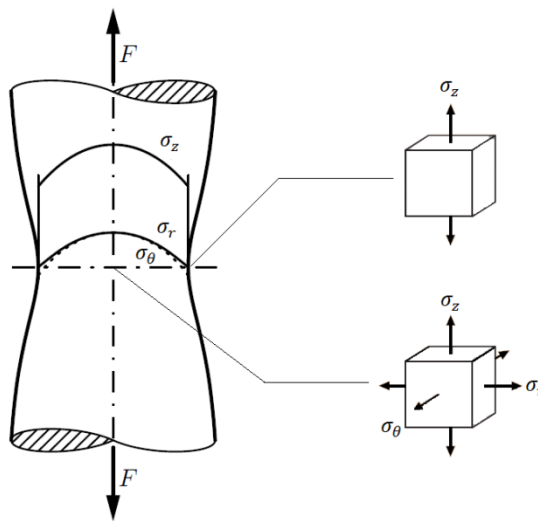


FIGURE 1.9: Triaxial stress state in a tensile specimen at the neck region showing longitudinal, circumferential and radial stresses [36, 39]

Since the true stress-strain curve gives information about the flow stress at any given strain, a correction has to be made to convert the actual triaxial stress state into a uniaxial one taking into account that the flow stress depends on the state of stress. The elemental cubes in FIGURE 1.9 illustrate the situation. This correction is much needed also in the context of fracture mechanics because the stress state in the crack tip region of a material, or the “process zone”, bears a lot of similarities to that of the necking region. Therefore, information and knowledge about the stress state, and the mechanical behavior of the material in question in the necking region is doomed to be essential for a good understanding of the fracture mechanics of the material. An attempt to provide a brief review of efforts toward this correction follows.

1.4 The Bridgman Correction of the Post Necking Stress – Strain Data.

Percy W. Bridgman [40] devised a method to correct the longitudinal stress that accounts for the presence of the transverse components (radial and circumferential). The following four assumptions are made [8]: i) the contour of the neck is approximated by the arc of a circle; ii) the cross section of the necked region remains circular during the test; iii) the von Mises criterion for yielding applies; iv) the strains are constant over the cross section of the neck. The main outcome of Bridgman analysis is a formula to calculate the flow stress that would exist during the tensile test if there was no triaxial stress state caused by necking, σ_{TB} ,

$$\sigma_{TB} = \frac{\sigma_T}{\left(1 + \frac{2R}{a}\right) \left[\ln\left(1 + \frac{a}{2R}\right)\right]} \quad (1.26)$$

In Equation (25), a is the radius of the tensile specimen at the thinnest section of the neck, and R is the radius of curvature of the neck profile as sketched in FIGURE 1.10.

Equation (1.26) can be re-arranged to show the Bridgman correction factor that will be denoted by B ;

$$B = \frac{\sigma_{TB}}{\sigma_T} = \frac{1}{\left(1 + \frac{2R}{a}\right) \left[\ln\left(1 + \frac{a}{2R}\right)\right]} \quad (1.27)$$

FIGURE 1.10 is a plot of Bridgman correction factor, $B = \sigma_{TB}/\sigma_T$, as a function of a/R according to equation (1.27).

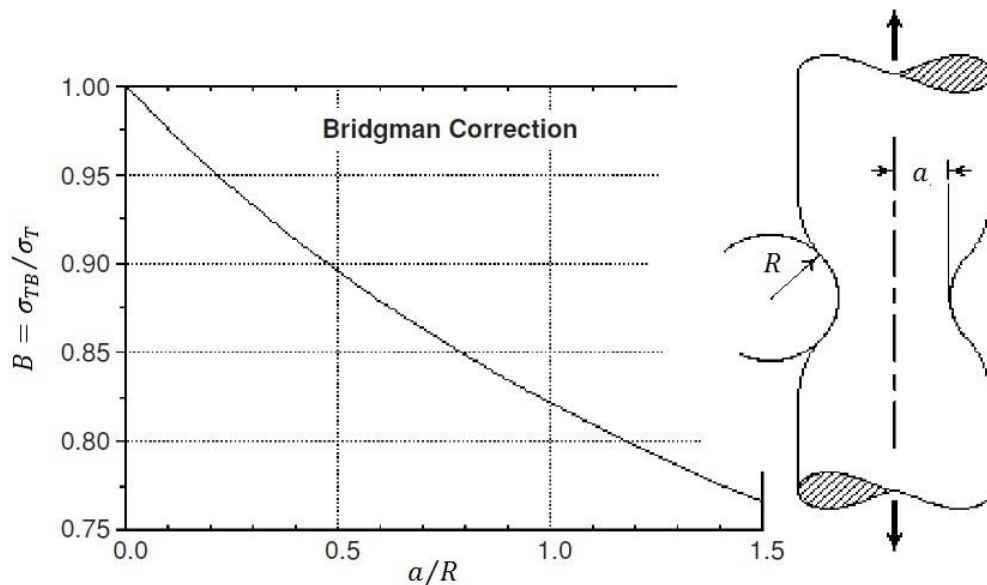


FIGURE 1.10: The Bridgman correction factor, B , as a function of the geometry of the neck (primarily the a/R ratio) [41].

It can be seen that the Bridgman correction parameter B is always less than unity, meaning that the corrected true stress curve should lie below the uncorrected one, which is traced extrapolating the true curve up to the point determined at fracture from measurements of the broken tensile specimen as shown in FIGURE 1.7(a). The empirical curve derived by Bridgman can be used to avoid continuous measurements of the geometrical parameters after necking starts. However, this curve is in close agreement

with experimental results only in the case of steels, and not for other materials with different necking strains. A curve that provides a closer correlation of the Bridgman correction factor with the necking strains is one that, instead of using a/R , is based on the necking strain, ϵ_n . This strain is nothing but the true total strain at the neck, minus the strain at the onset of necking or strain at maximum force, ϵ_{Tu} , equation (1.28). FIGURE 1.11 is a plot illustrating this closer correlation.

In light of the previous discussion, a more direct approach may be needed to derive a more accurate correction based on the strength of the material in the necking region and the strain therein.

$$\epsilon_n = \epsilon_T - \epsilon_{Tu} = \ln\left(\frac{A_0}{A_i}\right) - \epsilon_{Tu} \quad (1.28)$$

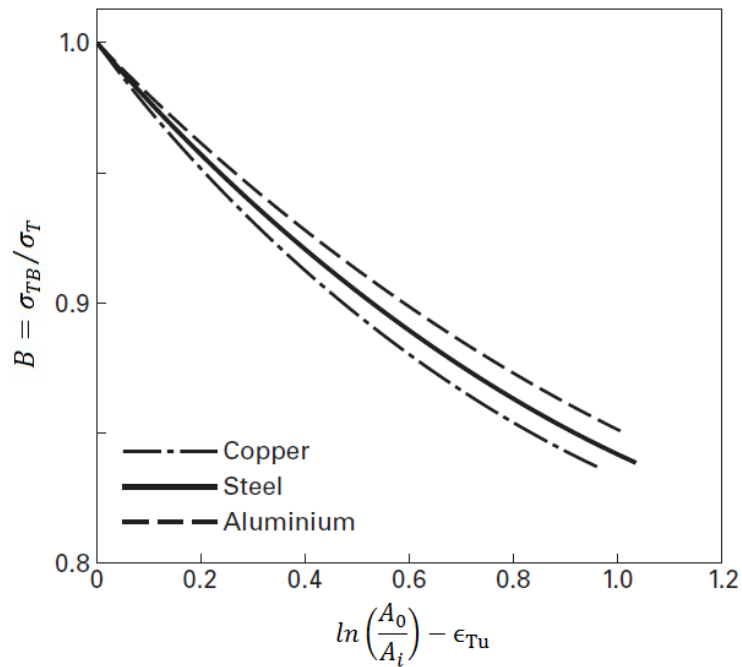


FIGURE 1.11: Bridgman correction factor as a function of necking strain ϵ_n [35].

1.5 Hardness of Metals.

Throughout the centuries hardness of a material has turned out to be a concept without a very clear definition. At first, it was only referred to as a qualitative property depending if the surface of the tested sample deforms or not. It has been associated to the results of two different types of tests: cutting and non-cutting methods. One particularity that the first devised tests had was that their values did not agree satisfactorily due to the complex mechanical and physical processes involved in such tests. The easiest way to test metals was to, by means of another apparently harder material, scratch the surface and then observed the characteristics of the groove or scratch. Actually, this method was followed by Mohs in 1812 to create a list of minerals based on their ability to scratch others. As a result, diamond seemed to be at the top of that scale because it was able to scratch any softer minerals after it. The idea of studying the scratches created on a metal by others leads to the concept of wear, which is not the subject of the research of this dissertation. As for non-cutting methods, the approach followed by Hertz in 1882 laid the foundation of the actual concept of static hardness. Hertz defined indentation hardness as the contact pressure in a small circular area at the elasticity limit caused by force perpendicular to the material surface. The area of contact mechanics started to emerge to solve some difficulties arising from the different mechanical responses of ductile and brittle solids [42]. Hardness is a property whose concept is very broad. It can be related to: resistance to indentation, the strength of the material, resistance to wear, and so on and so forth. Generally speaking, it gives information about the resistance of a material to *local* plastic deformation. This notwithstanding, a clear and commonly accepted definition of hardness is still open to discussion and investigation after theories,

simplifications and contributions of and from numerous researchers. Only indentation hardness will be dealt with in the research of the present dissertation.

1.5.1 Indentation Hardness Tests.

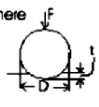
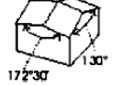
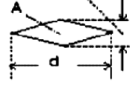
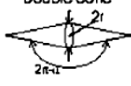
Indentation hardness of a material is evaluated by letting an indenter, of a specific shape, under a force F (perpendicularly applied) to penetrate into the surface of the material. When the load is removed, the residual contact area between the indenter and the surface is A . In this manner, indentation hardness of a material is defined as the ratio of the applied force or load (F) to the contact area (A) as

$$H = \frac{F}{A} \quad (1.29)$$

If A is the superficial area of the indent or the area of the remaining impression on the surface of the material, then the value of H will be considerably affected by the type and shape of the indenter. This is how a variety of test and techniques are differentiated from each other, i.e., Brinell, Ludwik, Grodzinski, Rockwell, Vickers and Knoop. TABLE 1.2 summarizes different methods to obtain static hardness of materials. Meyer proposed in 1908 to use the projected contact area A_c instead of that of the surface, giving a more physical meaning to hardness as the mean contact pressure between the surface of the indenter and the surface of the specimen. This definition is referred to as Meyer's hardness.

$$H_{Meyer} = p_m = \frac{F}{A_c} \quad (1.30)$$

TABLE 1.2: Static Indentation Hardness testing methods and the formulas involved [42].

Testing method	Shape of indenter	Shape of impression	Hardness value	Penetration depth
Brinell	Sphere 	Circle 	$H_c = \frac{2F}{\pi D^2 \{1 - [1 - (d/D)^2]^{1/2}\}}$ Brinell hardness number BHN; [F]=kg; [D], [d]=mm	$t = D[1 - [1 - (d/D)^2]^{1/2}] \approx d^2/2D$
Vickers	Tetragonal pyramid 136° 	Square  $d = (d_1 + d_2) / 2$	$H_v = \frac{2F \sin 68^\circ}{d^2} = \frac{1.8544F}{d^2}$ Vickers hardness number VHN; [F]=kg, [d]=mm	$t \approx d/7$
Knoop	Orthorhombic Pyramid 	Rhombus 	$H_k = \frac{F}{A} = \frac{14.40F}{d^2}$ Knoop hardness number KHN; [F]=kg, [d]=mm	$t \approx d/30.6$
Ludwik	Cone 90° 	Circle 	$H_L = \frac{4F \sin 45^\circ}{\pi d^2} = \frac{0.9F}{d^2}$	$t = d/2$
Grodzinski	Double cone 	Bangle 	$H_G = F/A_k = \frac{6rF}{\pi d^2} = \frac{0.9F}{\tan(\alpha/2)d^3}$ Double cone number $\alpha = 154^\circ$, $r = 2$ mm $HGN = \frac{2.77F}{d^3} \cdot 10^6$ [D]= μ m, $\alpha = 154^\circ$, [F]=kg	$t \approx d/80$ for $\alpha = 154^\circ$, $r = 2$ mm
Berkovich	Trigonal pyramid 142.3° 	Equilateral triangle  $A = a^2 \sqrt{3} / 2$	$H_B = F/A = 2F/a^2 \sqrt{3}$	$t \approx 0.19a$

1.6 Relationship Between Hardness and the Flow Curve of a Metal.

As hardness is usually understood as a material's resistance to local plastic deformation, one question naturally arises: What is the relationship between hardness and the material's overall mechanical behavior such as strength? The efforts to establish the link between hardness and the plastic behavior of metals dates back to Meyer's studies.

He states his empirical formula relating the load and the size of the indentation, known as Meyer's law

$$F = kd^{n'} \quad (1.31)$$

where F is the applied force in kgf; d is the diameter of the indentation in mm; n' is a material constant related to strain hardening of the metal (also known as Meyer index), and k is a material constant indicative of the metal's resistance to penetration. The exponent in equation (1.31) is related to the strain hardening exponent n , being approximately $n + 2$ (the hardening exponent n is to be understood in the context of Hollomon equation). Previously, Brinell had found another empirical relation for steels, with a wide range of carbon content, linking the ultimate tensile strength (UTS) to Brinell hardness number: $\sigma_u = 0.346 \cdot BHN$. It was not until the first paper of David Tabor about hardness [43] in which Tabor points out that a ball indentation initially led to elastic strain, then plastic strain and correspondingly strain hardening, to a final elastic recovery after removing the load. Tabor's work is based on the Hertz model for elastic contact deformation of spherical bodies, along with his own measurements [44].

Tabor showed particular interest in the relation between Brinell hardness and the tensile strength of a metal. He applied continuum mechanics theory (plane-strain indentation in a rigid-plastic material) to the plastic stage of the indentation process. As a result, he found a constant ratio between the mean contact pressure, p_m , and the uniaxial yield stress, σ_y . Observing that hydrostatic pressure does not produce plastic flow, this should only be associated with a critical resolved shear stress of the metal. Qualitatively speaking, he concludes that about two-thirds of the mean contact pressure, p_m , is in the form of hydrostatic pressure, and therefore, does not contribute to plastic flow. In other

words, the plastic flow of a material under indentation is produced by the remaining one-third of the contact pressure, i.e., $\frac{1}{3}p_m = \sigma_y$. For the hardness methods that utilize the projected contact area, the hardness number, H , is taken directly from the mean contact pressure p_m . As such, one-third of the hardness would be equivalent to the flow stress (yield strength in this case). In other words and for a general case, the mean contact pressure or hardness is directly proportional to the yield strength or flow stress of a metal in uniaxial compression, such that

$$H = C\sigma_y \quad (1.32)$$

The presence of a considerable hydrostatic component in an indentation stress field is due to the surrounding matrix that constrains the material zones affected by the indentation. Thus, the mean contact pressure is higher than that required in yielding in a uniaxial compression test. For this reason C in equation (1.32) is called the *constraint factor*, which is influenced by the type of indenter, the material being indented and other experimental parameters [45]. Theory and experiments have shown quite consistently that $C \approx 3.0$ for metals, which have large ratios of E/σ_y (or the elastic strain, where E is the Young's modulus and σ_y is the yield strength). For materials with lower ratios of E/σ_y , as in glasses, $C \approx 1.5$. It is worth mentioning at this point that the flow stress, or the yield stress of a material is the value of the stress at which plastic yielding or plastic flow first occurs for a specific state of the material in question. Even though C is only a constant relating hardness to the flow stress, it has been the subject of numerous scientific researches trying to explain its origin, its physical picture and accurate value by modifying the parameters mentioned above. Tabor's experiments started with analyzing results from spherical indenters, since such indenters can provide important information

about elastic and plastic properties of the material when the mean contact pressure (indentation stress) is plotted against the ratio d/D (indentation strain), where d is the contact area radius and R is the indenter radius. Depending on the indentation stress-strain response of the material, three regimes can be distinguished [45]:

- $p_m < 1.1\sigma_y$: Full elastic response, temporary deformation.
- $1.1\sigma_y < p_m < C\sigma_y$: Only plastic deformation beneath the surface constrained by the elastic surrounding material matrix.
- $p_m = C\sigma_y$: There is no increase in the mean contact pressure with increasing indenter load and plastic region extends to the surface of the tested material.

Tabor suggested that strain distributions would be similar if those were the product of geometrically similar indentations. Therefore, a ‘representative strain’ proportional to the ratio d/D might serve to characterize the strain field. Subsequently, using available experimental data, he demonstrated that geometrically similar indentations in a strain hardening metal yield equal values of the mean contact pressure as it is illustrated in FIGURE 1.12. After these results, Tabor envisioned the similarity of this curve with the plastic region of the true stress-strain curve, and later on showed that using equation (1.32), with $C = 2.8$ and a representative strain of $0.20d/D$, the points will lay on the flow curve for the strain hardened material subjected to increasing amount of plastic strain. See FIGURE 1.13.

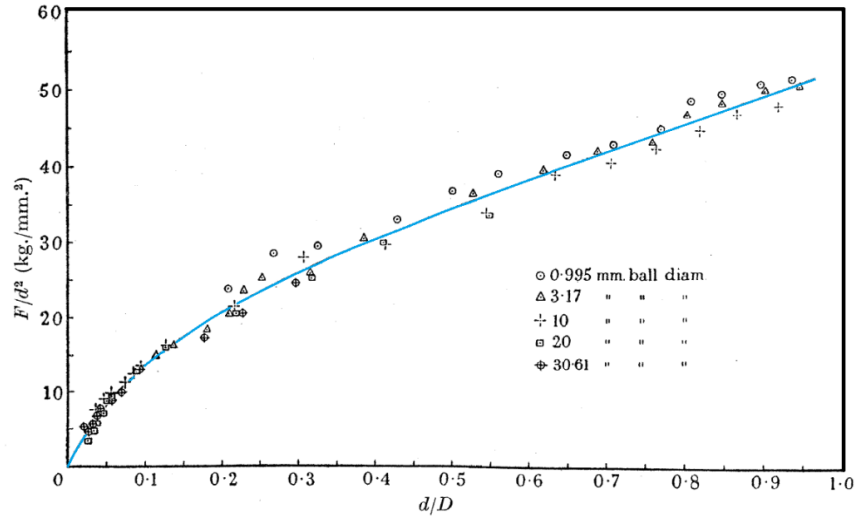


FIGURE 1.12: Mean contact pressure vs. indentation strain of annealed copper for various indenter diameters [43].

Although it is an empirical method, it has been demonstrated to be in good agreement for several metals. Because of this, it has been used as an alternative method to derive tensile properties when not possible otherwise. Equation (1.32) has proved to be a good estimate for some metals that strain-hardens, i.e., metals that do not have a well-defined yield stress. For such metals, σ_y is replaced by σ_r which is called 'representative (equivalent) stress', a value that is the flow stress at a given value of true strain named the representative (equivalent) plastic strain, ϵ_r . Tabor showed that the representative strain for geometrically similar indentations made by pyramidal Vickers indenter was about 0.8 (8%). Tabor's model has served to demonstrate the correlation between hardness and tensile or compressive stress-strain properties, the variation of hardness observed in strain-hardening metals (pointed out by Meyer as well), and differences that have arisen when utilizing indenters with different geometries.

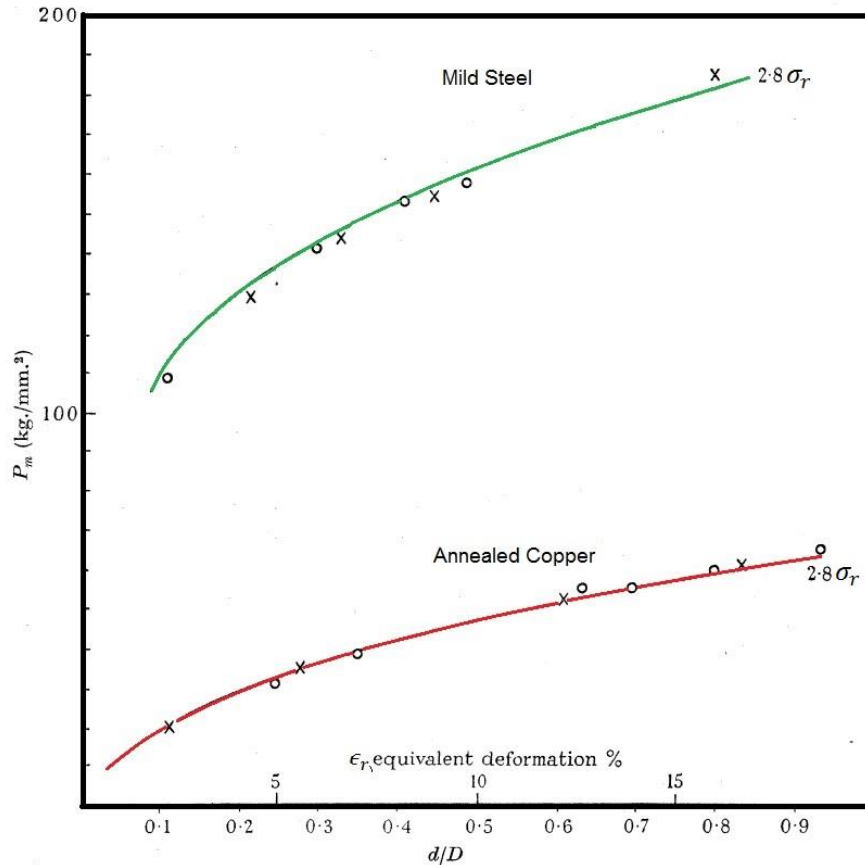


FIGURE 1.13: Comparison of flow curves obtained from hardness measurements (points) with flow curve obtained from compression test (solid curves) for a mild steel and an annealed copper [43].

The success of Tabor's approximation relies on its simplicity and applicability, since complex stress distributions generated during the indentation process have made it difficult to establish a direct relationship between such complex stress distributions and the stress distribution in the tension or compression test. Some models aiming to find such a relationship are worth to mention briefly at this point. The expanding cavity model (ECM) developed by Johnson [46] relies on the assumption that plastic deformation caused by an indentation has a radial and a tangential component, and the model focuses on the radial expansion of the plastic zone by disregarding the amount of material piled

up around the indentation. An alternative for the ECM is given by Shaw and DeSalvo [47] who concluded that the plastically deformed region in their bonded-interface specimens were elastically constrained, and the volume displaced by the indenter is taken up by elastic displacements. The plastic zone is restricted to advance through the boundary of a contact circle at the specimen surface. No quantitative data is presented. Instead, they suggest a method to determine the constrained factor independent of the strain. In the rigid-plastic slip line theory, the material displaced by the indenter is accommodated by upward flow around the indenter. Plastic yield within such a material depends upon a critical shear stress calculated either by the Tresca or the von Mises criteria of yielding. After the models suggested by different groups, it is accepted that the deformation caused by an indentation depends on the characteristics of the indenter and the material to be tested. If the indenter is sharp, the included angle will play an important role. For the case of spherical indenters the tangents to the surface at the points of contact will depend on the applied load. In both cases (of sharp indenter and spherical indenter), the ratio E/σ_y will also affect the type of stress field and strains generated, and will dictate the applicability of one model or another.

1.7 Instrumented Nanoindentation Testing – Indentation Hardness.

Instrumented indentation generally refers to the process of continuous recording of the depth of penetration as the load is applied to the indenter. In contrast to any static hardness methods mentioned earlier in this chapter, in which the size of the residual impression is measured after the test, instrumented indentation allows the application of a force or displacement history in a controlled manner over a complete cycle of loading and unloading. The main outcome of such an experiment is a load–displacement curve from

which hardness and elastic modulus can be derived. Furthermore, other mechanical properties, such as strain hardening exponent, fracture toughness, stress-strain behavior, among others, can be obtained as well without the need to measure the impression optically but can be derived based on high resolution instrumentation. Other names used to refer to this technique include: depth sensing indentation, continuous recording indentation, ultra-low load indentation, and nanoindentation if the depth of penetration of the indenter is just a few microns or even in the nanometer range as in the case of thin films. The main objective of the instrumented indentation method or nanoindentation (both terms will be used indistinctively in this study) is to obtain the elastic modulus and hardness of the specimen, based on a method proposed by Doerner and Nix [48] and subsequently refined by Oliver and Pharr [49], based on the unloading portion of the load-displacement curve recorded during the test. That method was thought to be used with sharp geometrically similar indenters. It has been used with different axisymmetric indenters including spherical ones. For the particular case dealt with in this research, the Berkovich indenter (described later in this section) is utilized and it is customary in finite element analyses to be modeled by a conical indenter with a half-included angle, $\phi = 70.3^\circ$.

FIGURE 1.14 illustrates a schematic of a typical load-displacement ($P - h$) curve obtained with a Berkovich indenter. The curve is composed of an elastic-plastic loading while the permanent impression is formed, a small period of holding time at the maximum load (not shown in the curve) to compensate any creep effects, and finally the unloading part which is assumed to be completely elastic.

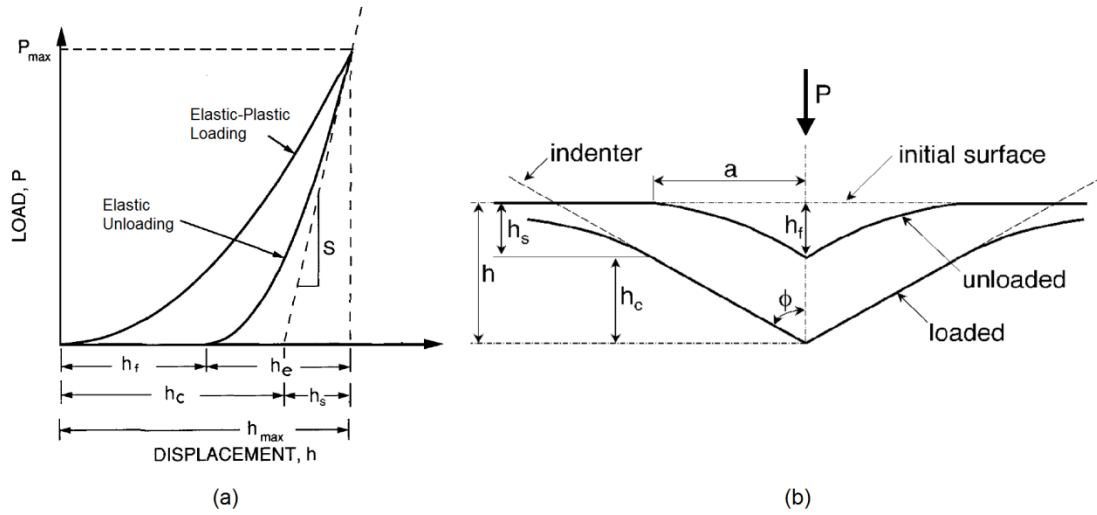


FIGURE 1.14: (a) A typical load-displacement curve (schematic) from a Berkovich indentation experiment. (b) Cross-section profile of the specimen surface during the indentation process [50]. h_f : depth of the residual impression. h_e : elastic displacement recovery during unloading. h_c : depth of the contact of the indenter with the specimen at P_{max} . h_s : sink-in of the surface at P_{max} . h_{max} : Maximum indentation depth at P_{max} . a : radius of the contact circle. P : Normal load on sample. S : Contact stiffness (slope of the unloading part). ϕ : half included angle of the indenter.

The relationship between displacement into surface, h , and force or load, P , during unloading is approximated by the power law form:

$$P = \alpha(h - h_f)^m \quad (1.33)$$

where α is a constant influenced by the geometry of the indenter, the sample elastic modulus, E , and Poisson's ratio, ν , the indenter elastic modulus, E_i , and Poisson's ratio, ν_i ; h_f is the final displacement or permanent unloading depth, and m is the power law exponent that depends on the indenter geometry, and is generally between 1 and 2 (2 for a cone-shaped tip). The final displacement, h_f , is one of the important quantities measured from the $P - h$ curve; the contact stiffness, S , is another quantity that it is

defined as the slope of the unloading curve at the maximum loading point, i.e., the derivative of the load with respect to the displacement at P_{max} , given by

$$S = \left(\frac{dP}{dh} \right)_{P_{max}} = \beta \frac{2}{\sqrt{\pi}} E_r \sqrt{A_c} \quad (1.34)$$

In Equation (33), A_c is the projected contact area; β is a dimensionless parameter including deviations in stiffness due to lack of axial symmetry and other physical processes affecting the stiffness. Normally β has a value of unity, but $\beta = 1.034$ is suitable for Berkovich indenter, and E_r is the reduced or combined modulus that accounts for elastic deformation of both the indenter and the sample and is given by

$$\frac{1}{E_r} = \frac{(1 - \nu^2)}{E} + \frac{(1 - \nu_i^2)}{E_i} \quad (1.35)$$

This equation represents the compliances for the elastic compression of two solids in contact added in series. The applicability of the method is limited since it is based on Sneddon's model for the indentation of an elastic half space with a rigid punch and does not account for the pile-up of the material around the periphery shown in elastic-plastic materials. Making the assumption of negligible pile-up, the amount the surface sinks-in is given by

$$h_s = \varepsilon \frac{P_{max}}{S} \quad (1.36)$$

where ε is a constant dependent on the indenter geometry. For the current case $\varepsilon = 0.75$. Observing FIGURE 1.14, the contact depth can be found by subtracting the sink-in of the surface from the maximum depth as follows

$$h_c = h_{max} - \varepsilon \frac{P_{max}}{S} \quad (1.37)$$

In order to accurately determine the contact stiffness at the maximum load the frame compliance of the system must be accounted for. Finally, the area function of the tip has to be determined by analyzing the geometry of the Berkovich indenter that is depicted in TABLE 1.2 and zoomed in FIGURE 1.15. From this FIGURE, we can see that the depth of penetration can be related mathematically to an area for the specific geometry shown. The original geometry of the Berkovich indenter with a pyramidal geometry can be transformed into an equivalent cone that gives the same area-to-depth ratio as the original.

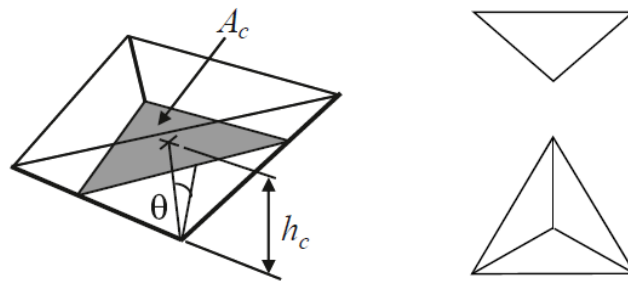


FIGURE 1.15: Berkovich indenter geometry [51]. The shaded area shows the projected contact area that depends on the contact depth at a given time during the indentation.

The so called indenter area function or indenter shape function is given in terms of the original geometry with a face angle $\theta = 65.27^\circ$

$$A_c = 3\sqrt{3}h_c^2 \tan^2 \theta \quad (1.38)$$

For the equivalent cone indenter with a half-included angle $\phi = 70.3^\circ$, one has

$$A_c = \pi h_c^2 \tan^2 \phi \quad (1.39)$$

Once the contact depth, and in turn, the contact area is determined, equations (1.38) or (1.39), the indenter function can be determined as well. In this manner the modulus (indentation modulus) can be computed from equation (1.34) and (1.35). Finally, hardness (indentation hardness) is calculated from

$$H_{IT} = \frac{P_{max}}{A_c} \quad (1.40)$$

1.7.1 Pile – up and Sink – in Behavior.

Depending on the plastic behavior of the test specimen, the material may sink in, i.e., the specimen surface is drawn inwards and downwards under the indenter's tip, or the material may pile up, i.e., the material flow upwards around the indenter's periphery. These two situations are depicted in FIGURE 1.16. If pile-up occurs, the actual contact area is greater than predicted by the method described above, leading to an overestimation of the indentation modulus and the indentation hardness. The discrepancy is due to the way the indentation was modeled based on the model for elastic contact. The behavior is mostly affected by the ratio E/σ_y and the strain hardening properties of the material. A large E/σ_y ratio and a low or zero strain hardening coefficient will produce the greatest pile-up. Such materials include, for instance, soft metals already cold-worked at the time of indentation. Pile-up is inhibited by the ability of the material to strain-harden, i.e., materials with relatively high values of the strain hardening exponent n . For materials with a low value of the ratio E/σ_y , the plastic zone is restricted within the circle of contact. As such, sink-in is more likely to occur and the method described above already takes it into account.

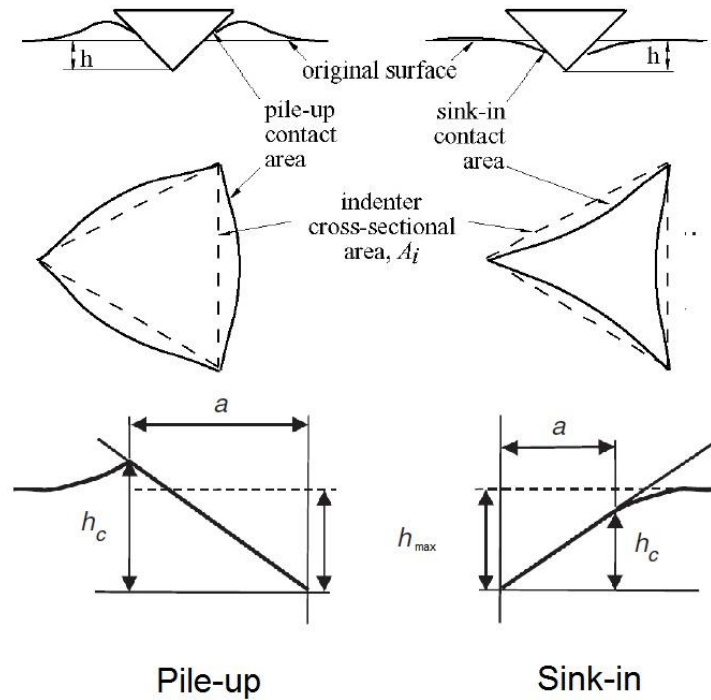


FIGURE 1.16: Sink-in and pile-un during indentation. The actual contact area differs from that one predicted by the calculation of the contact depth [51].

The factor that affects the accuracy of the nanoindentation data the most is the piling-up effect and it has not been resolved satisfactorily. Efforts can be found in the literature to deal with this issue [52-54]. The piling-up behavior can be anticipated by measuring the ratio of the final indentation depth, h_f , to the depth of indentation at maximum load, h_{max} [55]. From the $P - h$ curve the ratio h_f/h_{max} can be measured, with outcome values $0 \leq h_f/h_{max} \leq 1$. The lower limit will indicate fully elastic deformation and the upper one will show rigid-plastic behavior. FIGURE 1.17 shows the results of a finite element simulation for a material with a ratio $E_r/\sigma_y \approx 653$ and zero strain hardening rate ($n=0$). We can see that pile-up is large when the h_f/h_{max} ratio is close to unity, and when $h_f/h_{max} < 0.7$, little pile-up is observed in the simulation.

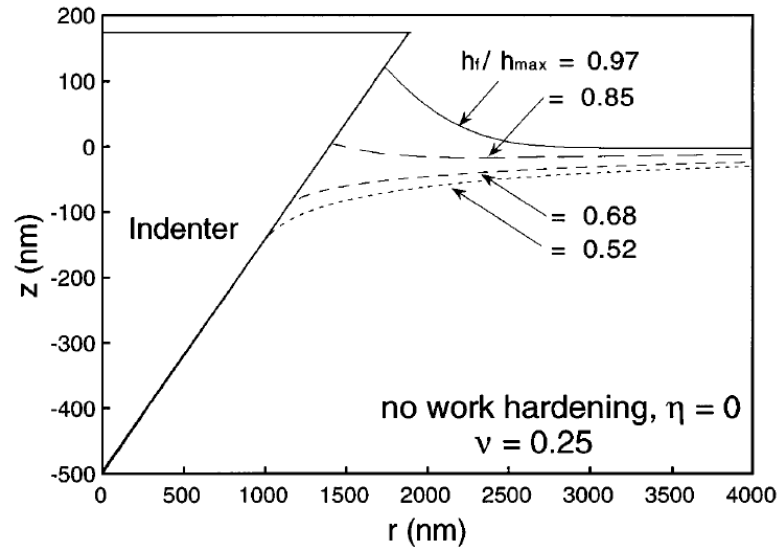


FIGURE 1.17: Indentation profile for a non-strain hardening material. In this FIGURE, z represents the indenter axis direction and r represents the radial direction for cone indentation [55].

The more reliable method to eliminate the influences of pile-up on the results is to measure the contact area directly [53, 54]. For instance, atomic force microscope (AFM) imaging can be helpful in finding the actual contact area. But this process is quite time consuming and is thus not so convenient in terms of the time invested. What is worse, this process renders all the advantages of the instrumented indentation method, and it is a step backwards going back to the conventional hardness methods outlined earlier in this chapter.

One method that does not require imaging of the impression is based on the observation that the ratio of load to stiffness squared (P/S^2) is a measurable parameter and this ratio does not vary with indentation depth. In other words, it should be constant and independent of the contact area [56]. Combining equations (1.34), (1.35) and (1.40) one can obtain

$$\frac{P}{S^2} = \frac{\pi}{(2\beta)} \frac{H_{IT}}{E_r} \quad (1.41)$$

Notice that this is independent of pile-up and sink-in behavior. The advantage of equation (1.41) is that if the material tested has a known elastic modulus, then this would be the input to calculate accurately the indentation hardness disregarding pile-up. Or the other way around, if the indentation hardness is known, then the indentation modulus can be estimated. In the case that both material properties are unknown then equation (1.41) cannot be applied.

1.7.2 Indentation Size Effect (ISE).

Experimental results have shown that indentation hardness and/or modulus vary with indentation depth when one would expect single values for both properties for isotropic materials [57]. This effect can either be intrinsic or extrinsic, depending on the materials of interest. Some causes are attributed to the hard superficial oxide films formed with different properties from those of the bulk material, to the presence of residual stresses and strain hardening from previous mechanical processing like polishing, to friction between the indenter and the sample, among others. Such effects are naturally extrinsic and may be eliminated by careful preparation of the specimen. However, for intrinsic size effect, the scenario becomes more complicated. In materials exhibiting this effect the plastic flow is affected by the strain and strain gradient. Hardness increases with the decrease in indentation depth. That is, shallower indentations produce high hardness values due to the nucleation of dislocations within the plastic zone. These dislocations may either be statistically stored or geometrically generated. The presence of these dislocations raises the yield strength of the material leading to an increase in hardness. As indentation depth decreases, the number of geometrically

necessary dislocations (GND) increases, leading to an expression to calculate the hardness, H_{IT} , in terms of that hardness obtained without the presence of GND, H_o , and of h^* that is the length that characterizes the depth dependence of the hardness [58].

$$\frac{H_{IT}}{H_o} = \sqrt{1 + \frac{h^*}{h}} \quad (1.42)$$

Some researchers [59] have demonstrated the existence of a critical depth below which the surface effects affect in a great manner and rule the load-displacement behavior. At even greater depths, bulk processes govern the behavior and corresponding results.

1.8 Motivation of this Research.

Since the works of P. W. Bridgman on metals under high pressure, large plastic flow and the stress state at the neck in a tensile test specimen, large plastic deformation [40] has been the subject of numerous studies especially in the area of manufacturing processes and fracture mechanics.

In any metal forming process, the final shape of the work piece is obtained by plastic deformation. Therefore, the plastic flow properties of metallic alloys and the stresses and strains induced during the forming processes are key factors for optimizing such processes. Computer simulation techniques have been developed in order to save time, the raw material and to make more efficient the aforementioned processes. The accuracy of the simulations will depend on the inputs given, i.e. plastic properties of the working material.

Plastic deformation is also present in the fracture mechanics associated with a crack tip of ductile materials. The propagation of such cracks depends on how the

surrounding plastically deformed material is able to accommodate the high stresses associated with the crack tip (the process zone) [35]. Stress triaxiality (three dimensional state of stress) and plastic deformation govern the process of ductile fracture [60].

In either of the two cases mentioned above, a fundamental and better knowledge of the plastic properties and of the three dimensional stress state, that reflects the particular condition of the material, must be known in order to anticipate the actual behavior during simulations or characterization of the mechanical behavior of the material. This knowledge is usually extracted from the true stress – strain curve of the material in which the actual plastic behavior is represented. In addition to it, stress triaxiality is represented by the necking phenomena existent during the last stage of a tensile test of a ductile material.

In addition to the tensile test, the true stress – strain (σ_t, ϵ_t) curves can also be obtained by means of compression, indentation, torsion and notch tensile tests. Finite element analysis (FEA) is a computational tool to extract the curves as well. Among these methods, the tensile test is the one that can reach the maximum strain value at the neck section (more than 1.0), where the cross section is the smallest right before the material fails (ductile fracture).

A complete characterization of the necking phenomena will shed light on the understanding in a better manner of the combined effects of large plastic deformations and stress triaxiality in metallic materials.

1.9 Research Objectives.

This research project has proposed a new method to correct the post-necking section of the true stress-strain curve of a tensile experiment of a ductile specimen. We

take advantage of the well-established relationship between hardness and flow stress, utilizing the powerful technique of instrumented indentation (nanoindentation in this case) to match each value of the flow stress in the curve to the indentation hardness along the axial direction of the broken tensile specimen. The key parameter in this match will be the representative plastic strain even though a clear definition and/or interpretation is still a matter under debate. A reverse analysis will be performed to achieve consistency between the properties before and after necking phenomenon starts. Lastly, the versatility of the nanoindentation technique in characterizing plastic behavior of materials will be proved by studying the strain rate sensitivity of copper that has been subjected to severe plastic deformation (SPD), particularly, equal channel angular extrusion (ECAE).

1.10 Organization of this Dissertation.

The dissertation is a logical sequence of the research, presented in each chapter; the topics and concepts needed to devise the method proposed are articulated with the theory and the experimental part. The outcomes are provided in a way that the new contributions are supported on previous works but at the same time distinguishing from them. Chapter 2 provides the necessary background and basic concepts about the type of analysis performed. The relationship between flow stress and hardness in Tabor's relationship frames the importance of the concept of representative plastic strain, which in turn, supports the approach followed. Chapter 3 deals with the materials used and methods executed in the process of achieving the objectives; these include: tensile and compression test, design and cutting of the samples specimen, and instrumented nanoindentation. Chapter 4 presents in a detailed manner the experimental results for the materials tested while discussing the findings and observations. Chapter 5 introduces the

application of the instrumented nanoindentation technique to study the mechanical properties of Equal Channel Angular Extruded copper. Finally, chapter 6 summarizes the conclusions and remarks, and some ideas for future work as well.

CHAPTER 2: PROPOSED METHODOLOGY

The two types of analyses utilized to relate hardness and flow stress are forward and reverse analysis. Key considerations in this study include characteristic or representative plastic strain and the constraint factor.

2.1 Forward and Reverse Analysis

Forward analysis consist of deriving the hardness characteristics, mainly the load-displacement curve, from the elasto-plastic properties extracted from conventional testing methods like those mentioned in chapter 1. Typically this analysis is done using the finite element method [61-65]. On the other hand, reverse analysis consists of deriving elasto-plastic properties from indentation information on the load-displacement curve [63, 66-74]. Reverse analysis is more complex than forward analysis mentioned previously and is based on instrumented indentation analyses.

The forward analyses have focused on modeling the loading part of the load-displacement curve as parabolic based on experimental results:

$$P = Kh^2 \quad (2.1)$$

where the proportionality constant K varies depending on the materials elasto-plastic properties and the type of indenter used. Curve fitting is used to obtain this relationship. Equation (2.1) is commonly referred to as Kicks law (Kicks, 1885). It is assumed that K is related to the hardness H and the elastic modulus E . An expression was derived by

Hainsworth et al [61] for a Berkovich indenter showing that the loading curve may be fitted to

$$P = E \left(\phi \sqrt{\frac{E}{H}} + \psi \sqrt{\frac{H}{E}} \right)^{-2} \cdot h^2 \quad (2.2)$$

where ϕ and ψ are indenter constants. However, the equation does not fit the experimental results very well, then, a polynomial function may be used instead [70, 75]. Another issue involving forward analysis is that two materials with different elasto-plastic properties can generate the same curvature K for the same indenter geometry modeled.

Reverse analysis, despite being more complex, has been the scope of study for many research groups after the works of Tabor [43, 76]. Researches were seeking to find an empirical and/or theoretical model to correlate hardness measurements with stress-strain data. The reason behind this is the advantages of performing indentation tests rather than tensile tests due to the convenience of the former being non-destructive, faster and simpler. Also, indentation tests can be performed without requiring specific geometry and cut back significantly on the amount of material used compared to the tensile test.

2.2 Applicability of Tabor's Relationship

It was mentioned in chapter 1 that by performing experiments on mild steel and copper, Tabor found a relationship between flow stress and hardness (spherical and Vickers). Realizing that the flow stress was the hardness value divided by 3, the constraint factor C was equal to 3. This idea has proved to be useful when dealing with perfectly plastic materials (first case), where the stress is independent of the strain and thus, making the yield strength equal to the flow stress. Tabor's empirical relationship

has been applied for all kind of materials regardless of the thermo-mechanical processing history, the stress-strain behavior, and sometimes, of the type of hardness measured. For instance, in the case of work hardening (strain hardening) materials (second case), the flow stress increases with any amount of plastic deformation induced in it, such as during the indentation process itself, making it larger than the yield strength σ_y . A third case is present when hardness measurements are performed on metals with certain amount of plastic deformation (pre-deformed); in such case, the flow stress is wrongly obtained by dividing the hardness measured by 3 in a straight manner. Tabor's equation can be generalized in a way that can still represent the relationship between hardness and flow stress, taking into account the type of material and the plastic deformation previous to the indentation ϵ_0 . TABLE 2.1 shows the cases just described.

TABLE 2.1: Possible scenarios where Tabor's relationship may be applied. The relationship between hardness and flow stress still holds.

Case	Material	Description	Equation
1	(Elastic) Perfectly Plastic	The stress is constant and equal to the yield strength independent of the strain	$H = C\sigma_y \quad (2.3)$ $C = \frac{H}{\sigma_y} \approx 3$
2	Strain Hardening	If the material is indented, the flow (yield) stress increases depending on the strain field under the indenter tip	$H = C\sigma_r(\epsilon_r) \quad (2.4)$
3	Deformed Strain Hardening	The amount of initial plastic strain affects the flow stress as well.	$H = C\sigma_r(\epsilon_0 + \epsilon_r) \quad (2.5)$

In case 2 above, the yield strength σ_y , is replaced by a representative flow stress σ_r , which in turn reflects the strain gradient under the indenter tip in a strain hardening material. In other words, the average contact pressure is linked to a

representative value of the stress inside that plastic zone. The representative stress is a function of a parameter called representative plastic strain of the material ϵ_r . In case 3, the representative stress is a function of the total strain composed of the initial plastic strain plus the representative plastic strain. The equations on the rightmost column show a linear relationship between hardness and (flow) stress through the constraint factor C .

2.3 Representative Plastic Strain

This parameter, also called characteristic strain, indentation strain and offset strain among the mechanics and materials communities, is of great importance in the area of contact mechanics of elasto-plastic solids. Many research groups have attempted to obtain a unified value or “universal quantity” but only resulting with different values or ranges derived from finite element simulations, mostly Vickers [63, 64, 68, 77, 78], conical [72, 79] from indentation hardness experiments [43, 80] and from theory [46]. The pioneer in defining this parameter was Tabor [43], defining it as the total strain imposed by the indenter. However, the numbers obtained for spherical and Vickers indenters have no apparent physical meaning, but a number to fit the experiments statistically [64] or, according to Tabor himself, an assumption that worked surprisingly well [81]. The only analytical study has been performed by Johnson [46] by using the contact mechanics theory and determining the indenter geometry dependency of the number, $\epsilon_r = 0.2c \cot \alpha$, where α is the indenter semi-apex angle. While numerous studies have focused their attention in obtaining the “magical” number constructing dimensionless functions, fitting endless curves and parameters, modeling virtual materials with different combinations of elasto-plastic properties, the physical foundations have been given less attention. Conversely, other methods have discovered

that the representative plastic strain may not be unique to all kinds of materials, instead, dependent on the tested material as it is the plastic strain field induced by sharp indenters. The materials respond according to their strain hardening behavior. The strain hardening exponent n , is a parameter that influences the strain field gradient under the sharp indenter, and therefore, the representative (average) plastic strain of that gradient zone will be particular to it.

One definition of representative plastic strain is the volume-averaged plastic strain within the plastic zone (resulting from indentation), defined as [64, 74]:

$$\epsilon_r = \frac{\sum \epsilon_i V_i}{V} \quad (2.6)$$

where ϵ_i is the equivalent plastic strain of an elemental volume V_i within the gradient plastic zone of total volume V . It was shown [74] that ϵ_r varies with the strain hardening exponent n , for one indenter geometry, but independent of σ_y and E (FIGURE 2.1).

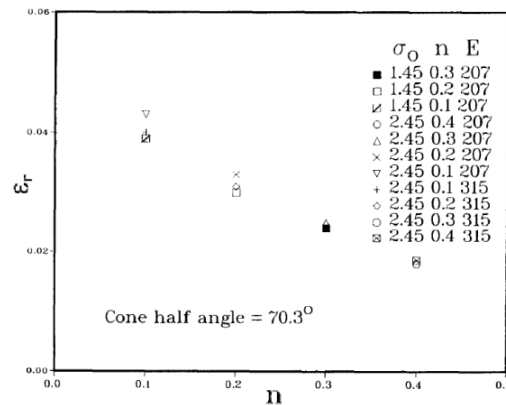


FIGURE 2.1: Volume-averaged plastic strain induced by conical indenter of half-angle of 70.3° showing dependency on the strain hardening exponent n , but not on yield strength or elastic modulus [74].

Recently, a study [82] was conducted to investigate the influence of the indenter angle of conical indenters on the gradient plastic zone beneath the indenter and on the representative plastic strain, defined as equation (2.6). Oxygen Free High Conductivity (OFHC) copper was the tested material. It was found that the representative plastic strain decreased with increasing indenter angle α .

In spite of the large variation in the magnitude of the representative strain, there is consensus among researchers that it is the key parameter in relating hardness to flow stress. TABLE 2.2 from reference [82] is a collection of some of the values of the representative plastic strain found so far by different researchers.

TABLE 2.2: Summary of representative plastic strain values obtained by different groups [82].

Researcher(s)	Indenter geometry	Type of study	Representative strain
Giannokopolus et al.	Vickers	Simulations	0.30
Johnson	Vickers	Theory	0.08 ($0.2 \cot \alpha$)
Chaudhri	Spherical ($d/D = 0.52$)	Experiments	0.20-0.25
Chaudhri	Vickers	Experiments	0.25-0.36
Tabor	Vickers	Experiments	0.08
Dao et al.	Vickers	Simulations	0.033
Chollacoop et al.	Conical indenters ($\alpha = 50, 60, 80^\circ$)	Simulations	$\epsilon_p(\alpha) = -2.185 \times 10^{-3}(\alpha) + 0.1894$
Ogasawara et al.	Vickers	Simulations	0.0115
Antunes et al.	Vickers	Simulations	0.034-0.042
Branch et al.	Vickers	Simulations	0.052 for $n = 0.064$ 0.035 for linear hardening material
Bucalille et al.	Conical indenters ($\alpha = 42.3^\circ, 50^\circ, 60^\circ$ and 70.3°)	Simulations	$\epsilon_p = 0.105 \cot \alpha$

A fully comprehensive definition of representative plastic strain is a matter of debate and under continuous investigation. Nevertheless, it is clear that it averages the strain field beneath the indenter, and serves to evaluate the increase in yield strength caused by plastic deformation during the indentation process. Likewise, it is a “characteristic” parameter of a material, i.e., affected by how the material responds mechanically to the indentation process manifested in the strain hardening exponent,

which is typical to each individual material; in other words, another material's property. Similarly, the constraint factor is dependent on the indenter geometry and material properties. FIGURE 2.2 from reference [83] shows the simulations of Berkovich and Vickers indentations on the same simulated material. It can be seen how the gradient strain fields form beneath the indenter and how they are a function of the geometry.

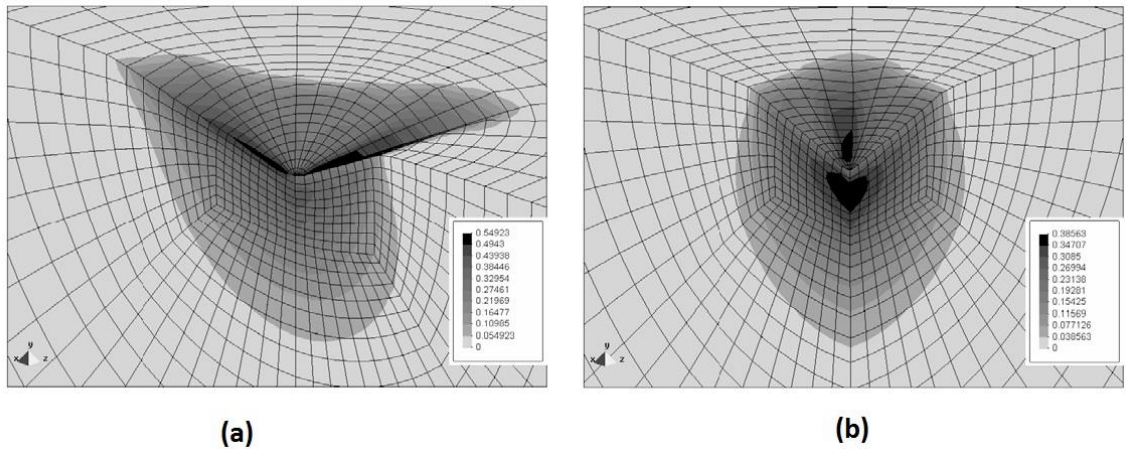


FIGURE 2.2: Strain gradient field under the indenter tip. Simulations of the indentation process on same material. (a) Berkovich. (b) Vickers [83].

2.4 Approaches of this Work

The relationship between the hardness of a material and its strength, manifested in the stress necessary to cause the material to flow plastically, was portrayed above. Departing from that relationship, the nanohardness obtained by instrumented indentation will be the means to determine the flow stress. Measurements along the axial direction in the post-test tensile specimen are performed. Therefore, nanohardness values for different cross sections, with a fixed value of plastic strain, can be matched to the flow stress for that particular plastic strain value. In other words, the degree of deformation at that specific cross section is such that if a tensile specimen was to be made out of the same

metal with that amount of initial plastic deformation, the flow stress will be higher than that of the annealed state. When the same hypothetical process was to be repeated, using another section of material with larger initial plastic deformation, the new flow stress would be at a higher level than the previous cross section. This trend is expected to continue until the very fracture cross section at the necked sections. Certainly, all those values of the flow stress should lie on the original path of the true stress-strain curve of the material tested continuously from its annealed state.

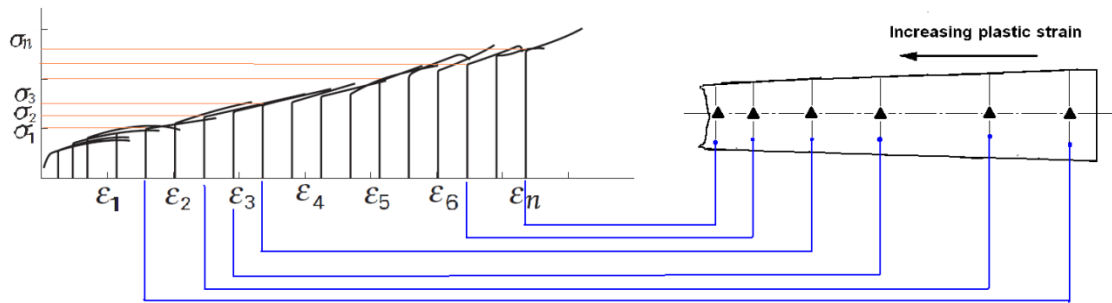


FIGURE 2.3: Schematic of the approach. For each of the cross sections, the amount of plastic deformation can be mapped into values of plastic strain in the true stress-strain diagram, which in turn will have a unique value of the flow stress.

FIGURE 2.3 depicts a schematic of the mapping of the measured true plastic strain into values on the true stress-strain curve; a unique set of points (ϵ_n, σ_n) can be utilized to trace the true stress-strain curve for each of the cross sections analyzed. In chapter 1 it was mentioned that the true stress-strain curve is constructed up to the maximum value of the force, which is the point where necking begins. Beyond that point the necking phenomena will cause a triaxial stress state and the curve will no longer represent a uniaxial stress state. To circumvent this issue, a reverse analysis is carried out by mapping nanohardness values into flow stress by means of the true plastic strain. In this

way, the nanohardness value measured at each cross section studied (represented by triangles in FIGURE 2.3) has a corresponding flow stress on the true stress-strain curve.

The assumption has its foundation on the theory introduced in section 2.2. Two of the materials studied in this research have power law strain hardening behavior (G018 and C11000), while the other has linear strain hardening behavior (S30400), thus, Tabor's relationship viewed in section 2.2 and summarized in the three scenarios in TABLE 2.1 is applied to the nanohardness measurements at each cross section performing a mapping $H \rightarrow \sigma_r$. Consequently, the constraint factor C , and the representative plastic strain ϵ_r , are derived from such mapping.

FIGURE 2.4 illustrates the same three cases presented in TABLE 2.1 where the hardness values are mapped into stress values using Tabor's relationship. This procedure is performed for each material studied in the present work.

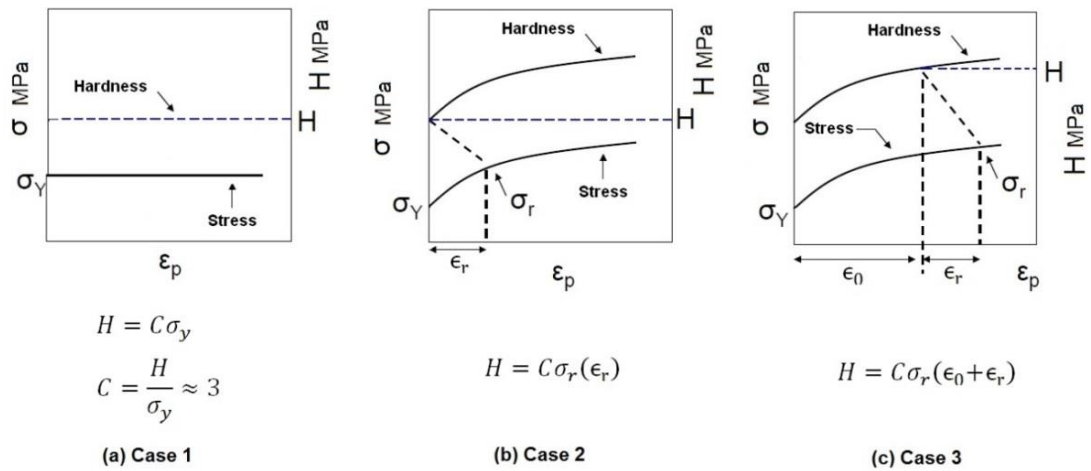


FIGURE 2.4: Tabor's relationship illustrated for the three different cases mentioned above: (a) perfectly plastic metal, with $C \approx 3$. (b) Indented annealed metal where the representative stress is a function of the representative strain. (c) Metal with initial plastic deformation before indentation; the representative stress is now a function of the initial plastic deformation ϵ_0 , plus the indentation representative plastic strain ϵ_r . Adapted from [84].

CHAPTER 3: MATERIALS AND EXPERIMENTAL PROCEDURES

3.1 Materials.

Tensile test samples (Laboratory Devices Company, Placerville, CA 95667) were machined out of three different materials: low carbon steel G10180 (AISI 1018), Electrolytic Tough Pitch copper (ETP) C11000 (ASTM B187), and austenitic stainless steel S30400 (AISI 304) [85]. In order to have the largest amount of plastic deformation, uniform and non-uniform, the as-received samples were subjected to full annealing treatment process; TABLE 3.1 summarizes the conditions of materials, compositions and heat treatments.

TABLE 3.1: Materials utilized in the research, designation, crystal structure and conditions followed to fully anneal them.

Material Designation (UNS)	Crystal Structure	Composition (%)	Annealing Conditions
Low carbon steel G10180	BCC	C: 15-20, Mn: 60-90, P 4(max), S: 5(max)	Kept at 870°C for 1 hour, then furnace cooled.
ETP Copper C11000	FCC	Cu: 99.90	Kept at 650°C for 1 hour, then water cooled.
Austenitic Stainless Steel S30400	FCC	C: 0.020, Cr: 18.270, Mn: 1.600, Ni: 8.440, P: 0.029, S: 0.025, Si: 0.392.	Kept at 1040°C for 1 hour, then water cooled.

3.2 Mechanical Testing.

In order to quantify the response of the studied materials to mechanical loading, different testing procedures were performed on two samples for each type of material. Quasi-static tensile test was carried out first, followed by nanoindentation experiments on samples taken out of the post-tensile test specimens. A simple metallographic study was conducted (only in G10180) to determine the change in grain size along the tensile direction and fractographs of the fracture cross-sectional area were taken to characterize the ductile behavior. Subsequently, compression tests were carried out to compare to the stress-strain properties found in tension experiments.

3.2.1 Tensile Test.

The cylindrical tensile test specimens were prepared according to the ASTM standard [14]; its geometrical configuration can be seen in FIGURE 3.1 with the nominal values specified.

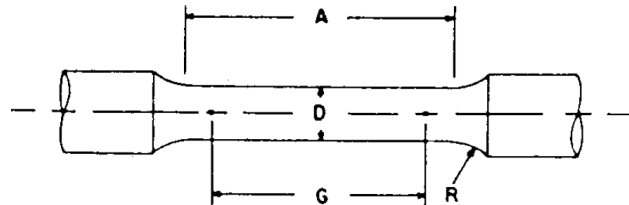


FIGURE 3.1: Cylindrical geometry Tensile Test Specimen [14]: $D=8.9$ mm, $G=36$ mm, $A=41.7$ mm (min), $R=6.35$ mm.

The dimension G in FIGURE 3.1 represents the gage length taken as the distance between two white marks drawn approximately 36 mm away from each other. All the samples were tested on an Instron® 5582 Universal Testing Machine with a non-contact (video) extensometer coupled to it. The tests were conducted by pulling the specimen at a

constant load cell speed of 2.5 mm/min, value within the range specified by the ASTM Standard, while continuously the non-contact extensometer was measuring the increments in the gage length until fracture ended the test. For each of the samples tested, the final dimensions, i.e., the length or distance between the marks, and the final diameter at the neck cross section were recorded. It is worth mentioning that the nominal strain rates for all tests were kept within the quasi-static interval; between 10^{-4} to 10^{-3} 1/s.

3.2.2 Instrumented Nanoindentation and Microhardness.

With the purpose of preparing a suitable type of sample to be tested by Instrumented Nanoindentation, a customized cut was designed; such cut consisted of slicing one of the broken halves through its longitudinal axis (mid-section) for each of the material specimens. The technique used was wire cut Electrical Discharge Machining (EDM) at Monroe Custom Molds, Inc. (Monroe, NC). The thickness of the thin slice was 0.5 mm spanning from the fracture tip going into the material up to the start point of the gage length. A schematic of this cut is illustrated in FIGURE 3.2.

The samples for Instrumented Nanoindentation were prepared following the sample preparation procedure described below; the purpose was to have a surface suitable for testing in terms of roughness and flatness, in a manner that the data will not be considerably affected by this factor.

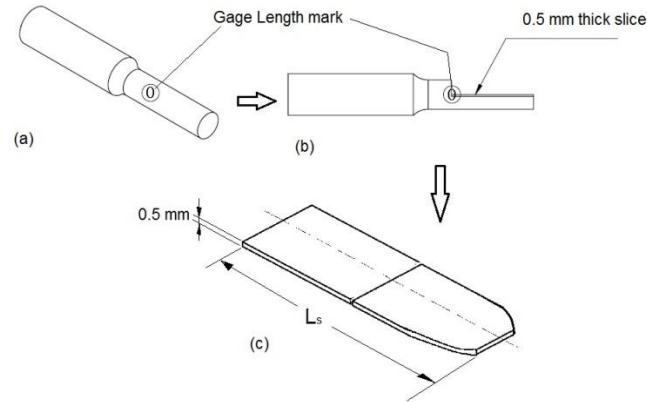


FIGURE 3.2: Schematic illustration showing how the sample for Instrumented Nanoindentation was obtained. (a) Post-tensile test specimen half. (b) Cutting along axial plane to extract a 5 mm slice. (c). Sample for Instrumented Nanoindentation, where L_s is the length of the sample along nanoindentation measurements were taken.

The instrumented Nanoindentation testing was conducted on the MTS® Nanoindenter G200 (now Agilent Technologies®) utilizing the XP head with a Berkovich (three sided pyramid) tip mounted. The method followed was the G-Series CSM [86] Standard Hardness, Modulus, and Tip Cal; this method allows the user to have control on the displacement into surface, which was set to 2000 nm ($2\mu\text{m}$) for all experiments with the purpose of eliminating the ISE described earlier in section 1.7.2. The Poisson's ratio input values for the Nanoindentation testing were 0.28, 0.33 and 0.29 for G10180, C11000 and S30400 respectively.

The Nanoindentation samples were divided in half as shown in FIGURE 3.2(c), and imaginary lines perpendicular to the tensile axis direction were drawn from left to right (the leftmost point being the gage length mark, and the rightmost one the fracture tip section) every 3 mm, then 1 mm and 0.5 mm spacing as the necking region approaches. On each of those lines, 12 equally spaced indentations sites were chosen in the diametral

direction at which at least 6 indentations were made. FIGURE 3.3 depicts the indentation sites on one of the G10180 samples.

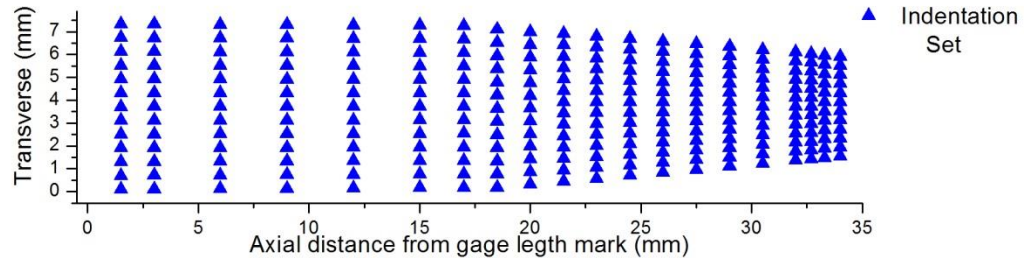


FIGURE 3.3: Map of the nanoindentation sites for the G10180. Transverse or diametral direction, and axial distance from gage length mark, L_s .

Microhardness testing was performed on the same samples intercalating the test sites with those from the nanoindentation, i.e., along the same vertical lines, in the gaps between the 12 equally spaced nanoindentation sites. The load was set to 200 gf, and the indenter was the common four-sided pyramid Vickers indenter.

3.2.3 Compression Test.

Cylindrical compression samples were machined down from the grip-sections of the post-test tensile specimens. The height and diameter were kept close to 9 mm and 6 mm respectively so as to maintain the height to diameter ratio around 1.5. The tests were performed accordingly to the ASTM Standard [87]. The load cell speed was set to produce the same nominal strain rate value of that of the tensile test, utilizing the Instron® 5582 Universal Testing Machine, but this time the non-contact (video) extensometer was disabled. Since the change in height is being measured by the instantaneous distance between the platens, a correction for the machine compliance has to be applied to the outcome data to take into account the elastic deflections of the

components and/or machine frame [88]. In order to minimize the bulging of the samples, both ends of the cylindrical samples were grinded and polished following the samples preparation process outlined below; additionally, a layer of grease was laid on the top and bottom surfaces and on both platens to reduce the friction as much as possible. None of the samples were taken to failure, but only to the strain level where the bulging effect was not evident, i.e., around $\epsilon \approx 0.5$.

3.2.4 Nanoindentation Strain Rate Sensitivity.

The indentation strain rate sensitivity was probed with the aid of the MTS® Nanoindenter G200 (now Agilent Technologies®) utilizing the XP head fitted with a Berkovich tip. The method applied in the current case was the G-Series XP CSM Strain-Rate Sensitivity, that is based on Nanoindentation strain-rate jump test developed by Maier et al [89]. Imaginary lines in the diametral direction were followed performing the test at 4 different applied indentation strain rates (0.001, 0.004, 0.014 and 0.05 1/s) in 16 sites. Those lines were located at the necking in order to identify some change in the strain rate response with the increasing amount of plastic deformation present at cross sections closer to the neck tip.

3.3 Preparation of the Surface of Samples.

All the surfaces to be tested by Nanoindentation technique, both ends of the compression cylinders specimens and the axial plane of the samples from the grip section of post-test tensile specimens were prepared to create a mirror like finish. The first stage consisted of hand grinding with silicon carbide sandpaper of progressively finer particle sizes, i.e., 320, 400, 600, 800, and 1200 numbers. Only in the case of samples subjected to nanoindentation testing, very fine grinding with 3M™ Diamond Lapping Discs, NH,

and Type 661 X was performed up to 0.5 μm particle size. Finally, polishing with a microcloth on a ECOMET® 3 polisher wheel using alumina, Al_2O_3 , of 0.3 μm and 0.05 μm particle size in water suspension.

3.4 Optical and Scanning Electron Microscopy.

After obtaining a mirror finish on the samples surfaces, they were etched accordingly to ASTM Standard E407 [90], in order to reveal the microstructure of the samples. The grain size was measured at different locations along L_s to observe its variation with position and, therefore, with amount of plastic deformation; also, how the grain shape changed in the axial direction was studied (G10180 steel only). For each material the proper etchant was prepared and the samples were immerse/swab for the time needed to reveal the grain characteristics; caution measurements and proper procedures were followed at the time of manipulating the reagent components [91, 92].

TABLE 3.2: Reagents, their components and procedure followed during the etching process of the samples. Etchant number* according to ASTM Standard [90].

Material	Etchant number* and name	Etchant components	Procedure
G10180	74 (Nital)	98 mL methanol, 2 mL HNO_3	Samples immersed for 5 – 15 seconds.
C11000	30	25 mL NH_4OH , 25 mL water, 30 mL H_2O_2	Samples immersed for 10 seconds
S30400	12 (Aqua Regia)	15 mL HCl , 5mL HNO_3 .	Samples immersed for 25 seconds

Observation of the samples was done on the optical Microscope Olympus® BX51 coupled with a ColorView Soft Imaging system; the images were recorded at magnifications from 10X to 100X.

In regard to fractographs of the cup-cone fracture, a JEOL® JSM-6480 Scanning Electron Microscope (SEM) was utilized for that purpose. The qualitative characteristics of the fracture surface were analyzed. The SEM technique served as a method to observe the indentation sites and to detect the piling-up or sinking-in behavior at a specific location. Also such technique shed light on how the topography of the sample at the neck may be influencing the final results.

CHAPTER 4: RESULTS AND DISCUSSION

4.1 Stress-Strain Curves.

The engineering (nominal) stress-strain curves for G10180, S30400 and C11000 are plotted in FIGURE 4.1 Two curves are shown for each material; both of them are very close to each other indicating that the conditions for the test were consistent for both, and the specimen's material behave in similar manner. From this point only one curve will be shown for each material for the sake of clarity.

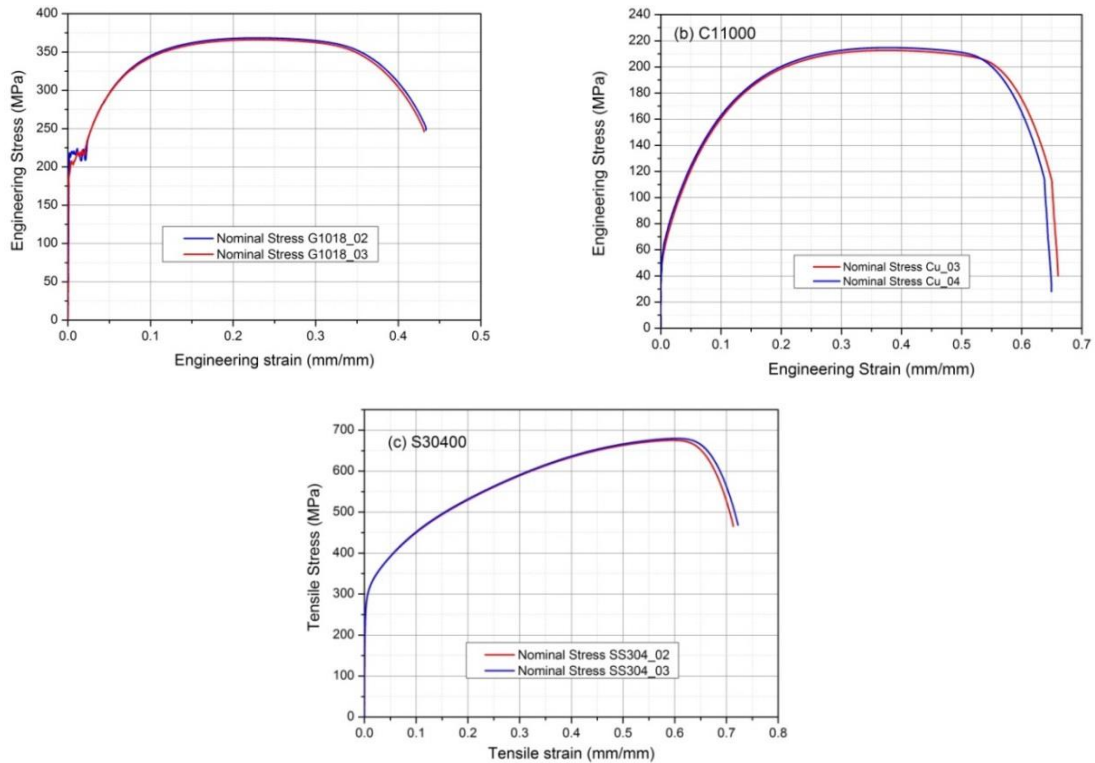


FIGURE 4.1: Nominal stress-strain curves from uniaxial tensile tests carried out on (a) G10180, (b) C11000 and (c) S30400. Results from two specimens are displayed.

The experimental and literature values of the elasto-plastic properties for the three materials extracted from the curves in FIGURE 4.1 are summarized in TABLE 4.1. It is noteworthy the large value of the %*EL* and %*AR* for the three materials.

TABLE 4.1: Elasto-plastic properties from engineering stress-strain curves of G10180, C11000 and S30400.

Property	G10180		C11000		S30400	
	Experiment	Literature	Experiment	Literature	Experiment	Literature
σ_y (MPa)	223	236	53	69	275	290
<i>UTS</i> (MPa)	368	354	213	220	679	621
<i>E</i> (GPa)	200	205	112	115	193	193
% <i>EL</i>	45	25 (in 50 mm)	66	55 (in 50 mm)	72	55 (in 50 mm)
% <i>AR</i>	43	50	85	-----	74	50

The features of pre-test and post-test G10180 steel specimens are shown in FIGURE 4.2. In addition to the evident deformation at the neck region, it is worth mentioning that the diameter of the reduced section decreased gradually throughout its entire length, being more severe, as expected, at the narrowest cross section right at the neck. This fact aids the characterization of a unique value of plastic strain for different cross sections considered in the research of this dissertation.

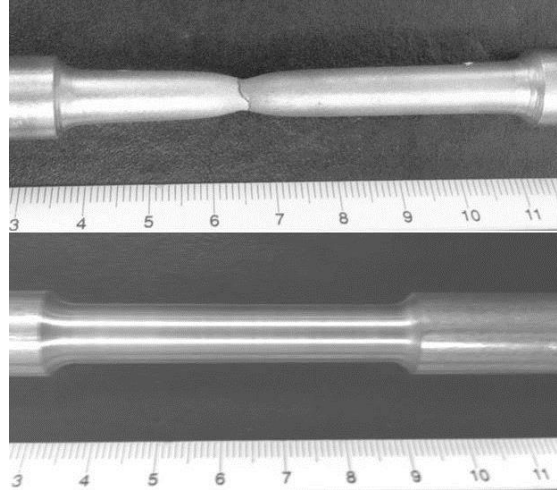


FIGURE 4.2: Before (bottom) and after (top) G10180 tensile specimens showing the necking feature and the decrease in diameter along the whole reduced section.

The true curves were obtained by means of equation (1.11) and (1.12). As it was pointed out in chapter 1, the curve can only be drawn for the homogeneous plastic deformation range, i.e., right before plastic instability begins at ϵ_{Tu} (according to Considère criterion). Thus the curve is interrupted at the point that corresponds to the maximum load (UTS value in the nominal curve). By means of equation (1.13) the true plastic strain was calculated using the post-test specimen dimensions. FIGURE 4.3 shows the true curves of the same materials in FIGURE 4.1 along with the ones obtained in the compression tests. The isolated point at the upper right corner of each figure corresponds to true fracture stress and strain data without any correction applied to it. The right hand side of FIGURE 4.3 illustrates the strain hardening behavior of each metal. G10180 steel and C11000 copper display power law strain hardening behavior evidenced by a suitable linear fit on a log-log scale. The Hollomon equations that describe the segment between the yield stress and the load maximum point for G10180 steel and C11000 copper are $\sigma_T = 707.02\epsilon_{Tp}^{0.27} \text{ MPa}$ and $\sigma_T = 497.55\epsilon_{Tp}^{0.44} \text{ MPa}$, respectively.

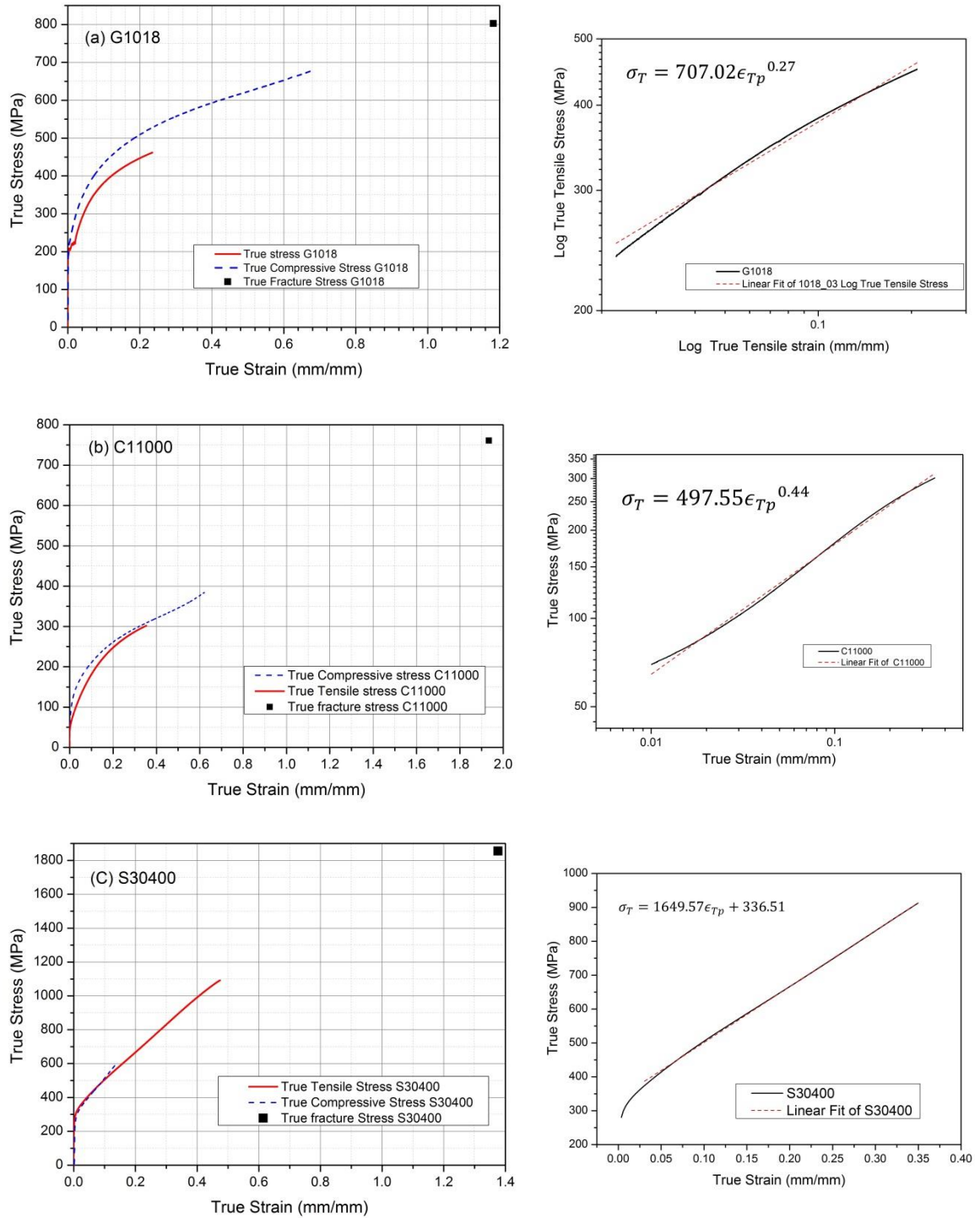


FIGURE 4.3: True stress-strain curves from tensile and compression tests, and fracture points for (a) G10180 steel, (b) C11000 and (c) S30400. The plot on the right of each curve shows the strain hardening behavior of each.

The results for C11000 are comparable to reported values from literature [80, 82], the value of K and n for copper was $K = 491$ and $n = 0.46$, and $K = 405$ and $n = 0.46$ respectively, even though they studied C10100 OFHC (Oxygen Free High Conductivity) copper.

The scenario for S30400 stainless steel in terms of strain hardening behavior differs from G10180 and C11000. A linear strain hardening law ($n = 1$) is followed, and the linear fit is $\sigma_T = 1649.57\epsilon_{Tp} + 336.5 \text{ MPa}$.

In FIGURE 4.3, the true curve from compression test is in close agreement with that from tensile test except in G10180 steel; it is argued that the yield phenomenon present in low carbon steels only under tensile load causes the observed discrepancy in the two curves. In the case of C11000 copper, the compression curve shows some signs of bulging or barreling effect in the last portion of the curve; the elastic part of the compressive curve reproduces well that from tensile test.

The true uniform strain right before the onset of necking, ϵ_{Tu} , for G10180 steel and C11000 copper is close to that predicted by (1.25), which estimates its value to be equal to the strain hardening exponent; 0.27 for G10180 and 0.44 for C11000; in both cases the onset of necking begins at a lower value of the strain than the predicted one, 0.22 and 0.35 respectively. There is a big gap in the true curves between ϵ_{Tu} and ϵ_{Tf} , showing a big difference in the plastic strains at the onset of necking and at the fracture point. Such a gap is indicative of the large amount of plastic deformation that has been taken place during the necking phenomenon, and therefore, the large margin of error when dealing with correction methods for the nonuniform plastic strains.

4.2 Indentation Hardness Profile.

Results from indentation hardness measurements along axial direction of the sliced specimens are shown in FIGURE 4.4. Blue colored triangles and red colored rhombuses represent Berkovich (nanoindentation) and Vickers (microhardness) respectively.

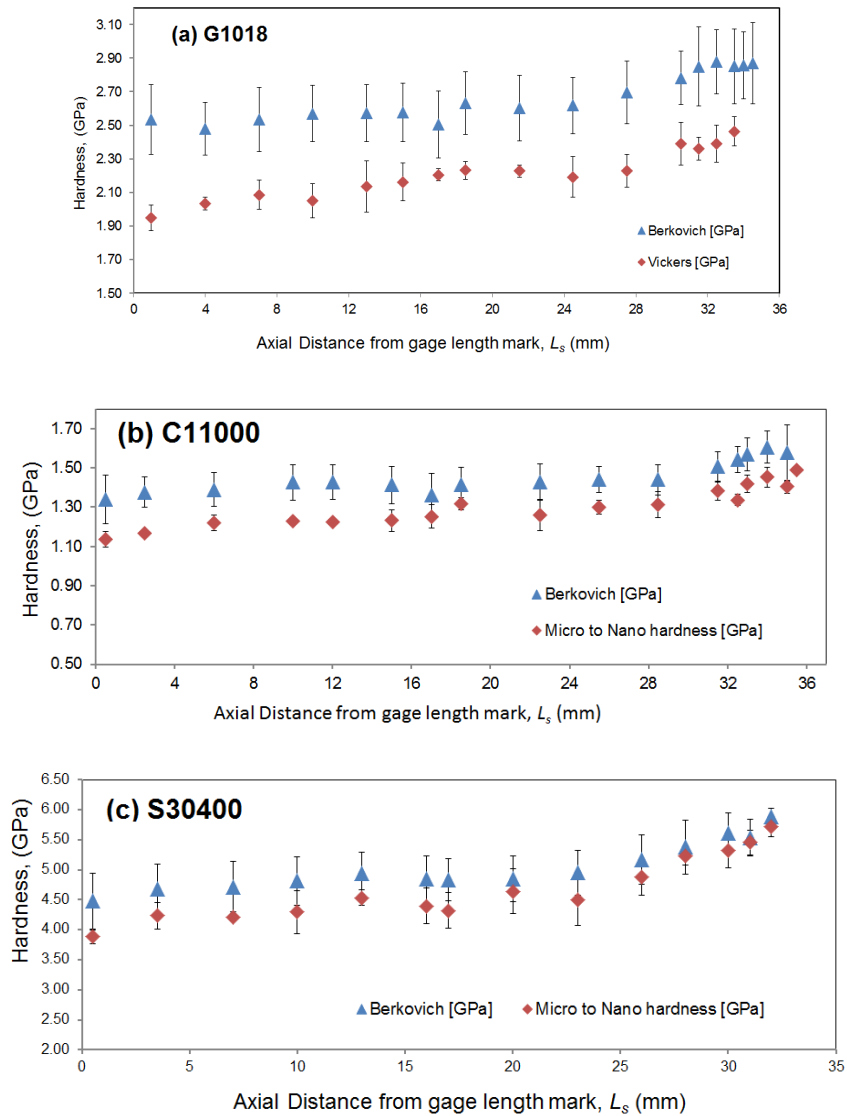


FIGURE 4.4: Variation of hardness with distance from gage length mark, L_s . Berkovich (blue) and Vickers (red) measurements.

Both types of hardness show an increasing trend starting with the lowest value at the section where the gage length mark is located and the highest at the neck section. A more detailed examination of the plots in FIGURE 4.4 reveals that both types of hardness measurements differ in certain amount, even though both follow the same trend. It is worth highlighting that both are plotted in the same scale (GPa), but one of them has to be converted into the other. In other words, both are not directly comparable numbers. Vickers hardness is based on the measurement of the actual area of the residual indent left by the pyramidal indenter on the material, and Berkovich hardness (nanohardness) is founded on the concept of the projected contact area at maximum load. The differences between them are twofold: the first relies on the concept of the area itself that is used to calculate their values, and the second is a more obvious one and is intrinsic to the geometrical configuration of the indenter and of the impression as well. In order to convert Vickers hardness numbers HV [93], to equivalent projected Vickers numbers HV_{proj} , the following expression is used

$$HV_{proj}(GPa) = 1.0577 \times 10^{-2} HV \quad (4.1)$$

The values in FIGURE 4.4 were converted using equation (4.1). The geometrical issue is circumvented by modeling the Berkovich with a conical indenter with a half-included angle, $\phi = 70.3^\circ$. Also, the error bars become larger for those sections closer to the neck indicating wider variation of the hardness values

4.3 Indentation Hardness Map.

Nanoindentation hardness measurements were made at selected locations shown in FIGURE 3.3 for the three materials. The nanohardness values obtained are mapped

over the entire area of the samples. FIGURE 4.5 depicts nanohardness maps (left) with their color codes (right).

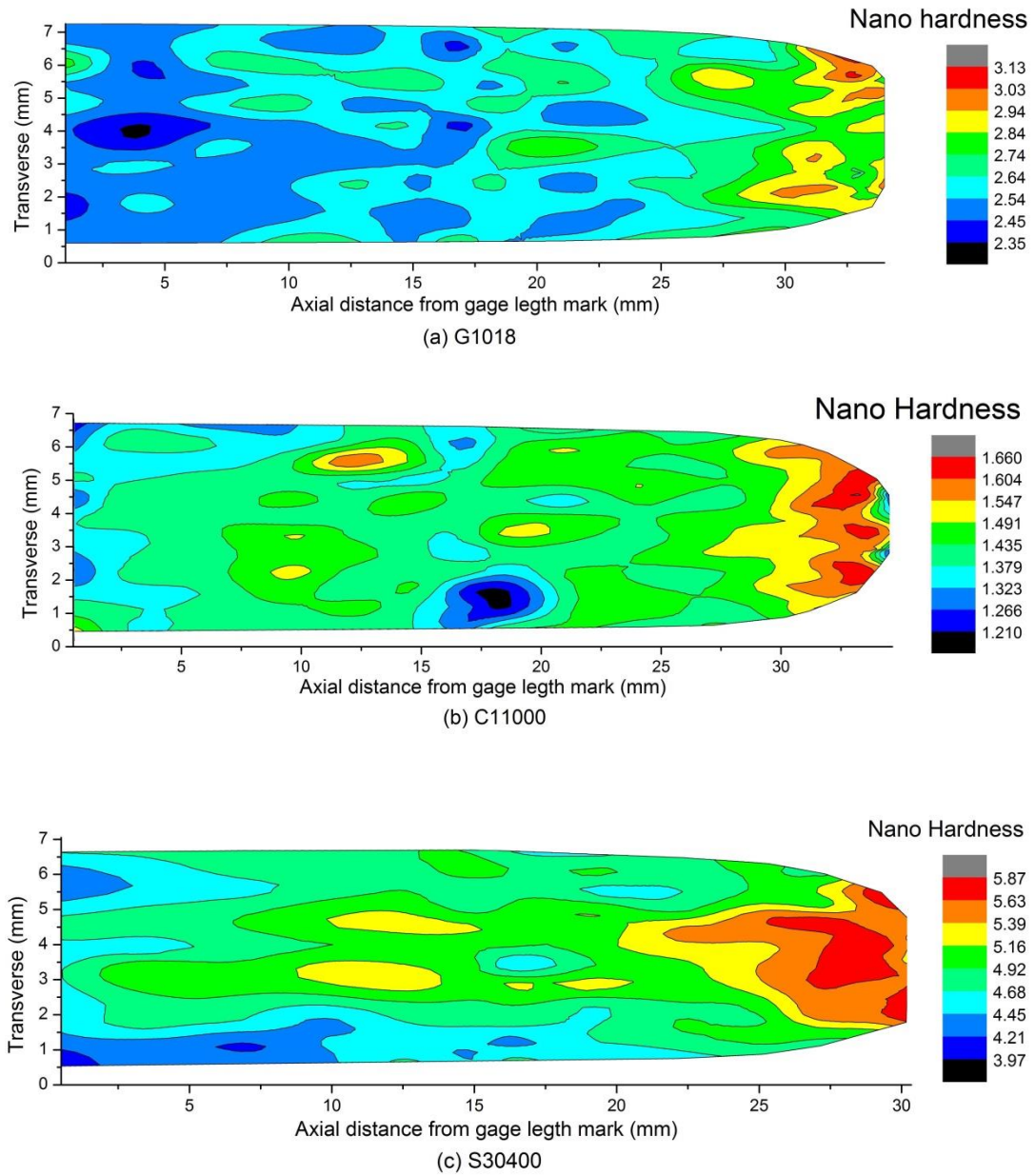


FIGURE 4.5: Hardness maps of: (a) G10180 steel. (b) C11000 copper. (c) S30400 stainless steel.

While data shown in FIGURE 4.4 represents averages along the transverse (diametral) direction, the nanohardness map in FIGURE 4.5 indicates the actual range value at every location of the sample surface. As logic would dictate, it may have been anticipated that higher nanohardness numbers will have resulted at the necked sections. However, the maps show that values of medium range nanohardness values (yellow and green) were present too at the narrowest section in the three materials. This is more evident in G10180 steel and in less proportion in C11000 copper and much less in S30400. This fact explains why the error bars in FIGURE 4.4 become larger at sections in the neck region, especially in G10180. Generally, the values of hardness along the main (longitudinal) axis tend to be higher than those ones above and below it. The highest nanohardness values (red color) occur about the mid-section close to the end of the specimen, but not at the very tip. This indicates that the localized strain hardening during necking is more severe at the core of the neck for the two FCC metals, C11000 and S30400) and more towards the exterior for the G10180 steel that has BCC structure.

4.4 Mapping Indentation Hardness into Flow Stress.

The relationship between hardness and flow stress is established through the measured plastic strain on the sample. True plastic strain measurements of the same diametral sections designated for hardness measurements (see FIGURE 3.3) were performed. Each average value of nanohardness, shown in FIGURE 4.4, can be associated with a unique value of the plastic strain measured on the specimen. The method of converting hardness into equivalent plastic strain has been used in the past by some researches [82, 94]. They converted micro hardness values taken inside a strain gradient field left by a macro Vickers indent into equivalent plastic strain. In the research

of this dissertation, the average values of nano hardness are plotted against the post-test plastic strain. The trend of nano hardness vs. true plastic strain turns out to follow closely a power law relationship, thus, a log-log plot might describe well such behavior, and therefore, a linear fit on that plot is suitable to be applied. TABLE 4.2 compiles the power law relationships and FIGURE 4.6 plots nano hardness values vs. true plastic strain in a log-log scale along with their linear fit.

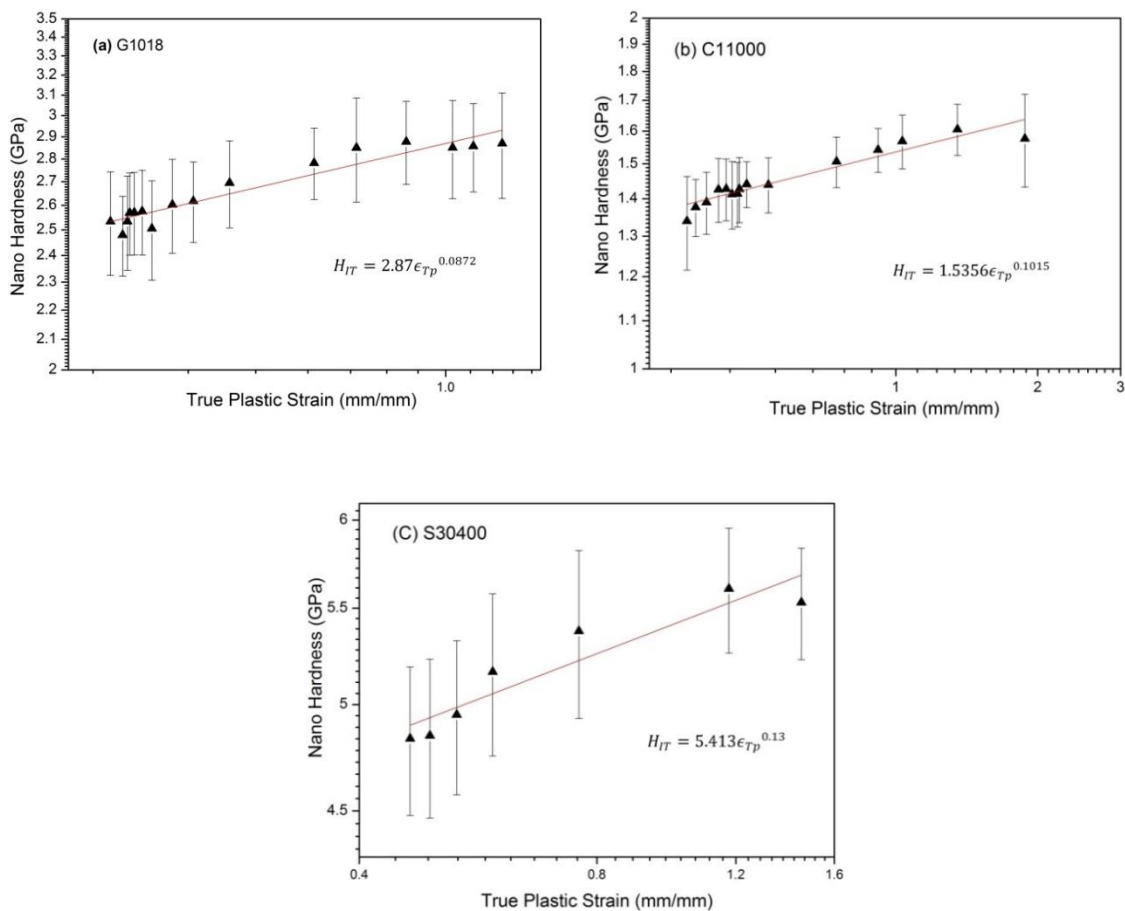


FIGURE 4.6: Log-Log plot of nano Hardness vs. True plastic strain. The power law equation links nano hardness with true plastic strain. (a) G10180 steel, (b) C11000 copper and (c) S30400 stainless steel. The red line is the linear fit at the given scale.

It is worth mentioning that the value of the true plastic strain measurements on G10180 steel and C11000 copper are higher than their respective plastic strains at the

onset of necking ϵ_{Tu} . Contrary to that fact, for the S30400 case, plastic strain values lower than its ϵ_{Tu} were measured; i.e., when $L_s = 0$ (leftmost end of the sample) the value of the plastic strain was $0.39 < 0.47$ (its necking strain). Consequently, most of the plastic deformation is more localized and closer to the fracture, at the neck region, than the other two materials. The fourth column in TABLE 4.2 displays the range of plastic strain for the power law expression found for each material.

TABLE 4.2: Strain hardening and nanohardness expressions as functions of the true plastic strain interval specified.

Material	ϵ_{Tp}	$\sigma_T(\epsilon_{Tp})$ in MPa	Interval	$H_{IT}(\epsilon_{Tp})$ in MPa
	Interval	Hollomon		
G10180	<0.23	$\sigma_T = 707.02\epsilon_{Tp}^{0.27}$ (4.2)	0.23-1.18	$H_{IT} = 2870\epsilon_{Tp}^{0.0872}$ (4.3)
C11000	<0.35	$\sigma_T = 497.55\epsilon_{Tp}^{0.44}$ (4.4)	0.35-1.9	$H_{IT} = 1535.6\epsilon_{Tp}^{0.1015}$ (4.5)
S30400	<0.47	$\sigma_T = 1649.57\epsilon_{Tp} + 336.5$ (4.6)	0.47-1.43	$H_{IT} = 5413\epsilon_{Tp}^{0.13}$ (4.7)

The hardness can be transformed into plastic strain by means of the expressions (4.3), (4.5) and (4.7). The plastic strain contours are shown in FIGURE 4.7; they all three display approximately symmetric contours at the neck region. S30400 stainless steel exhibits a more uniform distribution of the strain throughout the entire sample whilst in C11000 copper is more localized at the neck. This behavior is corroborated by contrasting the %EL and %RA; a more strained mid-section in S30400, high %EL, and more strained neck-section, high %RA, for C11000. In other words, S30400 has the ability to take plastic deformation in a more uniform manner than C11000. G10180 is the

material that shows more tendency to accommodate most of plastic deformation at the neck.

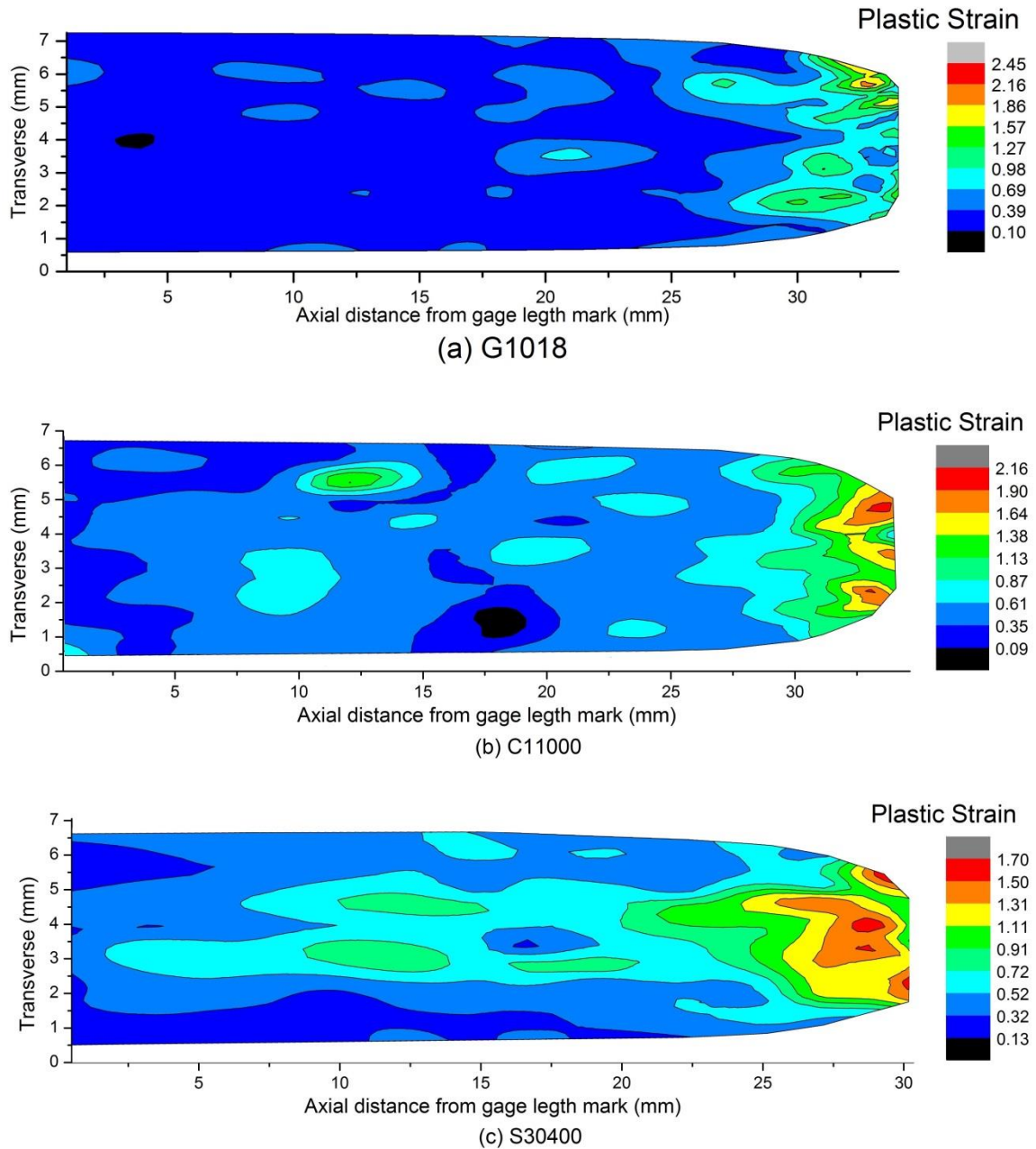


FIGURE 4.7: Plastic strain contours obtained from nanohardness measurements for (a) G10180 steel, (b) C11000 copper and (c) S30400 stainless steel.

4.5 Reverse Analysis.

The reverse analysis can be performed on the basis of the relationship found between indentation hardness and plastic strain discussed in chapter 2. Thus, flow stress given by the Hollomon equation (1.21) is valid up to ϵ_{Tu} ; from that point on, the plastic strain range valid for equations (4.3), (4.5) and (4.7) begins. For instance, G10180 has a fitted power law equation of $\sigma_T = 707.02\epsilon_{Tp}^{0.27}$ which is valid between ϵ_{yield} and ϵ_{Tu} ; afterwards, values for the flow stress are uncertain from the tensile test, but nanohardness data is available from the nanohardness map, FIGURE 4.5(a) for values up to the fracture plastic strain ϵ_{Tf} . FIGURE 4.8 is a schematic that clarifies this relationship.



FIGURE 4.8: Schematic of the reverse analysis performed. Plastic strain ranges for measured nanohardness (left) and flow curve (right).

The data from FIGURE 4.6(a) is well described by power law equation $H_{IT} = 2.87\epsilon_{Tp}^{0.0882}$, and then both equations (4.2) and (4.3), will have values linked to a common value of the plastic strain; i.e., at ϵ_{Tu} . Or, to state it in another way, the constraint factor C , can be found at that specific value of plastic strain since both, indentation hardness and flow (representative) stress are known; the following expression summarizes such relationship as:

$$C = \frac{H_{IT}}{\sigma_T} \Big|_{\epsilon_{Tu}} \quad (4.8)$$

The constraint factor that relates nanoindentation hardness and flow stress in G10180 is $C \approx 5.5$, which means that nanohardness values are C times larger than the flow stress (using same units for both quantities). Subsequently, flow stress values are obtained by dividing equation (4.3) by the constraint factor such that the fitted power law equation from nanohardness results is transformed into

$$\sigma_T = 527.17\epsilon_{Tp}^{0.0882} \quad (4.9)$$

Equation (4.9) is the expression to describe the post-necking behavior of G10180 steel. Similar calculations can be made for C11000, equations (4.4) and (4.5), and for S30400, equations (4.6) and (4.7), evaluating them at the true plastic strain value of ϵ_{Tu} , common to both intervals. Subsequently, the constraint factor for each material is found by means of the expression (4.8); TABLE 4.3 is a summary of the result of such calculations. The flow stress converted from nanohardness for C11000 is

$$\sigma_T = 341.24\epsilon_{Tp}^{0.102} \quad (4.10)$$

and for S30400 is

$$\sigma_T = 1202.88\epsilon_{Tp}^{0.13} \quad (4.11)$$

both expressions give the value in MPa. The power law exponents in equations (4.9) to (4.11) differ from those in Hollomon equations due to the change in the strain hardening with large plastic strains (see TABLE 4.2). In reference [82], it is stated that the differences in the exponents of the power law functions are due to the intrinsic nature of two types of testing methods, additionally, the plastic strain is homogeneous in compression but not during indentation. In the study of this dissertation, the plastic strains involved are inhomogeneous; i.e., the nonuniform strain during tensile and the

strain field left by an indentation. It is argued that both power law exponents have to be different. The strain hardening behavior that governs before the onset of necking cannot continue up to the fracture because, when necking begins, another mechanism comes into play. The expressions for the true (flow) stress found in the analysis are referred only to uniaxial stress.

TABLE 4.3: Constraint Factor C , obtained from nanoindentation hardness.

Material	Constraint Factor (from nanoindentation)
G10180	5.5
C11000	4.5
S30400	4.5

Recalling that the original concept of the constraint factor was to relate hardness to a representative value of the stress in an undeformed material, case 2 in FIGURE 2.4, the representative plastic strain can be found applying Tabor's relationship. The nanohardness of the material in the annealed condition was measured, and with the known constraint factor value, the calculation is straightforward. The G10180 steel annealed has a nanohardness value of 1.23 GPa (1230 MPa) which leads to a value of the representative stress for the undeformed material of 265.38 MPa ; the value of the representative plastic strain for G10180 steel is found by looking at the true stress-strain diagram and reading directly the value for ϵ_r . FIGURE 4.9 shows how to obtain the total strain from the representative stress; the representative stress and its related true strain (total).

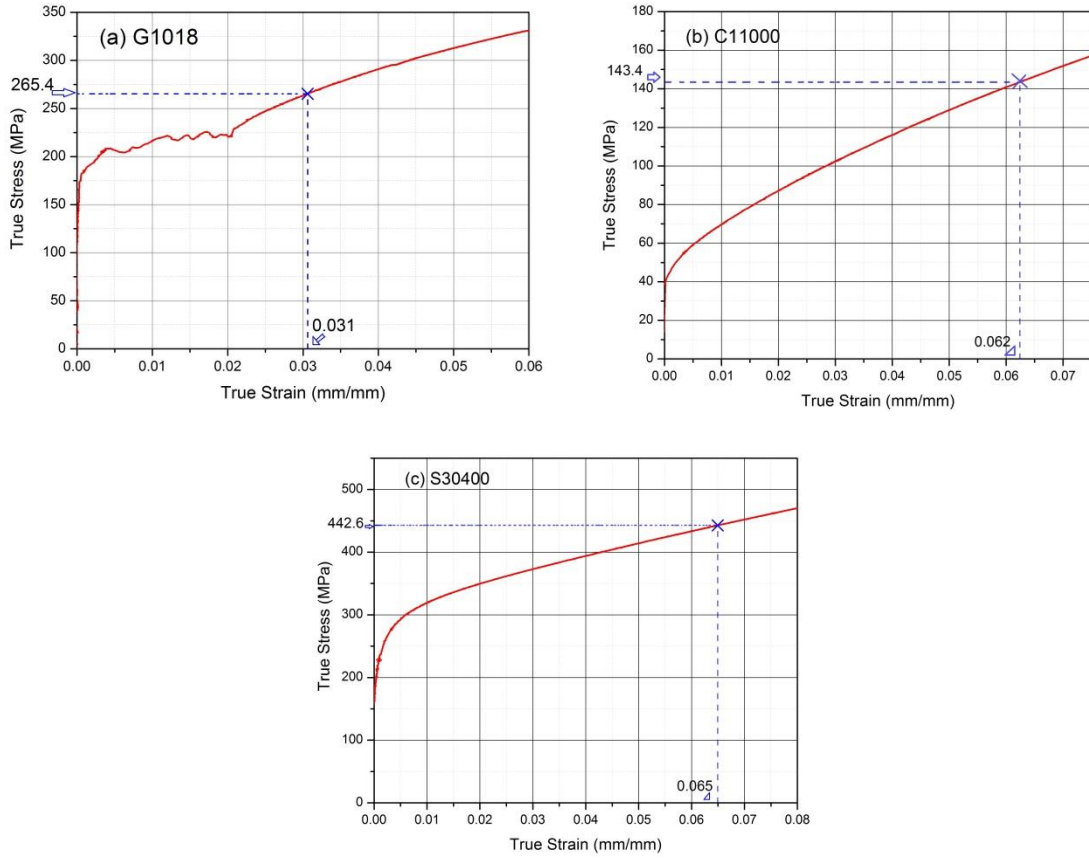


FIGURE 4.9: Representative stress for G10180 steel, $\sigma_r = 265.38 \text{ MPa}$, used as input to find out the representative plastic strain. The total strain for this stress level is $\epsilon_{Total} = 0.031$. Similar method to find those for C11000 and S30400.

The mathematical definition for the representative plastic strain, given in the literature [63, 78, 95], for a power law strain hardening material such as G10180 steel is

$$\epsilon_r \equiv \epsilon_{total} - \epsilon_y = \epsilon_{total} - \frac{\sigma_y}{E}$$

where $\epsilon_y = \sigma_y/E$ is the yield strain. In the particular case of the G10180 steel studied in the research of this dissertation, $\epsilon_{total} = 0.031$, and $\epsilon_y = 0.003$, therefore $\epsilon_r = 0.028$.

Likewise, the value of the representative stress for the annealed material, and consequently, the representative plastic strain ϵ_r can be obtained for C11000 and S30400.

TABLE 4.4 summarizes the experimental results for the three materials with their

respective representative plastic strain. The constraint factors used are those from TABLE 4.3.

TABLE 4.4: Representative stress and Representative plastic strain values for G10180, C11000 and S30400.

Material	Nanohardness of the annealed material (GPa)	Representative stress, σ_r (MPa)	Representative plastic strain, ϵ_r (mm/mm)
G10180	1.23	265.38	0.028
C11000	0.65	143.42	0.062
S30400	1.99	442.62	0.061

It is necessary to clarify that the values of representative plastic strain and of the constraint factors are determined based on the nanoindentation results. No similar study has to date been performed by any research group. In contrast, abundantly of them regarding Vickers indentation analyses are well known in the literature. The two FCC materials display closer values in their representative plastic strains, while the BCC one differs significantly. Whether or not the crystal structure affects the representative plastic strain, additional experiments and simulations have to be performed before drawing such a conclusion.

4.6 Corrected True Stress-Strain Data.

The complete true stress-strain data up to the fracture point for the three materials studied in the research of this dissertation are displayed in FIGURE 4.10. The solid red lines correspond to the true curves in the uniform plastic deformation range (pre-necking), the blue dashed lines are expressions (4.9) to (4.11) plotted for the nonuniform plastic deformation (post-necking), and the triangles represent the experimental nanohardness values divided by the constrain factor.

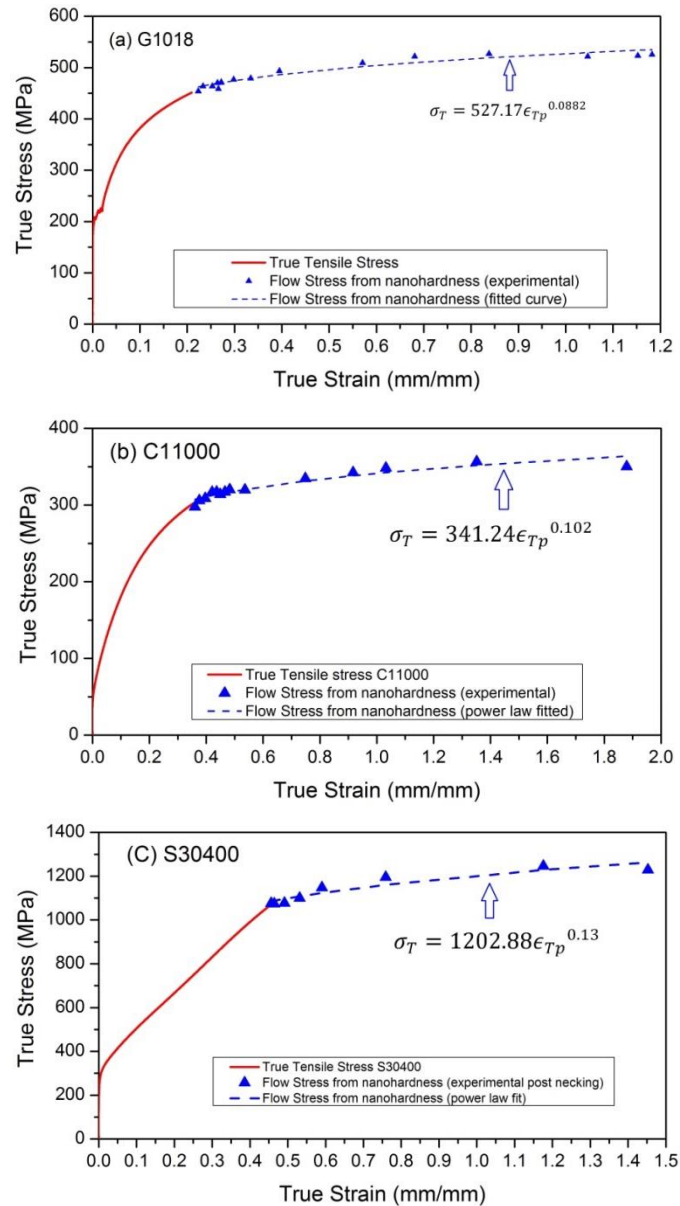


FIGURE 4.10: Corrected True Stress-Strain curves for (a) G10180 steel, (b) C11000 Copper and (c) S30400 Stainless steel.

A feature that is shared by the three materials is the mild decrease in the value of the flow stress derived from nanohardness. This fact was evidenced in the hardness maps (FIGURE 4.5) where lower values of hardness were measured at the very fracture tip. A possible explanation is that the microvoid coalescence (MVC) phenomenon [96-99], present in all this three ductile fractures, is responsible for leaving voids or material

“empty” spaces in a great number such that the strained material under the indenter lacks of constraint. Therefore, the displacement into surface would be larger than if the defects were not present. Also, the size of the indenter tip is comparable with that of the voids.

It is evident that there is a well-defined transition in the strain hardening behavior of the materials. It is markedly strong in the uniform strain portion of the curve and very slight in the nonuniform one where it is mostly localized at the neck. The post-necking strain hardening power law expressions account for the effect of necking on the uniaxial (longitudinal) true stress only.

4.7 Validity of the Method.

Earlier in this chapter, it was mentioned that the plastic strain range measured on S304000 was $\langle 0.39, 1.43 \rangle$, but since this research is focused on post-necking data, only the plastic strain range $\langle 0.47, 1.43 \rangle$ was used in the power law expression defined in equation (4.7). Nevertheless, the remaining part of the plastic strain interval $\langle 0.39, 0.47 \rangle$ with their associated nanohardness values was plotted in FIGURE 4.11. It can be seen that a linear fit (dashed red line) is the closest approximation to describe the behavior of the nanohardness within that interval. Such linear behavior is in agreement with the linear strain hardening behavior of the material within the uniform plastic deformation regime.

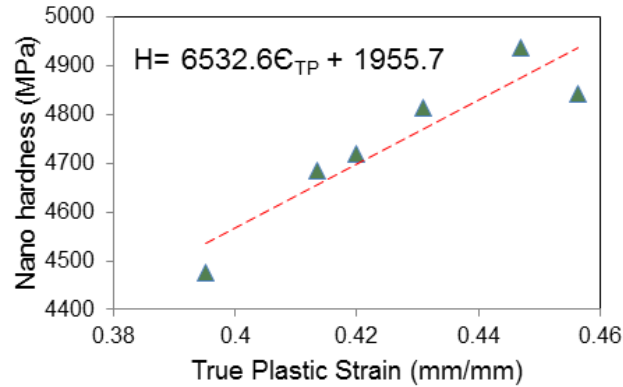


FIGURE 4.11: Pre-necking nanohardness vs. true plastic strain for S304000 showing linear trend likewise flow stress for the same plastic strains range.

It may be inferred from such a result that, likewise flow stress, nanohardness increases linearly with plastic strain and only its curve is shifted up in the MPa scale. A suitable constraint factor C , will translate nanohardness values into flow stress values. It is obvious that to support such a statement, more evidence has to be found studying more materials with various types of hardening behavior, and within wider ranges of plastic deformation.

One may argue that the entire plastic strain range could have been fitted with either, linear or power law, but the error when fitting the post-necking data with a power law was one order of magnitude less than that of the linear fit and vice versa for the pre-necking data.

4.8 Comparison Between Experimental Results to other Models.

It was mentioned earlier in this dissertation that the correction, based on geometrical features, proposed by Bridgman provides a good estimation of the true characteristics of necking in steels, however, it cannot be applied to describe other type of metals due to large errors with respect to experimental data. Equation (1.27) was used to

obtain the Bridgman correction factor $B = 0.8103$ with $a = 2.46$ and $R = 2.26$ as inputs (measured on the post-test tensile specimen).

FIGURE 4.12(a) presents all the true stress-strain data for G10180 steel from compression and tensile test; corrected post-necking by nanoindentation, and a single point after fracture with and without Bridgman correction for the fracture point. FIGURE 4.12(b) shows the curves for C11000 copper and FIGURE 4.12(c) does for S30400 stainless steel. In all three cases, the curve corrected by the proposed method produces a value of the flow stress at fracture lower than the one measured from the final geometry as expected. For G10180, the flow stress derived from nanohardness is even less than the corrected point by Bridgman method. C11000 and S30400 have significantly lower corrected values of the true fracture stress than those measured from final geometry; C11000 in particular exhibited a corrected value which is almost half of the uncorrected one. Another comparison arises from the fact that, in some cases, the Hollomon equation is used to extrapolate the true stress-strain data; very rough approximation judging from FIGURE 4.12. The mentioned differences in the true fracture stress values are correlated to the percentage of reduction of area, %*RA*. TABLE 4.1 presented %*RA* showing that the largest correspond to C1100, then S30400 and finally G10180 in decreasing magnitude. Or, to put it in other way, the more severe the necking phenomenon is, the largest the difference between corrected and uncorrected values of the true fracture stress.

In reference [11] new formulae for the correction of stresses at the neck are provided. For large strains, they found that the poorest correction was given by the Bridgman method amongst all. Likewise the present study, their empirical formula yields lower values for true stresses at the neck than Bridgman's.

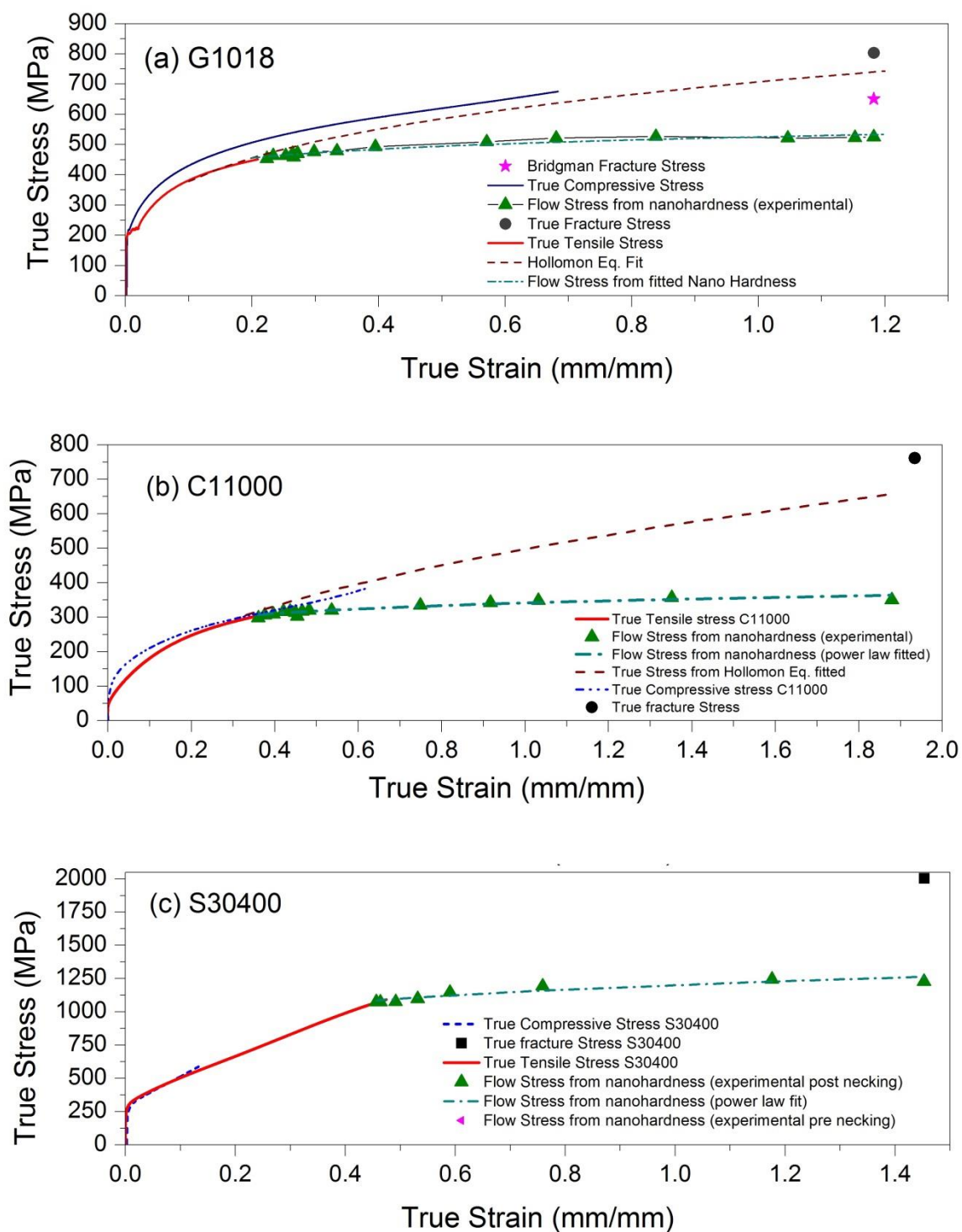


FIGURE 4.12: Comparison of the corrected curve to all true stress-strain data (a) G1018 Steel, (b) C11000 copper and (c) S30400 stainless steel.

It is important to note that the correction shown is for the uniaxial tensile stress since it is based on hardness-uniaxial flow stress relationship; in other words, the method separates out the effects of the triaxial stress-state at the neck on the uniaxial true stress-strain curve, which is the cause of increasing values of the true stress at the end of the tensile test experiment.

4.9 Strain Rate Sensitivity at the Neck Region.

Results from Indentation strain rate sensitivity test are given in FIGURE 4.13. Chapter 5 provides a brief background theory on the indentation strain rate sensitivity and the way it is measured by the indentation technique.

The plots in FIGURE 4.13 show how the strain rate sensitivity of the metals studied progress as the plastic strain is more severe towards the necked region. The increase in the initial (created during the tensile test) plastic strain along the longitudinal axis is accompanied by a change in the strain rate sensitivity index m , equation (5.9). This trend is seen by the change in the slope of the linear fit of the data for the individual plastic strains measured for the three materials. Only in the case of G10180, the highest slope is coupled with the highest hardness values for the indentation strain rates studied. FIGURE 4.13(a) shows how the slope of the linear fit increases with higher values of hardness and plastic strain; that is, the necking causes the G10180 to be more strain rate sensitive. The hardness changes (increases) more rapidly in response to plastic deformation during necking. For C11000, the strain rate sensitivity does not change markedly in the more strained material at the neck. There is a mild increase in m at the very tip, but it is not significant. However, the interval of nanohardness for each strain

rate tested is large compare to the other two materials, exhibiting very clear positive strain rate sensitivity.

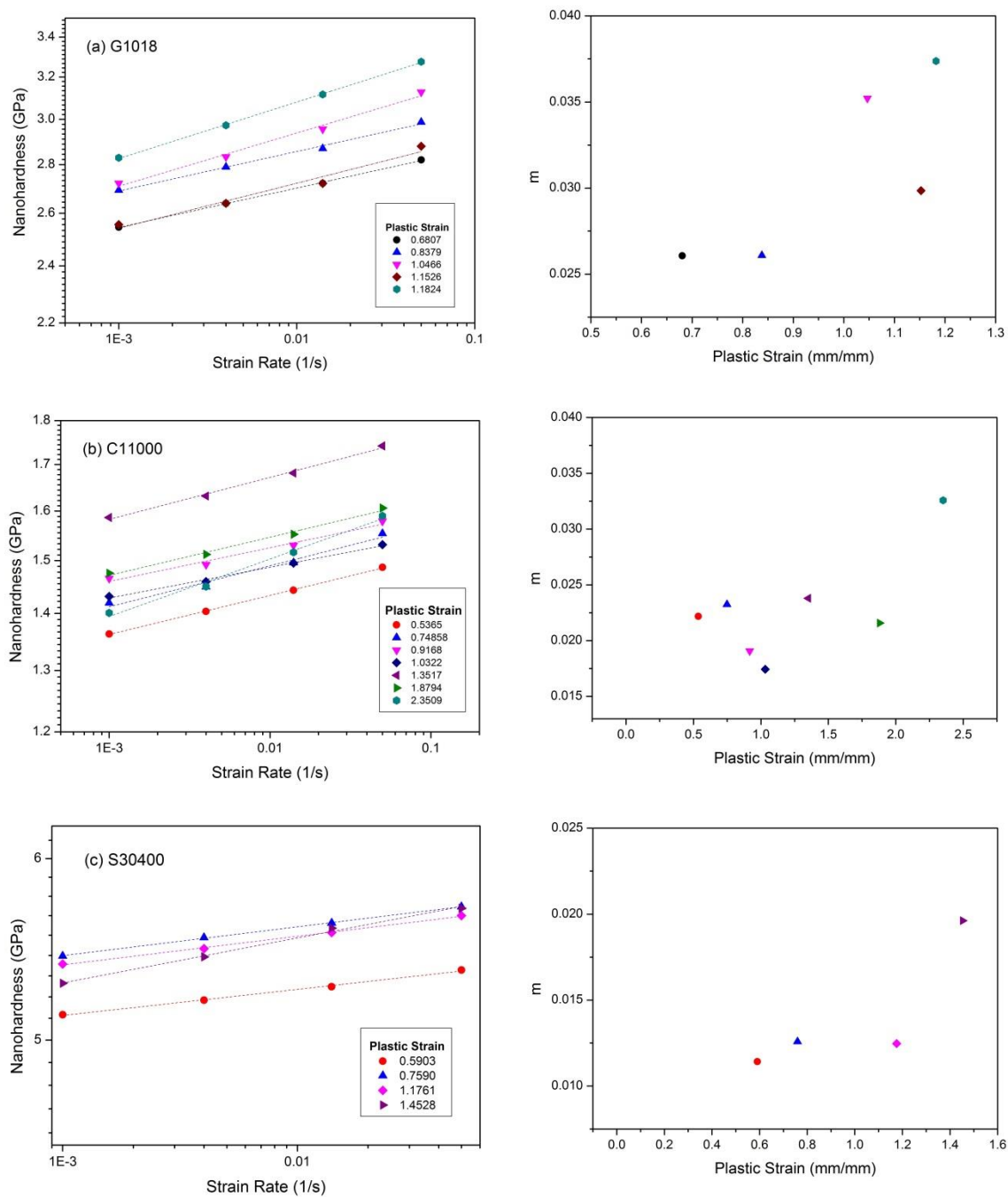


FIGURE 4.13: Strain Rate Sensitivity (SRS) of G10180, C11000 and S30400 at the neck. (a), (c) and (d). Nanohardness vs. strain rate, and (b), (d) and (f) strain rate sensitivity exponent m vs plastic strain for the three materials respectively.

S30400 displays the lowest indentation strain rates sensitivity at the neck. This is indeed meaning that the higher rate of straining does not affect substantially its hardness. i.e., the strain rate sensitivity is limited. Similar behavior for G10180 is exhibited.

4.10 Limiting Factors in the Research of this Dissertation.

Some factors that might have affected the experimental results and can make the corrections presented in this dissertation to have a limited scope includes: machine calibrations, homogeneity of the materials tested, surface roughness among other aspects.

Machine and instrument calibration is a key factor that might have influenced the experimental results at most. Large machine compliances will affect the magnitudes of the strains measured in tension, compression and nanoindentation. During tensile test, this effect is neutralized by using the video extensometer (non-contact) which measures in the elongation of the sample at regular intervals of time; unfortunately, such an extensometer cannot be used in compression due to the size of sample, leaving the measurement of the instantaneous height to the actual distance between the parallel platens. This leads to the need for machine compliance correction. [88]. In the case of instrumented nanoindentation, the value of P/S^2 (equation (1.41)) for fused silica standard sample was within the tolerance of $0.0015 \pm 0.0001 \text{ GPa}^{-1}$, according to reference [50].

As it was mentioned earlier in this chapter, the value of the nanohardness obtained from a single indent is highly susceptible to the topography and state of the surface. The effect of the surface roughness is diminished by polishing the material specimens as described in chapter 3. Still, the fact that it is a manual process makes it sensitive to misalignment on the perpendicularity of the applied pressured to the specimen surface.

For instance, the asymmetric patterns shown in the hardness and plastic strains contours maps could be due to uneven polished surfaces. In terms of topography of the sample, it was pointed out that the higher density of microvoids close to the fracture tip make the material at that section less dense, since more empty-material areas are present. On the other hand, some of those microvoids have relative sizes comparable to that for the Berkovich tip. The anisotropy effect when making single nanoindentations is counterbalanced by performing many indentations (about 1000) all over the surface (for example FIGURE 3.3); in this manner, the properties will be that for an isotropic material.

4.11 Optical Microscope and SEM Images for G10180.

The grain's features of G10180 varied along the longitudinal axis as a result of elongation in the axial direction and reduction in the diameter as the necked region is approached. The grain size variation in both directions, diametral (transverse) and longitudinal (axial) is presented in FIGURE 4.14. The micrographs at the top of the figure (both at X100) reveal how the equiaxiality of the grains closer to the grip section is lost as a result of the heavily large deformation during necking. However, the effective size maintains its original value. FIGURE 4.14 (bottom) shows how the longitudinal dimension departs from the radial dimension as the neck approaches; the average size value is the same throughout the axial direction, being close to 40 μm .

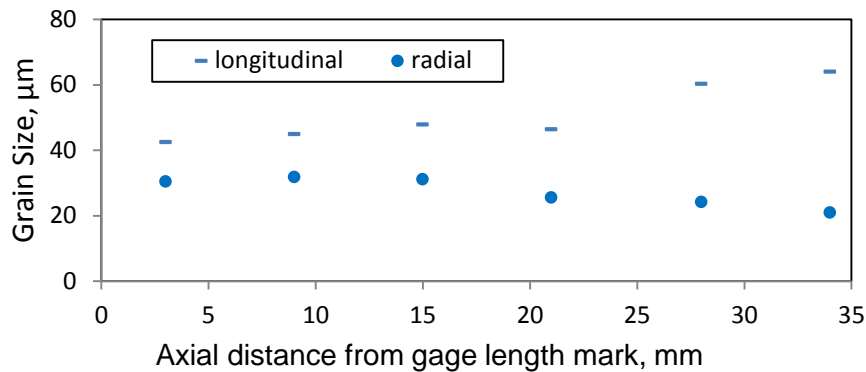
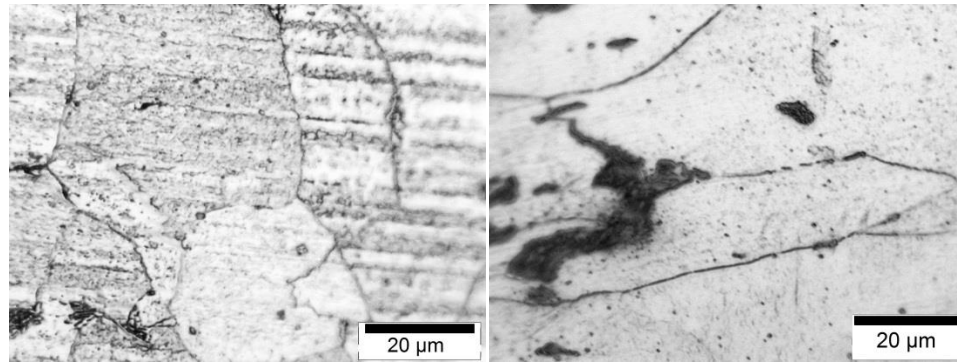


FIGURE 4.14: Grain size of G10180. Top left: micrograph taken at X100 showing grain features at the grip section. Top right: micrograph taken at X100 showing elongated grains at the neck region. Bottom: Gradient of grain size and orientation along L_s .

FIGURE 4.15 contains the SEM images of G10180 taken at some key locations. The images at the top illustrate the characteristic dimpled surface of a ductile failure. It can be seen that the size of the microvoids is very diverse. Some relatively big voids are the result of the coalescence of small ones during the fracture process, as the MVC (microvoid coalescence) theory explains [99, 100]. Furthermore, the size of some of those microvoids is of the order of the Berkovich indents as depicted in FIGURE 4.15 bottom left, where an array of 4 indents is surrounded by some microvoids. Also, it is worth noticing that some of the indents exhibit pile-up phenomenon around it, but others do not. This may be an indication of some degree of strain hardening that the material is still able to carry on. A panoramic view of the same array of the indents which is very

close to the neck is shown in FIGURE 4.15 bottom right. The fracture surface on the right displays microvoids that might be affecting the nanohardness results since the scale size of both, the indents and some microvoids underneath the polished surface are close to each other. These images support the explanation given above about the decrease in nanohardness at the regions very close to the fracture tip.

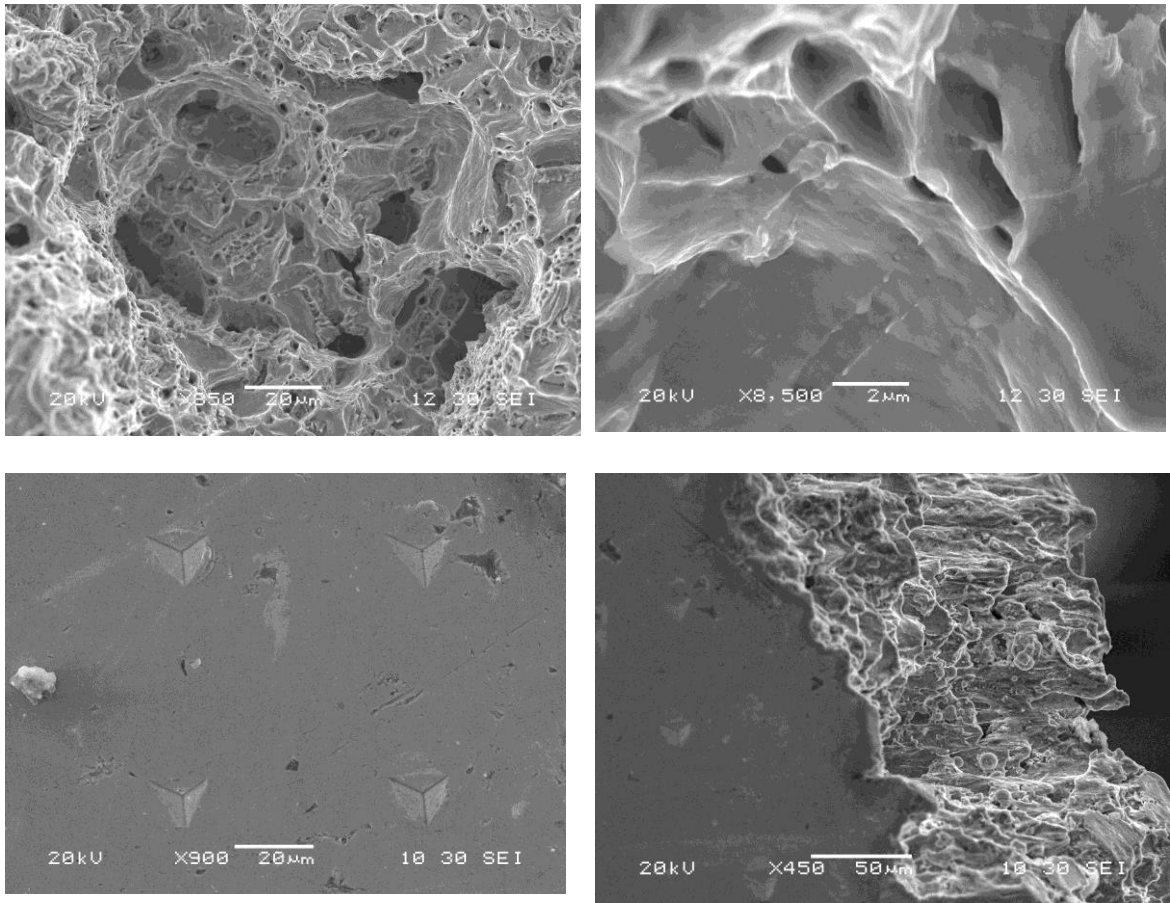


FIGURE 4.15: SEM images of G10180 steel. Top left: microvoids at the center of the failure. Top right: microvoids in the range of 0.5-1 μm. Bottom left: array of four Berkovich indentations at the neck region. Bottom right: Berkovich indentation of comparable size to microvoids at the neck.

CHAPTER 5: EVALUATION OF MECHANICAL PROPERTIES OF ECAE COPPER VIA INSTRUMENTED INDENTATION

5.1 Introduction

Traditional cold metal forming processes, such as extrusion, forging, drawing and rolling are well known to be an effective way to modify the mechanical properties, i.e., improving the strength, of metals [101]. This improvement is achieved by reducing the cross-section of the billet progressively, and therefore, refining the grain size of the metal; the grain size of the metal is a factor that affects its strength the most, as Hall and Petch stated in their investigations during the 1950s, which resulted in an equation known as the Hall-Petch relationship relating the yield strength, σ_y to the grain size, d , as follows

$$\sigma_y = \sigma_0 + k_y d^{-1/2} \quad (5.1)$$

where σ_0 is the friction stress and k_y is a constant of yielding (Hall, 1951 and Petch, 1953). Equation (5.1) shows that the yield strength increases as the grain size is reduced, thus showing the importance to make materials with ever finer grain sizes.

The plastic deformation processes mentioned above require high pressures and expensive equipment and lead to a non-uniform distribution of stress-strain within the material. Also, these processes are incapable of achieving special structures on new materials (ultrafine-grained) with a limited capacity of producing grain sizes below few micrometers [102]. Ultrafine-grained materials (UFG) refer to polycrystalline materials

having a very small average grain size of about 1 μm or less, and can be synthesized in a “bottom-up” or “top-down” approaches. Bottom-up methods usually involve assembling individual atoms or consolidating nanoparticles or powders to form bulk forms. Techniques such as powder metallurgy, physical vapor deposition, and so on and so forth, belong to the bottom-up category. Top-down methods usually start with coarse-grain bulk solid and process them by heavy straining to refine the grain size into ultrafine grain or nanocrystalline regimes (grain size smaller than 100 nm), respectively. The latter processes are primarily grouped in what is known as severe plastic deformation (SPD) processes, characterized by imposing high strains while forming the bulk solid without altering the dimensions of the solid significantly. There are a number of variants of SPD, such as equal-channel angular pressing (ECAP) or extrusion (ECAE), high-pressure torsion (HPT), accumulative roll bonding (ARB), etc. The developments in the SPD processing date back to Bridgman’s experiments during the 1950s. Bridgman attempted to largely deform fairly brittle metals, under high applied pressures, to improve their mechanical properties. More specifically, metal disks are subjected to torsional straining [40]. Even though the 0.2 GPa of pressured applied was not enough to achieve significant improvements in the properties, his work laid ground for further SPD processing techniques, particularly HPT investigations [102].

One of the most successful SPD processing technique has been the equal channel angular extrusion (ECAE), also denominated equal channel angular pressing (ECAP), which was invented in the 1970s in the former Soviet Union [103] by Vladimir Segal [101] but did not receive considerable attention within the wider scientific community until the 1990s. Segal’s method was based on his observation that large volumes of

materials can be subjected to simple shear to improve their properties by changing their microstructure. The ECAE method consists of making a conveniently lubricated billet pass through two channels intersecting at an angle Φ ($60^\circ < \Phi < 135^\circ$), inside a die, by means of a punch; the die may have a rounded corner with an angle $\Psi > 0$ or simply $\Psi = 0$ [104] as the schematic in FIGURE 5.1 depicts; as the billet moves from one channel to the other, deformation by simple shear at the crossing plane of the channel takes place, and it emerges at the other end with no change in the cross-section dimensions, and uniformly deformed throughout it except at its ends [101].

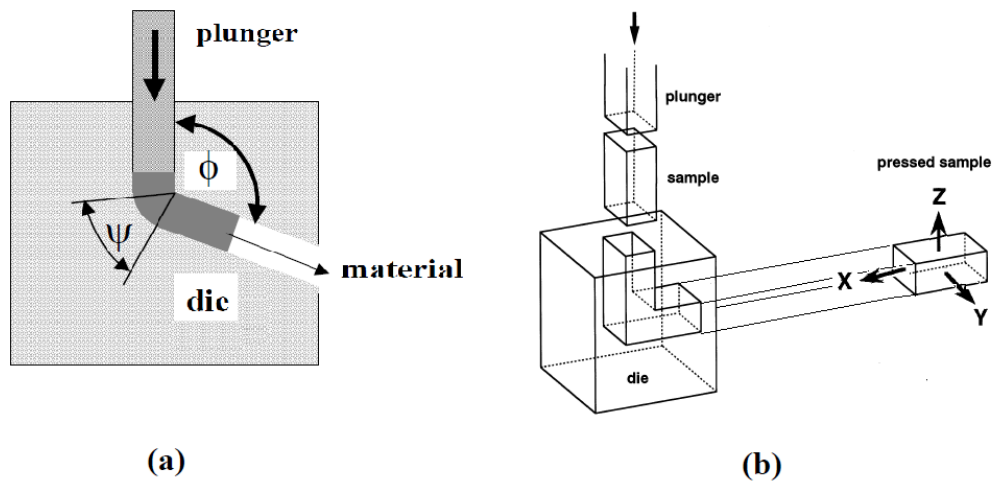


FIGURE 5.1: (a) Schematic of an ECAE die showing its geometry [104]. (b) Schematic illustrating the ECAE process and coordinates [105].

The microstructure is refined successively allowing the same billet to undergo multiple passes. By changing its orientation between consecutive passes, i.e., rotating the billet in multiples of 90° angles with respect to any of the x, y, z axis, diverse structures and textures are achieved since different slip systems are being activated. In other words, the structure and properties are functions of the route followed during the ECAE process,

and at the same time, of the geometry of the die since the strain induced in each pass is governed by the angle of intersection, Φ , and the arc of curvature, Ψ , in minor proportion. The equivalent strain, ε_N , after a number of passes, N , depends on these geometrical parameters, and it is expressed in a general way by equation (5.2) [106].

$$\varepsilon_N = \frac{N}{\sqrt{3}} \left[2 \cot \left(\frac{\Phi}{2} + \frac{\Psi}{2} \right) + \Psi \operatorname{cosec} \left(\frac{\Phi}{2} + \frac{\Psi}{2} \right) \right] \quad (5.2)$$

In the common particular case of $\Psi = 0^\circ$, and the angle of intersection is taken as $\Phi = 2\varphi$, the equivalent strain after N passes is estimated by the expression found by Segal;

$$\varepsilon_N = \frac{2N}{\sqrt{3}} \cot \varphi \quad (5.3)$$

There are three conventional ECAE routes: route A, where the billet is not rotated between passes; route B, where the billet is rotated 90° (alternatively, B_A , or in one direction only either clockwise or counterclockwise, D or B_C) between passes; and route C where the billet is rotated 180° between passes. There are other routes that are considered hybrid. They are: route E, where the billet is rotated 180° between passes 1 and 2, 3 and 4, and rotated 90° between passes 2 and 3; route F follows rotations of 90° , 180° , 270° between passes, respectively.

Routes E and F have the characteristic for an element in the central section of the billet to return to its original shape after four passes. In other words, the route is complete after four passes. Also, the product yield in the hybrid routes, as the number of passes increases, does not drop as rapidly as the conventional routes do. Therefore, the hybrid routes are more efficient than the conventional A, B and D [107]. TABLE 5.1 provides the volume percent of ECAE fully worked material for routes A through F for number of

passes 1 to 8. The billets have a square cross section and an aspect ratio (length/height) of 6.

TABLE 5.1: Product yield in percentage for ECAE processing routes as a function of number of passes. Adapted from [107].

Route	Rotations before extrusion	Number of passes							
		1	2	3	4	5	6	7	8
A	0°, all passes	83.3	75	66.7	58.3	50	41.7	34.7	29.8
B(B _A)	90°, <i>N</i> even, 270° <i>N</i> odd	83.3	77.8	72.2	66.7	61.6	55.6	50.2	44.4
C	180°, all passes	83.3	83.3	83.3	83.3	83.3	83.3	83.3	83.3
D(B _C)	90°, all passes	83.3	77.8	73.6	72.2	72.2	72.2	72.2	72.2
E	180°, 90°, 180°	83.3	83.3	77.8	77.8	77.8	77.8	77.8	77.8
F	90°, 180°, 270°	83.3	77.8	77.8	77.8	77.8	77.8	77.8	77.8

It is worth mentioning that only the percentages of material shown can be accounted to have uniform microstructure and no cracks.

A better understanding of the influence of the number of passes on the mechanical properties of ECAE processed materials is paramount. It is equally important to explore the advantages of the hybrid routes compared to the conventional ones. The purpose of the present research is to utilize instrumented nanoindentation to probe the mechanical properties of copper, subjected to equal channel angular extrusion processing from 1 to 32 passes, at different strain rates.

5.2 Experimental Procedure

Commercial copper with a purity of 99.98% was used to manufacture bar samples utilized for all passes. The samples were annealed at 500°C for one hour, and were processed via ECAE following route E thereafter; the number of passes to which the samples were subjected were 1, 2, 4, 8, 16, 24, and 32. The geometry of the ECAE facility (tooling) was $\Phi = 90^\circ$ and $\Psi = 90^\circ$. FIGURE 5.2 is a schematic of route E followed in this study.

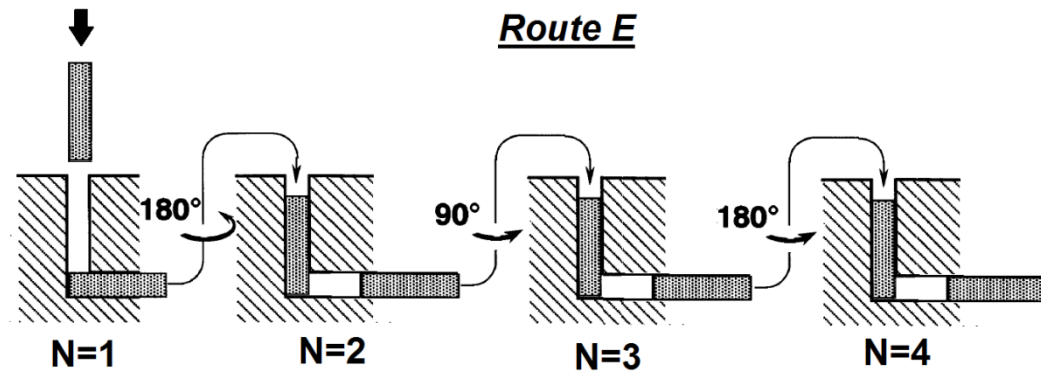


FIGURE 5.2: Hybrid route E following 180° - 90° - 180° rotation pattern. Adapted from [105].

After ECAE processing, specimens of dimensions $5 \times 2.5 \times 2.5 \text{ mm}^3$ were cut out of the bars by wire EDM (electro-discharge machining) for analysis. Subsequently the small cuts were manually and machine grinded with decreasing particle size sandpaper up to Grade 1200, and then wheel-polished with a cloth and alumina suspension of 0.3 and $0.05 \text{ }\mu\text{m}$, respectively.

The mechanical properties of the samples were probed by means of instrumented nanoindentation performed utilizing a Nanoindenter G200 from Agilent Technologies® with a diamond Berkovich tip. Indentation hardness and indentation elastic modulus were obtained at different strain rates ranging from $2.5 \times 10^{-3} \text{ 1/s}$ to $5.0 \times 10^{-2} \text{ 1/s}$, and to a maximum depth of indentation, h_{max} , of 2000 nm for the 10 indentations made on each sample. All the indentations were performed following the CSM (continuous stiffness measurement) standard method for elastic modulus, hardness and tip calibration. The advantage of using the CSM method relies on controlling the total displacement into the material surface for each indentation [86]. In this manner, one is able to have a relatively

constant indentation strain rate. Lucas and Oliver [108] proposed that technique for conducting constant indentation strain rate experiments; departing from equations (1.29) and (1.39) revisited (assigning the letter P instead of F to refer to the load on sample),

$$H = \frac{P}{A_c} = \frac{P}{ch_c^2} \quad (5.4)$$

where c is taken as a constant with a value of 24.56 for an ideal Berkovich geometry tip.

Equation (5.4) is then differentiated with respect to time to cast

$$\dot{H} = \frac{\dot{P}}{ch_c^2} - \frac{2P\dot{h}}{ch_c^3}$$

$$\text{and } ch_c^2 = \frac{P}{H}$$

$$\text{thus, } \frac{\dot{H}}{H} = \frac{\dot{P}}{P} - \frac{2\dot{h}}{h}$$

then simplifying and rearranging the terms for convenience,

$$\frac{\dot{h}}{h} = \frac{1}{2} \left(\frac{\dot{P}}{P} - \frac{\dot{H}}{H} \right) \equiv \dot{\epsilon}_i \quad (5.5)$$

where $\dot{\epsilon}_i$ is the effective indentation strain rate. Provided that hardness at indentation depths larger than 500 nm turn out to be constant for the type of material studied here, and therefore, it is not affected by the ISE (indentation size effect), equation (5.5) can be even further simplified as

$$\dot{\epsilon}_i \approx \frac{1}{2} \frac{\dot{P}}{P} \quad (5.6)$$

The term “constant indentation strain rate” refers to an effective averaged value over the total deformed volume under the indenter tip since the stresses and strains change in a non-linear manner throughout the elastic-plastic indentation zone. In this

sense, the strain rate differs from that measured in a uniaxial tension test where the stress state is considered constant [109]. During the process of indentation, the CSM method is configured to control the load in such a way that the loading rate divided by the load on the contact surface is held constant at a value of the target strain rate. This target or applied strain rate is related to the effective indentation strain rate as follows,

$$\dot{\varepsilon}_i \approx \frac{1}{2} \frac{\dot{P}}{P} = \frac{1}{2} \dot{\varepsilon}_a \quad (5.7)$$

where $\dot{\varepsilon}_a$ is the applied indentation strain rate equal to \dot{P}/P .

5.3 Results and Discussion

FIGURE 5.3 shows the average load – displacement curves at different indentation effective strain rates for ECAE copper in the annealed condition (0 passes), 4, 24 and 32 passes following route E; the maximum depth of penetration were 2000 nm for all cases. In all plots, for each number of passes depicted, the maximum indentation load rises as the indentation strain rate is increased. However, the effect is evidently different in each case. For the annealed state (N=0 passes) the maximum load is the smallest for each indentation strain rate compared to the other cases, and there is a mild increase with increase strain rate. Contrary to the first case, the effect is markedly stronger for the N=4 passes FIGURE 5.4(b). The maximum load increases considerably between 0.0025 1/s and 0.050 1/s, and maintain and increasing trend up to the highest strain rate. For the N=24 passes, FIGURE 5.4(c), the change in strain rate does not seem to affect significantly the magnitude of the maximum load, and also the curves are very close to each other as if the material were not being affected by the strain rate nor by the higher number of passes. For the indentation strain rates of 0.0025 1/s, 0.025 1/s, and 0.050 1/s the curves almost overlap each other, indicating no dependence on the strain

rate, and the level of maximum load is the second lowest amongst all. In the case of $N=32$ passes, again, the trend of increase load with strain rate is recovered and the material with highest degree of deformation is just the second highest in regards to the maximum load achieved. It can be seen that all the indentation experiments were carried out at a fixed depth of penetration or maximum displacement into surface to circumvent the depth dependence of the hardness. In this case, h in equation (5.5) is taken as h_c .

As the number of passes increases, more plastic strain has been imposed on the material leading to microstructural changes responsible for improvement in the strength, and, therefore, hardness. This is illustrated in FIGURE 5.4, where for every number of passes (lower horizontal axis) the nanohardness increases with increasing values of the indentation strain rate. It starts with the expected lowest value at its annealed state ($N=0$), and it then increases up to $N=4$ passes where a clear peak is reached. That is to say, for every value of the indentation strain rate, the maximum nanohardness value is achieved at $N=4$ passes. Then they start decreasing consistently reaching the lowest value (for the ECAE deformed copper) at $N=24$ passes, and finally resume increasing again afterwards. For instance, a nanohardness value of 2.01 GPa is achieved at 0.050 1/s for $N=4$, while for the same indentation strain rate only 1.67 GPa is obtained for $N=24$. The upper horizontal axis represents the equivalent strain, given by Equation (5.2), accumulated with the number of passes for the geometry mentioned above.

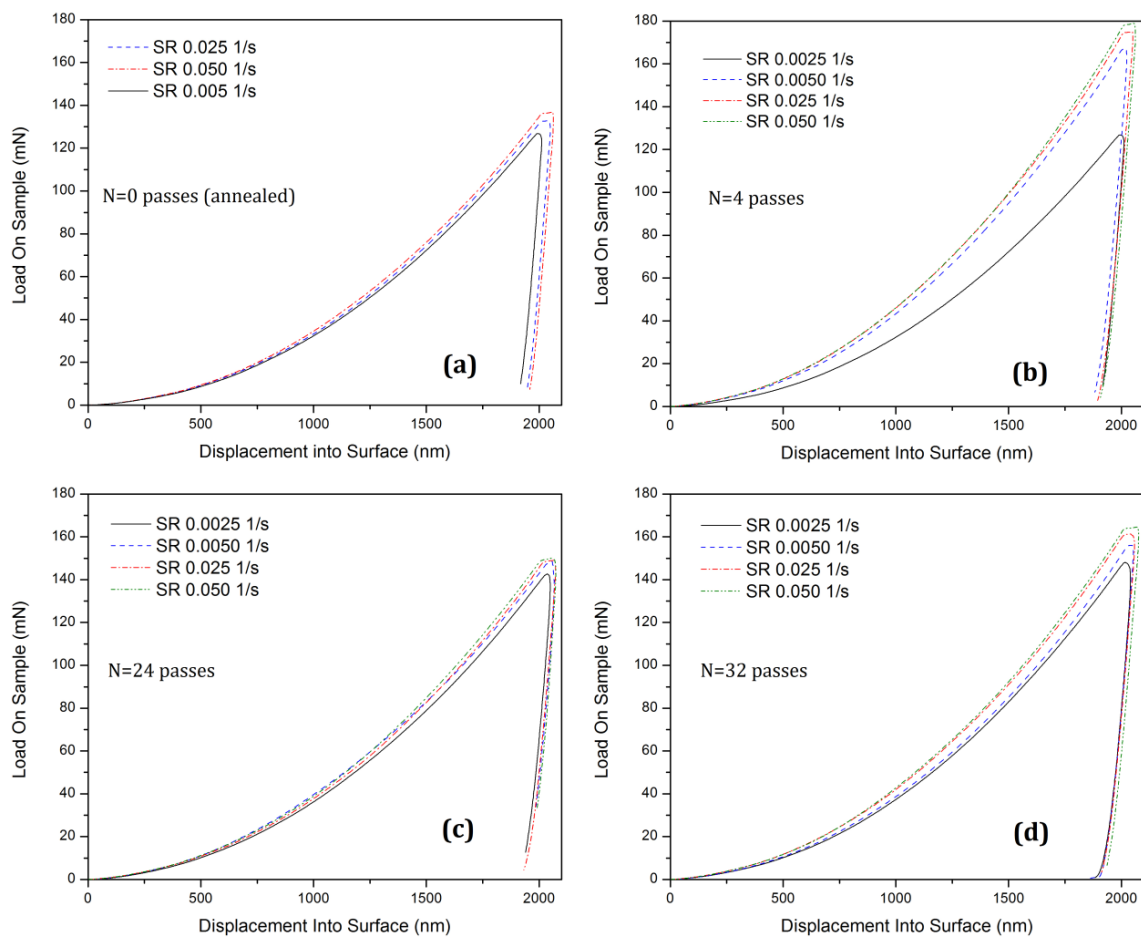


FIGURE 5.3: Load - displacement curves for ECAE copper for (a) N=0, (b) N=4, (c) N=24 and (d) N=32 passes showing the influence of the indentation strain rate on the maximum load.

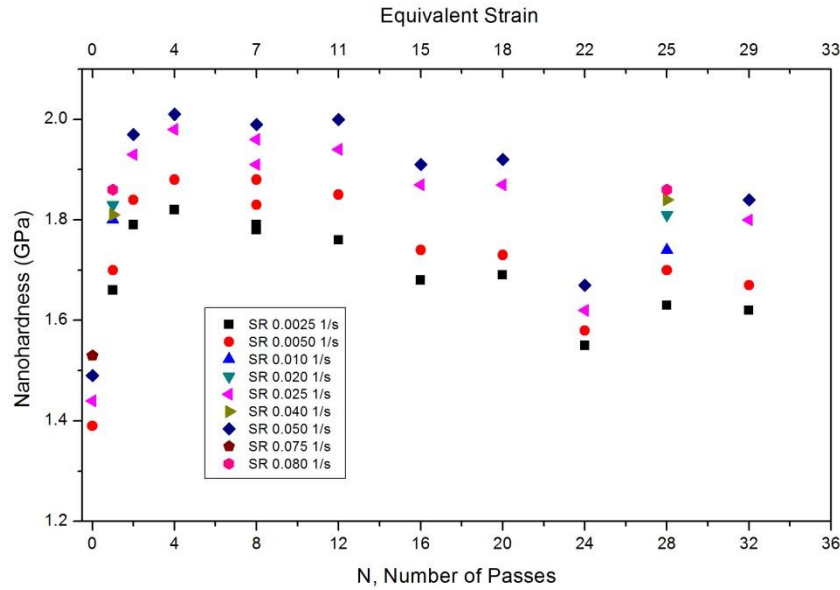


FIGURE 5.4: Variation of Nanohardness with number of passes for ECAE copper. Tests performed at various constant indentation strain rates. The nanohardness peak is reached at $N=4$ passes.

The behavior of nanohardness as a function of the number of passes is related to the microstructure achieved during the ECAE process. The microstructure has to be observed from the three orthogonal planes (see FIGURE 5.1) and will be strongly dependent on the route followed during the ECAE process. Besides dislocations mechanisms, phenomena such as grain rotation and grain boundary sliding are prone to influence the deformation behavior during ECAE [110]. Lamellar boundaries (LB) characterize the microstructure, elongated grains with subgrains inside. As the number of passes increased the microstructure becomes more homogeneous. Such observations were made in a previous study by Dalla Torre et al [111], following route D or B_C , and up to 16 passes. They reported the change in the microstructure from mostly lamellar at lower number of passes, $N=1$ and $N=2$, similar to that of rolling, and then higher fractions of the grains turn out to be equiaxed at $N=4$ and $N=8$, to a greater extent at even higher

number of passes. At the same time, signals of recovery at the grains interior and grain boundaries, and lowering of dislocation densities are seen for higher number of passes due to dynamic recovery and recrystallization that leads to the formation of low-energy dislocation (LED) structures. However, the complexity in the nature of the microstructure is reflected in differences in the measurements of the feature sizes for similar materials studied. Microstructures obtained by different routes are also diverse [112]. What is common amongst the results from the literature is that the strength reaches a maximum around $N=4$ passes due to the saturation of dislocations at the constrained low angle grain boundaries, and a softening effect occurs at subsequent passes, most likely, due to dynamic recovery and recrystallization processes within the strained microstructure.

From a different perspective, nanohardness, H , number of passes, N , and strain rate, $\dot{\epsilon}$ or SR, are correlated in a manner where the strain rate effect can be observed more clearly. Equation (1.21) describes the strain hardening effect on the flow stress (true stress). Similarly, for some non-linear materials, the rate of application of the strain affects the mechanical response which can be modeled using the empirical power law relationship

$$\sigma_T = K' \dot{\epsilon}^m \quad (5.8)$$

where σ_T is the true stress, $\dot{\epsilon}$ is the true strain rate, K' is a proportionality constant that corresponds to the stress value for a strain rate of 1.0 1/s, and m is the strain rate sensitivity (SRS) exponent. Materials with a low m value are not strain rate sensitive; on the other hand, those with a high m are very sensitive to changes in the strain rate. High values of m provide indication of the superplasticity of a material. The strain rate

sensitivity exponent can be expressed in terms of hardness and indentation strain rate as in the following definition [113],

$$m = \frac{\partial(\ln H)}{\partial(\ln(\dot{h}/h))} = \frac{\partial \ln H}{\partial \ln \dot{\epsilon}} \quad (5.9)$$

and is a measure of the sensitivity of the hardness of a material as the strain rate changes.

The strain rate sensitivity exponent can be related to the activation volume of plastic deformation, v^* , as follows [114],

$$m = 3\sqrt{3} \frac{kT}{H \cdot v^*} \quad (5.10)$$

where k is the Boltzmann constant, and T is the absolute temperature.

The variation of nanohardness with indentation strain rate for the ECAE copper subjected to 1 to 32 passes under route E, and for the annealed state is plotted in FIGURE 5.5. The trend of how the nanohardness increases from low to high indentation strain rates values is seen more clearly. Moreover, it is visibly observable that for N=4 passes the nanohardness values take their maximum at each indentation SR value (pink downward triangle), and the opposite behavior is observed in samples corresponding to N=24 passes (olive color pentagons). What is even more evident is the trend that a linear fit will follow if one was to fit each set of data for every number of passes. That is to say the strain rate sensitivity exponent, m , is nothing but the slope of the linear fit for each number of passes since FIGURE 5.5 is plotted in a log-log form as was stated by equation (5.9).

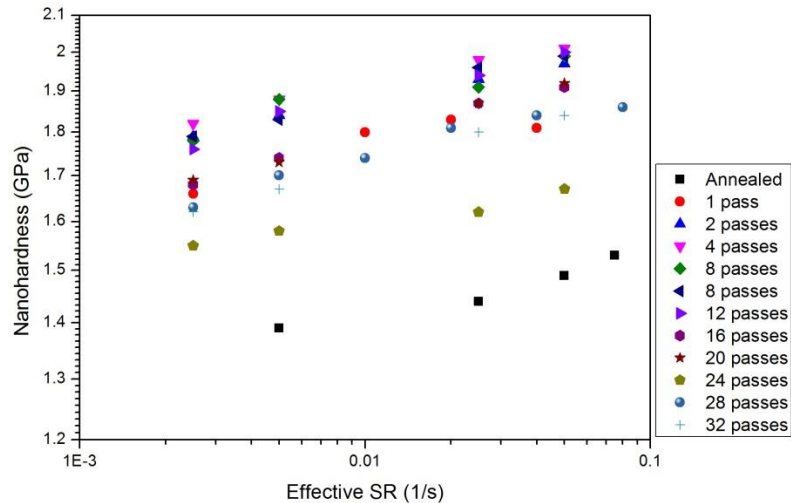


FIGURE 5.5: Nanoindentation hardness as function of indentation strain rate for ECAE copper from $N=0$ (annealed state) to $N=32$ passes under route E. $\log H$ vs. $\log \dot{\epsilon}$.

The slope for each number of passes was obtained by performing a linear fit for each N , including $N=0$ or the annealed state. Those values are plotted in FIGURE 5.6 where it is observed that two points deviate from the rest. The first is the red one, corresponding to the Rod Number 3 that has a lower value of m for the same number of passes of the sample taken from Rod 2. The second one is the point corresponding to m at $N=24$ passes, which indicates that the material of that state becomes much less rate sensitive than even the non-deformed material in its annealed state. This behavior could have been predicted by observing the load-displacement curves in FIGURE 5.3(c) where the change in SR does not seem to affect in a significant manner the maximum load as it was pointed out above. The m exponent starts with a value of 0.033, and then it decreases for $N=1$ and $N=2$ passes, and starts increasing from $N=4$ passes. Disregarding for a moment the red point the trend for m is to have higher values at greater number of passes until $N=20$ where the abrupt drop at $N=24$ breaks a possible plateau that could follow next.

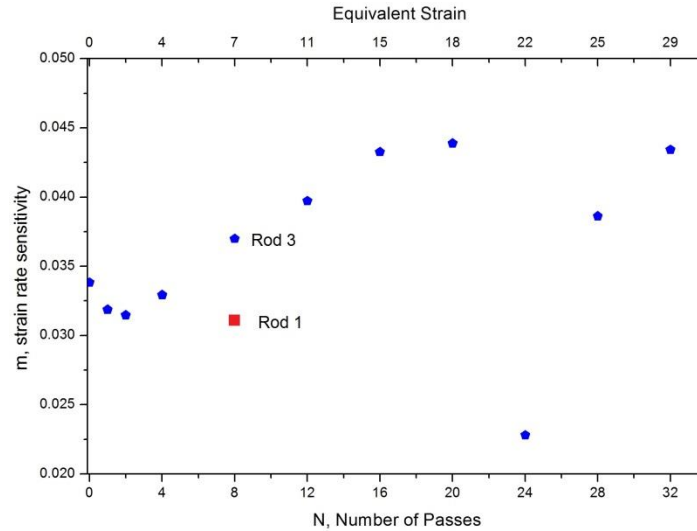


FIGURE 5.6: Strain Rate sensitivity exponent obtained by nanoindentation on ECAE copper (Route E) as function of number of passes. For $N=8$, data for two different rods is provided.

A possible explanation for the red point is that the sample was taken from a section of the billet that was not fully processed or affected by another processing or testing error, while the point for $N=24$ indicates a more complex explanation presumably involving a microstructural phenomenon.

Other values of mechanical properties and strain rate sensitivity for ECAE copper can be found in references [115-117], and literature for microstructural development and characterization in [112, 118, 119].

A complementary study to the present one was performed on the same bulk ECAE copper with the aim of obtaining a constitutive model based on the rate dependence behavior of the UFG copper [120]; some of the theoretical and empirical models are studied and combined in an attempt to explain the complex plastic deformation behavior of ECAE copper following route E.

5.4 Summary and Concluding Remarks.

An analysis of bulk polycrystalline copper subjected to Equal Channel Angular Extrusion (ECAE) from 1 to 32 passes under route E was performed. As one of the Severe Plastic Deformation (SPD) processes, utilized to improve the properties of materials by decreasing the grain size to the ultrafine grain regime, ECAE proved to increase the hardness (nanohardness in this study) and thus the strength of copper by successive passes. The maximum nanohardness value is achieved after $N = 4$ passes, which coincides with other studies for different routes. Then after reaching a saturation within the microstructure, a decrease will follow until an abrupt drop at $N = 24$ passes is observed. For the $N=28$ and $N=32$ the values increased again. This particular behavior was noticed for different values of effective indentation strain rate at which the experiments were performed. Bulk UFG – copper demonstrated to be strain rate sensitive represented by the slope of the linear fit in the $\log H$ vs. $\log \dot{\epsilon}$; values of $m = 0.033$ for the annealed case and $m = 0.045$ for $N=18$ and $N=32$ were observed. The lowest value of the strain rate sensitivity exponent was obtained for $N=24$, which also held the lowest nanohardness values for the strain rates studied. This reduction in hardness and strain rate sensitivity is presumably due to the process of dynamic recrystallization; a complete study of the microstructure, such as TEM, and EBSD analysis, may be conducted to characterize ECAE copper under route E, and inquire about the possible factors affecting the mentioned behavior.

The instrumented nanoindentation technique proves to be an efficient method to probe the plastic deformation mechanism of UFG materials, without the need of machining high-cost and complicated samples for other types of mechanical testing.

However, it will be worthwhile to utilize conventional mechanical testing, such as uniaxial tensile test, and/or compression test, and testing at higher strain rates and higher temperatures in order to validate and extend the nanoindentation results and to provide more information about the complex plastic behavior of materials subjected to severe plastic deformation processes.

CHAPTER 6: CONCLUSIONS AND FUTURE WORK

The research presented in this dissertation is purely experimental and opens up a new path to re-reconsider some aspects regarding hardness-flow stress relationship. A reverse analysis, i.e. nanohardness data converted to flow stress, was conducted with the purpose of correcting post-necking stress-strain data.

Three materials were studied during the research of this dissertation; low carbon G10180 steel, Electrolytic Tough Pitch (ETP) copper and austenitic stainless steel S30400. Tensile test was carried out with the aim of characterize the nonuniform plastic strain (post-necking). The first two materials, exhibited power-law strain hardening behavior and the third one linear strain hardening. The nanohardness averaged over their longitudinal direction showed an increasing trend as the necked section approaches. Berkovich and micro Vickers measurements coincide with this trend, however, both types behaved differently from one material to another. In other words, the relationship between the two of them apparently depends on the plastic strain field created on the material. This observation has to be clarified with more studies on different materials subjected under the same conditions. Nanohardness (Berkovich) exhibits a mild decrease at the very fracture tip; a size effect may be the cause. The topographic configuration of the material at the necked section is that of a material with a high percentage of dimples. The material affected by the indentation strain fields under the tip do not have a full dense material to serve as constraint. This lack of material support at the necked region is

attributed to the numerous voids and microvoids present, according to the microvoid coalescence (MVC) theory of ductile failure.

The hardness maps revealed that the hardness distribution over the entire surface is unique to each material, being S30400 the one that exhibits a better ability to distribute plastic strain more uniformly throughout the specimen than the other two materials, not to mention its high nanohardness values achieved. The slight decrease in nanohardness at the very fracture tip is evident in the hardness maps for all three materials, but this effect is less notorious with higher nanohardness values. Also, the areas with maximum nanohardness were more towards the exterior surface of the neck in G10180, and in less degree in C1100. S30400 differs from this, since the core of highest hardness values are well inside the necked region.

For each of the materials analyzed, a relationship between nanohardness and plastic strain was found. Such relationship turned out to be well represented by a power-law function. Then, Tabor's equation was utilized to find the constraint factor C , by linking nanohardness with flow stress by the plastic strain as independent variable. The constraint factors relating nanohardness to flow stress were 5.5, 4.5 and 4.5 for G10180, C11000 and S30400 respectively. The representative plastic strain ϵ_r , determined by the experimental results dictated that a unique single value is not appropriate to describe materials with different plastic behaviors. The values of the representative plastic strain were 0.028 (G10180), 0.062 (C11000) and 0.061 (S30400). It is the author's point of view that these two important parameters (C and ϵ_r) are actually two important plastic properties of the materials; then, they should be characterized experimentally in a

standardized manner such that both values can be listed, along with other properties, in tables and manuals.

The finding of the constraint factor makes the way to translate the nanohardness values to those of flow stress for the post-necking plastic strains. The corrected post-necking portion is added to the previously known true stress-strain curve. It is clear that a change in the plastic behavior has to be marked by the inflexion point on the curve when plastic instability begins, since a different strain hardening phenomenon is occurring during necking revealing a microstructural change. The corrected curve inherently separates out the effect of triaxiality on the uniaxial true stress-strain curve, provided that the nanohardness-flow stress relationship is based on uniaxial values of stress. Yet, a relationship linking both power law exponents, the one from Hollomon equation and that for the corrected curve, has to be established in the future. Based on the experimental results it is noticed that the corrected curve and the strain hardening exponent n , are in direct association, i.e., the material with higher strain hardening behavior is the one with higher exponent in the corrected curve. The corrected curve for G10180 steel provided a lower value compare to Bridgman, and in the other two materials, a much lower fracture stress value than the stress at fracture from final measurements. Additionally, lower flow stress values than the imaginary projection of the compression curve and of the Hollomon equation (G10180 and C11000). The strain rate sensitivity m , at the neck region increases with plastic strain showing its highest value at the narrowest cross section for G10180; in the case of C11000 copper and S30400 stainless steel, it remains approximately within the same low-value range. S30400 exhibits the less sensitivity among all three materials.

The method presented in this dissertation requires a complete characterization of the entire surface, i.e., instrumented nanoindentation is performed throughout the area of the sample specimen. One drawback concerns the time for testing which is considerably high; in addition to the invested time in sample preparation. Recalling that the method is purely experimental, such complete characterization would need to be done only once.

Instrumented indentation is the most suitable method to perform this characterization task because of its close control on the instrument load and displacement into surface, and its repeatability when a large number of indents are needed such as this research. An additional aspect of nanoindentation that proved its versatility was its ease to probe mechanical properties of materials. Without the need of extra sample preparation, machine set-up or especial geometry configuration, nanoindentation was used successfully to test the strain rate sensitivity of materials in the quasi-static regime.

The present research can be complemented in different ways in the future. In terms of experimental work, a larger number of materials with varied plastic behavior may be studied. Regarding instrumented indentation, it can be performed with micro Vickers to sort out some of the size effect limitations of the Berkovich indenters. From a theoretical perspective, to continue the search for a constitutive model that describes closer to reality the relationship between hardness, an elasto-plastic property, with flow stress. An adequate, rigorous and in depth finite element analysis that reproduces the experimental procedure might follow. The variables such as, strain rate, temperature, elasto-plastic properties, from this study and additional ones can be varied during modeling. Care must be taken in this simulation analysis where the risk of bias is high in the effort to obtain unique or universal values that fit all materials.

REFERENCES

1. Callister, W.D. and D.G. Rethwisch, *Materials Science and Engineering: An Introduction, 8th Edition*. 2009.
2. Tietz, T.E. and J.W. Wilson, *Behavior and properties of refractory metals*. 1965, Stanford, California: Stanford University Press. 419.
3. Lassner, E. and W.-D. Schubert, *Tungsten-Properties, Chemistry, Technology of the element, alloys and chemical compounds*. 1998: Kluwer-Academic/Plenum Publishers.
4. Wei, Q. and L.J. Kecskes, *Effect of Low-Temperature Rolling on the Tensile Behavior of Commercially Pure Tungsten*. *Materials Science and Engineering A*, 2008. **491**: p. 62-69.
5. Wei, Q., L.J. Kecskes, and K.T. Ramesh, *Effect of Low-Temperature Rolling on the Propensity to Adiabatic Shear Banding of Commercial Purity Tungsten*. *Materials Science and Engineering A*, 2013. **578**: p. 394-401.
6. Kecskes, L.J., et al., *Grain size engineering of bcc refractory metals: top-down and bottom-up--application to tungsten*. *Materials Science and Engineering A*, 2007. **467**: p. 33-43.
7. Honeycombe, R.W.K., *The plastic deformation of metals*. 1975, London: Edward Arnold.
8. Dieter, G.E. and D.J. Bacon, *Mechanical Metallurgy*. 1988: MCGRAW-HILL Higher Education.
9. Zhao, Y.H., et al., *Influence of specimen dimensions on the tensile behavior of ultrafine-grained Cu*. *Scripta Materialia*, 2008. **59**: p. 627-630.
10. Zhao, Y.H., et al., *Influence of specimen dimensions and strain measurement methods on tensile stress-strain curves*. *Materials Science and Engineering A*, 2009. **525** p. 68-77.
11. Gromada, M., G. Mishuris, and A. Öchsner, *Correction Formulae for the Stress Distribution in Round Tensile Specimens at Neck Presence*. 2011: Springer.
12. Kalpakjian, S. and S. Schmid, *Manufacturing Engineering & Technology*. 2013: Pearson Education.
13. Davis, J.R., *Tensile Testing*. 2004: A S M International.

14. ASTM, *E8/E8M - 09. Standard Test Methods for Tension Testing of Metallic Materials*. 2009, ASTM International: PA, USA. p. 27.
15. Meyers, M.A., A. Mishra, and D.J. Benson, *Mechanical properties of nanocrystalline materials*. Progress in Materials Science, 2006. **51**: p. 427-556.
16. Wang, Y.M. and E. Ma, *Three strategies to achieve uniform tensile deformation in a nanostructured metal*. Acta Materialia, 2004. **52**: p. 1699-1709.
17. Wang, Y.M., et al., *Controlling factors in tensile deformation of nanocrystalline cobalt and nickel*. Physical Review B, 2012. **85**: p. 014101.
18. Wei, Q., *Strain rate effects in the ultrafine grain and nanocrystalline regimes--its influence on some constitutive behavior*. Journal of materials science, 2007. **42**: p. 1709-1727.
19. Li, H. and F. Ebrahimi, *Ductile to brittle transition in nanocrystalline metals*. Advanced Materials, 2005. **17**: p. 1969-1072.
20. Li, H. and F. Ebrahimi, *Tensile behavior of a nanocrystalline Ni-Fe alloys*. Acta Materialia, 2006. **54**: p. 2877-2886.
21. Li, H.Q. and F. Ebrahimi, *Transition of deformation and fracture behavior in nanostructured face-centered cubic metals*. Applied physics letters, 2004. **84**(21): p. 4307-4309.
22. Ritchie, R.O., *The conflicts between strength and toughness*. Nature Materials, 2011. **10**(11): p. 817-822.
23. Kumar, K.S., H. Van Swygenhoven, and S. Suresh, *Mechanical Behavior of nanocrystalline metals and alloys*. Acta Materialia, 2003. **51**: p. 5743-5774.
24. Dao, M., et al., *Toward a quantitative understanding of mechanical behavior of nanocrystalline metals*. Acta Materialia, 2007. **55**: p. 4041-4065.
25. Koch, C.C., *Nanostructured materials: processing, properties and potential applications*. Materials Science and Processing Technology, ed. McGuire GE. 2002, Norwich: Noyes Publications.
26. Koch, C.C., et al., *Structural Nanocrystalline Materials-fundamentals and applications*. 2007, Cambridge: Cambridge University Press. 362.
27. Koch, C.C., R.O. Scattergood, and K.L. Murty. *Mechanical behavior of multiphase nanocrystalline materials*. in *Nanocomposites-Their Science, Technology and Applications, MS&T2006*. 2006. Cincinnati: TMS.

28. Valiev, R.Z., et al., *Paradox of strength and ductility in metals processed by severe plastic deformation*. Journal of Materials research, 2002. **17**(1): p. 5--8.
29. Ma, E., *Controlling plastic instability*. Nature Materials, 2003. **2**: p. 7-8.
30. Ma, E., *Eight routes to improve the tensile ductility of bulk nanostructured metals and alloys*. JOM, 2006(April): p. 49-53.
31. Gao, H.J., *Application of fracture mechanics concepts to hierarchical biomechanics of bone and bone-like materials*. International Journal of fracture, 2006. **138**(1-4): p. 101-137.
32. Gao, H.J., et al., *Materials become insensitive to flaws at nanoscale: lessons from nature*. PNAS, 2003. **100**(10): p. 5597-5600.
33. Huang, Z.W., et al., *Uncovering high-strain rate protection mechanism in nacre*. Scientific Reports (Nature), 2011. **1**: p. 148.
34. ASM, *Atlas of Stress-Strain Curves*. 2, illustrated, reprint ed, ed. A. International. 2002: ASM International, 2002.
35. Meyers, M.A. and K.K. Chawla, *Mechanical Behavior of Materials*. 2009: Cambridge University Press.
36. Czichos, H., T. Saiato, and L.L.R. Smith, *Springer handbook of materials measurement methods*. 2006: Springer Science+Business Media, Incorporated.
37. Hart, E.W., *Theory of the tensile test*. Acta Metallurgica, 1967. **15**: p. 351-355.
38. Hart, E.W., *A phenomenological theory for plastic deformation of polycrystalline metals*. Acta Metallurgica, 1970. **18**: p. 599-610.
39. Roesler, J., H. Harders, and M. Baeker, *Mechanical Behaviour of Engineering Materials: Metals, Ceramics, Polymers, and Composites*. 2007: Springer.
40. Bridgman, P.W., *Studies in large plastic flow and fracture: with special emphasis on the effects of hydrostatic pressure*. 1964: Harvard University Press.
41. Hosford, W.F., *Mechanical Behavior of Materials*. 2005: Cambridge University Press.
42. Mukhopadhyay, N.K. and P. Paufler, *Micro- and nanoindentation techniques for mechanical characterisation of materials*. International Materials Reviews, 2006. **51**(4): p. 209-245.

43. Tabor, D., *A Simple Theory of Static and Dynamic Hardness*. Proceedings of the Royal Society of London. Series A, Mathematical and Physical Sciences, 1948. **192**(1029): p. 247-274.
44. Hutchings, I.M., *The contributions of David Tabor to the science of indentation hardness*. Journal of Materials Research, 2009. **24**(03): p. 581-589.
45. Fischer-Cripps, A.C., *Introduction to Contact Mechanics*. 2007: Springer.
46. Johnson, K.L., *The correlation of indentation experiments*. Journal of the Mechanics and Physics of Solids, 1970. **18**(2): p. 115-126.
47. Shaw, M.C. and G.J. DeSalvo. *On the plastic flow beneath a blunt axisymmetric indenter*. 1969: ASME.
48. Doerner, M.F. and W.D. Nix, *A method for interpreting the data from depth-sensing indentation instruments*. Journal of Materials Research, 1986. **1**(04): p. 601-609.
49. Oliver, W.C. and G.M. Pharr, *An Improved Technique for Determining Hardness and Elastic-Modulus Using Load and Displacement Sensing Indentation Experiments*. Journal of Materials Research, 1992. **7**(6): p. 1564-1583.
50. Oliver, W.C. and G.M. Pharr, *Measurement of hardness and elastic modulus by instrumented indentation: Advances in understanding and refinements to methodology*. Journal of Materials Research, 2004. **19**(1): p. 3-20.
51. Fischer-Cripps, A.C., *Nanoindentation*. 2011: Springer.
52. Tsui, T.Y. and G.M. Pharr, *Substrate effects on nanoindentation mechanical property measurement of soft films on hard substrates*. Journal of Materials research, 1999. **14**(1): p. 292-301.
53. Tsui, T.Y., C.A. Ross, and G.M. Pharr, *A method for making substrate-independent hardness measurements of soft metallic films on hard substrates by nanoindentation*. Journal of Materials research, 2003. **18**(6): p. 1383-1391.
54. Guo, Y.Z., et al., *Critical issues related to instrumented indentation on non-uniform materials: Application to niobium subjected to high pressure torsion*. Materials Science and Engineering a-Structural Materials Properties Microstructure and Processing, 2013. **586**: p. 149-159.
55. Bolshakov, A. and G.M. Pharr, *Influences of pileup on the measurement of mechanical properties by load and depth sensing indentation techniques*. Journal of Materials Research, 1998. **13**(04): p. 1049-1058.

56. Joslin, D.L. and W.C. Oliver, *A new method for analyzing data from continuous depth-sensing microindentation tests*. Journal of Materials Research, 1990. **5**(01): p. 123-126.
57. Ma, Q. and D.R. Clarke, *Size-dependent hardness of silver single-crystals*. Journal of Materials research, 1995. **10**: p. 853-863.
58. Nix, W.D. and H.J. Gao, *Indentation size effects in crystalline materials: A law for strain gradient plasticity*. Journal of the Mechanics and Physics of Solids, 1998. **46**(3): p. 411-425.
59. Zhang, T.Y. and W.H. Xu, *Surface effects on nanoindentation*. Journal of Materials research, 2002. **17**(7): p. 1715-1720.
60. Reuter, W.G., et al., *Fatigue and Fracture Mechanics: 33rd Volume*. 2003: American Society for Testing & Materials.
61. Hainsworth, S.V., H.W. Chandler, and T.F. Page, *Analysis of nanoindentation load-displacement loading curves*. Journal of Materials Research, 1996. **11**(08): p. 1987-1995.
62. Troyon, M. and M. Martin, *A critical examination of the $P-h^2$ relationship in nanoindentation*. Applied Physics Letters, 2003. **83**(5): p. 863-865.
63. Dao, M., et al., *Computational modeling of the forward and reverse problems in instrumented sharp indentation*. Acta Materialia, 2001. **49**(19): p. 3899-3918.
64. Branch, N.A., et al., *Material-dependent representative plastic strain for the prediction of indentation hardness*. Acta Materialia, 2010. **58**(19): p. 6487-6494.
65. Mata, M., M. Anglada, and J. Alcalá, *A hardness equation for sharp indentation of elastic-power-law strain-hardening materials*. Philosophical Magazine A, 2002. **82**(10): p. 1831-1839.
66. Lee, J., C. Lee, and B. Kim, *Reverse analysis of nano-indentation using different representative strains and residual indentation profiles*. Materials & Design, 2009. **30**(9): p. 3395-3404.
67. Shim, S., J.-i. Jang, and G.M. Pharr, *Extraction of flow properties of single-crystal silicon carbide by nanoindentation and finite-element simulation*. Acta Materialia, 2008. **56**(15): p. 3824-3832.
68. Antunes, J.M., et al., *A new approach for reverse analyses in depth-sensing indentation using numerical simulation*. Acta Materialia, 2007. **55**(1): p. 69-81.

69. Kim, J.-Y., et al., *Determination of tensile properties by instrumented indentation technique: Representative stress and strain approach*. Surface and Coatings Technology, 2006. **201**(7): p. 4278-4283.
70. Pelletier, H., *Predictive model to estimate the stress-strain curves of bulk metals using nanoindentation*. Tribology International, 2006. **39**(7): p. 593-606.
71. Farrissey, L.M. and P.E. McHugh, *Determination of elastic and plastic material properties using indentation: Development of method and application to a thin surface coating*. Materials Science and Engineering a-Structural Materials Properties Microstructure and Processing, 2005. **399**(1-2): p. 254-266.
72. Bucaille, J.L., et al., *Determination of plastic properties of metals by instrumented indentation using different sharp indenters*. Acta Materialia, 2003. **51**(6): p. 1663-1678.
73. Giannakopoulos, A.E. and S. Suresh, *Determination of elastoplastic properties by instrumented sharp indentation*. Scripta Materialia, 1999. **40**(10): p. 1191-1198.
74. Jayaraman, S., et al., *Determination of monotonic stress-strain curve of hard materials from ultra-low-load indentation tests*. International Journal of Solids and Structures, 1998. **35**(5-6): p. 365-381.
75. Jha, K.K., N. Suksawang, and A. Agarwal, *Analytical method for the determination of indenter constants used in the analysis of nanoindentation loading curves*. Scripta Materialia, 2010. **63**(3): p. 281-284.
76. Tabor, D., *The hardness of solids*. Review of Physics in Technology, 1970. **1**(3): p. 145.
77. Giannakopoulos, A.E., P.L. Larsson, and R. Vestergaard, *Analysis of Vickers Indentation*. International Journal of Solids and Structures, 1994. **31**(19): p. 2679-2708.
78. Ogasawara, N., N. Chiba, and X. Chen, *Representative strain of indentation analysis (vol 20, pg 2225, 2005)*. Journal of Materials Research, 2006. **21**(10): p. 2699-2700.
79. Chollacoop, N., M. Dao, and S. Suresh, *Depth-sensing instrumented indentation with dual sharp indenters*. Acta Materialia, 2003. **51**(13): p. 3713-3729.
80. Chaudhri, M.M., *Subsurface strain distribution around Vickers hardness indentations in annealed polycrystalline copper*. Acta Materialia, 1998. **46**(9): p. 3047-3056.

81. Tabor, D., *Indentation hardness: Fifty years on - A personal view*. Philosophical Magazine a-Physics of Condensed Matter Structure Defects and Mechanical Properties, 1996. **74**(5): p. 1207-1212.
82. Eswar Prasad, K., N. Chollacoop, and U. Ramamurty, *Role of indenter angle on the plastic deformation underneath a sharp indenter and on representative strains: An experimental and numerical study*. Acta Materialia, 2011. **59**(11): p. 4343-4355.
83. Sakharova, N.A., et al., *Comparison between Berkovich, Vickers and conical indentation tests: A three-dimensional numerical simulation study*. International Journal of Solids and Structures, 2009. **46**(5): p. 1095-1104.
84. Branch, N.A., et al., *A new reverse analysis to determine the constitutive response of plastically graded case hardened bearing steels*. International Journal of Solids and Structures, 2011. **48**(3-4): p. 584-591.
85. Society of Automotive, E., T. American Society for, and Materials, *Metals & alloys in the unified numbering system*. 8th ed. Handbook Supplements Series. 1999: Society of Automotive Engineers.
86. Hay, J., P. Agee, and E. Herbert, *CONTINUOUS STIFFNESS MEASUREMENT DURING INSTRUMENTED INDENTATION TESTING*. Experimental Techniques, 2010. **34**(3): p. 86-94.
87. ASTM, *E9 - 09. Standard Test Methods of Compression testing of Metallic Materials at Room Temperature*. 2009, ASTM International: PA, USA. p. 22.
88. Kalidindi, S.R., A. Abusafieh, and E. El-Danaf, *Accurate characterization of machine compliance for simple compression testing*. Experimental Mechanics, 1997. **37**(2): p. 210-215.
89. Maier, V., et al., *Nanoindentation strain-rate jump tests for determining the local strain-rate sensitivity in nanocrystalline Ni and ultrafine-grained Al*. Journal of Materials Research, 2011. **26**(11): p. 1421-1430.
90. ASTM, *E407 - 07. Standard Practice for Microetching Metals and Alloys*. 2007, ASTM International: PA, USA. p. 22.
91. Vander Voort, G.F., *Metallography, principles and practice*. 1999: ASM International.
92. Bramfitt, B.L., *Metallographer's Guide: Practice and Procedures for Irons and Steels*. 2001: ASM International.

93. ASTM, *E384-11. Standard Test Method for Knoop and Vickers Hardness of Materials*. 2011, ASTM International: PA, USA. p. 43.
94. Srikant, G., N. Chollacoop, and U. Ramamurty, *Plastic strain distribution underneath a Vickers Indenter: Role of yield strength and work hardening exponent*. *Acta Materialia*, 2006. **54**(19): p. 5171-5178.
95. Cao, Y.P. and J. Lu, *A new method to extract the plastic properties of metal materials from an instrumented spherical indentation loading curve*. *Acta Materialia*, 2004. **52**(13): p. 4023-4032.
96. Puttick, K.E., *Ductile fracture in metals*. *Philosophical Magazine*, 1959. **4**(44): p. 964-969.
97. Beachem, C.D. and G.R. Yoder, *Elastic-plastic fracture by homogeneous microvoid coalescence tearing along alternating shear planes*. *Metallurgical Transactions*, 1973. **4**(4): p. 1145-1153.
98. Thomason, P.F., *A three-dimensional model for ductile fracture by the growth and coalescence of microvoids*. *Acta Metallurgica*, 1985. **33**(6): p. 1087-1095.
99. Benzerga, A.A. and J.B. Leblond, *Ductile Fracture by Void Growth to Coalescence*, in *Advances in Applied Mechanics, Vol 44*, H. Aref and E. VanDerGiessen, Editors. 2010, Elsevier Academic Press Inc: San Diego. p. 169-305.
100. Stroh, A.N., *A theory of the fracture of metals*. *Advances in Physics*, 1957. **6**(24): p. 418-465.
101. Segal, V.M., *Materials processing by simple shear*. *Materials Science and Engineering: A*, 1995. **197**(2): p. 157-164.
102. Valiev, R.Z. and T.G. Langdon, *Principles of equal-channel angular pressing as a processing tool for grain refinement*. *Progress in Materials Science*, 2006. **51**(7): p. 881-981.
103. Lowe, T. and R.Z. Valiev, *Investigations and Applications of Severe Plastic Deformation*. 2000: Springer Netherlands.
104. Verlinden, B., *Severe Plastic Deformation of Metals*, in *2nd International Conference Deformation, Processing and Structure of Materials, Part I*. 2005: Belgrade, Serbia and Montenegro. p. 165-182.
105. Nakashima, K., et al., *Development of a multi-pass facility for equal-channel angular pressing to high total strains*. *Materials Science and Engineering: A*, 2000. **281**(1-2): p. 82-87.

106. Iwahashi, Y., et al., *Principle of equal-channel angular pressing for the processing of ultra-fine grained materials*. Scripta Materialia, 1996. **35**(2): p. 143-146.
107. Barber, R.E., et al., *Product yield for ECAE processing*. Scripta Materialia, 2004. **51**(5): p. 373-377.
108. Lucas, B. and W. Oliver, *Indentation power-law creep of high-purity indium*. Metallurgical and Materials Transactions A, 1999. **30**(3): p. 601-610.
109. Mueller, J., et al., *Local investigations of the mechanical properties of ultrafine grained metals by nanoindentations*, in *Nanomaterials by Severe Plastic Deformation*, Z. Horita, Editor. 2006. p. 31-36.
110. Valiev, R.Z., et al., *Paradox of strength and ductility in metals processed by severe plastic deformation*. Journal of Materials Research, 2002. **17**(1): p. 5-8.
111. Dalla Torre, F., et al., *Microstructures and properties of copper processed by equal channel angular extrusion for 1–16 passes*. Acta Materialia, 2004. **52**(16): p. 4819-4832.
112. Ferrasse, S., et al., *Microstructure and properties of copper and aluminum alloy 3003 heavily worked by equal channel angular extrusion*. Metallurgical and Materials Transactions a-Physical Metallurgy and Materials Science, 1997. **28**(4): p. 1047-1057.
113. Alkorta, J., J.M. Martínez-Esnaola, and J. Gil Sevillano, *Critical examination of strain-rate sensitivity measurement by nanoindentation methods: Application to severely deformed niobium*. Acta Materialia, 2008. **56**(4): p. 884-893.
114. Wei, Q., *Strain rate effects in the ultrafine grain and nanocrystalline regimes— influence on some constitutive responses*. Journal of Materials Science, 2007. **42**(5): p. 1709-1727.
115. Chen, J., L. Lu, and K. Lu, *Hardness and strain rate sensitivity of nanocrystalline Cu*. Scripta Materialia, 2006. **54**(11): p. 1913-1918.
116. Dalla Torre, F.H., et al., *Recent progress on the study of the microstructure and mechanical properties of ECAE copper*. Journal of Materials Science, 2007. **42**(5): p. 1622-1637.
117. Dalla Torre, F., E.V. Pereloma, and C.H.J. Davies, *Strain rate sensitivity and apparent activation volume measurements on equal channel angular extruded Cu processed by one to twelve passes*. Scripta Materialia, 2004. **51**(5): p. 367-371.

118. Dalla Torre, F.H., et al., *Grain size, misorientation, and texture evolution of copper processed by equal channel angular extrusion and the validity of the hall-petch relationship*. Metallurgical and Materials Transactions a-Physical Metallurgy and Materials Science, 2007. **38A**(5): p. 1080-1095.
119. Salimyanfard, F., et al., *EBSD analysis of nano-structured copper processed by ECAP*. Materials Science and Engineering: A, 2011. **528**(16–17): p. 5348-5355.
120. Su, J., et al., *A Rate Dependent Constitutive Model for ECAE Cu Based on Instrumented Nanoindentation Results*. Materials Science and Engineering: A, 2014(0).

VITA

Iván Darío Romero Fonseca was born on July 28, 1977 in Bogotá, the capital of Colombia, South America. The third of four children, Iván showed affinity for the academia since he was in elementary school. He graduated from high school in 1994 from "El Minuto de Dios" School with the third best score. He decided to major in Mechanical Engineering, partly inspired by reading his father's books on the shelf. He was admitted in fall 1995 to The National University of Colombia at Bogotá with the fourth best score in the admission exam among more than 3000 applicants for that major. For his machine design course, he and his fellow students designed and built a Stacker hydraulic Lift Truck. He worked for one year and a half on his undergraduate thesis titled "Artificial Vision System" applied to Materials Requirements Planning (MRP) and to Coordinate-Measuring machine motion. He received his B. S. in Mechanical Engineering degree in spring 2002. After graduation, He worked for the industry; in the area of production in a textile company, and in the CAD area in another company. While working, he was offered a position as lecturer professor at the Colombian School of Industrial Careers (ECCI), where he developed his inclination towards Mechanics and Materials Science, and teaching. The idea of coming to the U.S.A to study came about when he attended the ASME congress at New York City in November 2001. That goal motivated him to teach himself English in addition to his mother's example. He went back to New York City in 2002, and traveled to Charlotte, NC in 2006. During his stay in Charlotte, he visited the campus of The University of North Carolina, where he applied to one year later; first to the English Language Training Institute and then to the Graduate School . He started his Master's/PhD in spring 2008. He joined Dr. Wei's research group

in late fall 2008. A series of events like health issues, the birth of his daughter, the loss of his beloved grandma and others put at risk the completion of his PhD. After one semester on a leave of absence, he earned his M.Sc. degree in spring 2011. Thereafter, he started working in different projects and in his dissertation research. He was awarded the Outstanding Graduate Teaching Assistant recognition in spring 2013 for his commitment and dedication in teaching the Materials and Mechanics lab to senior undergraduates. He has been offered to be the lecturer instructor for instrumentation and materials laboratories in summer 2014. He is member of the American Society for Mechanical Engineers (ASME) and of the Society of Hispanic Professional Engineers (SHPE).